

Diss. ETH No. 22445

# Scanning Probe Thermometry of Nanosystems

A thesis submitted to attain the degree of  
DOCTOR OF SCIENCES of ETH ZURICH  
(Dr. sc. ETH Zurich)

presented by  
FABIAN ROMAN MENGES  
Master of Science in Materials Science, ETH Zurich  
born 21.04.1985  
citizen of Germany

accepted on the recommendation of  
Prof. Dr. Andreas Stemmer, examiner  
Dr. Bernd Gotsmann, co-examiner

2015



# Abstract

This thesis reports on the development of a thermal scanning probe microscope and methods for nanoscale thermometry. The instrument and the techniques are applied to quantify thermal transport across graphene layers, the temperature of nanoscopic hot spots in self-heated metal interconnects as well as local Joule and Peltier effects in indium arsenide (InAs) nanowires contacted by metal electrodes. The work is motivated by the lack of experimental tools and techniques to characterize thermal processes, such as the self-heating of transistors, in nanosystems.

The design, the operation and the characterization of the pico-Watt-per-Kelvin thermal scanning probe microscope are illustrated and discussed. The performance of the microscope is first demonstrated in studies of thermal transport across graphene sheets of varying thickness. Thermal resistance modulations are quantified with sub-10 nm spatial resolution and sensitivity for the individual atomic layers.

The quantification of nanoscopic temperature fields is enabled by the development of a technique termed scanning probe thermometry. Scanning probe thermometry is a two-path method inferring temperature by probing the total steady-state heat flux and a temporally modulated heat-flux signal between the scanning probe sensor and a sample simultaneously. The novel technique minimizes contact-geometry-related artifacts that so far limited the reliability of nanoscopic temperature measurements by scanning thermal microscopy.

The method is applied to quantify self-heating of metal interconnects. Nanoscopic hot spots near 40 nm-wide lithographically defined defects are characterized with 30 mK sample temperature resolution. The method is further extended by a dual-harmonic detection scheme to separate different thermophysical effects so far only observed as superposition in thermal scanning probe measurements. Advantageously, the technique is applied to directly image Joule heating and Peltier effects at the contacts of an InAs nanowire with 10 nm spatial and 85 mK sample temperature resolution.

*Abstract*

# Zusammenfassung

Diese Doktorarbeit beschreibt die Entwicklung eines thermischen Rastersondenmikroskops und Methoden zur nanoskaligen Thermometrie. Das Gerät und die Techniken werden verwendet, um den Wärmetransport über Grapheneschichten, die Temperatur von Hotspots in selbst-heizenden Metalleitern, sowie Joule- und Peltier-Effekte in Indium Arsenid Nanodrähten zu bestimmen. Die Arbeit ist durch den Mangel experimenteller Methoden und Geräte zur Charakterisierung thermischer Prozesse in Nanosystemen, wie die Selbsterwärmung von Transistoren, motiviert. Das Design, der Betrieb und die Charakterisierung des picoWatt-pro-Kelvin thermischen Rastersondenmikroskops werden illustriert und erläutert. Die Leistungsfähigkeit des Mikroskops wird zunächst anhand von Wärmetransportmessungen über Grapheneschichten unterschiedlicher Dicke demonstriert. Thermische Widerstandsänderungen werden mit einer räumlichen Auflösung kleiner als 10 nm und mit Sensitivität für einzelne Atomlagen quantifiziert. Die Bestimmung nanoskopiger Temperaturfelder ist durch die Entwicklung einer Technik ermöglicht, die hier als Rastersonden-Thermometrie bezeichnet wird. Die Technik beruht auf einer zwei-Kanal-Methode, bei der gleichzeitig ein stationärer und ein zeitlich modulierter Wärmestrom gemessen werden, um die Proben temperatur zu bestimmen. Die neuartige Technik minimiert kontaktgeometrie-bedingte Artefakte, welche bisher die Verlässlichkeit nanoskopiger Temperaturfeldmessungen mittels thermische Rastersondenmikroskopie limitiert haben.

Die Methode wird verwendet, um die Selbsterwärmung von Metalleitern zu untersuchen. Hotspots in der Nahe 40 nm kleiner, lithographisch definierter Defekte, werden mit einer Temperaturauflösung von 30 mK charakterisiert. Darüberhinaus wird die Methode um ein dual-harmonisches Messschema erweitert, welches die Trennung thermophysikalischer Effekte ermöglicht die andernfalls nur in Überlagerung untersucht werden können. Dadurch ermöglicht die Methode die direkte Abbildung von jouscher Erwärmung und Peltier-Effekten an den Kontakten eines InAs Nanodrahtes mit einer räumlichen Auflösung von 10 nm und einer Temperaturauflösung von 85 mK.



# Contents

Abstract	iii
Zusammenfassung	v
1 Hot Topics and Cool Ideas	1
1.1 Thermal Measurements by Local Scanning Probes . . . . .	1
1.2 Fundamentals of Scanning Probe Thermometry . . . . .	7
1.3 The Concept of Temperature on the Nanoscale . . . . .	14
1.4 Scope and Motivation . . . . .	18
1.5 Organization . . . . .	20
2 A Scanning Thermal Microscope for Nanoscale Thermometry	23
2.1 A Thermometer for the Nanoscale . . . . .	24
2.2 Design and Development of the Microscope . . . . .	24
2.3 Instrument Control and Data Acquisition . . . . .	38
2.4 Calibration of the Heatable Scanning Probes . . . . .	43
2.5 Noise Characterization and Thermal Resolution . . . . .	47
2.6 Conclusions . . . . .	55
3 Mapping Thermal Resistance Modulations across Graphenes	57
3.1 An Atomic Sheet for Heat Spreading . . . . .	58
3.2 Thermal Transport into Graphene on Silicon Dioxide . . . . .	60
3.3 An Analytical Model of Heat Spreading into Graphene . . . . .	64
3.4 Thermal Identification of Graphene Flakes on Silicon Carbide	70
3.5 Lateral Thermal Resolution and Topography Artifacts . . . . .	72
3.6 Conclusions . . . . .	74
4 Quantification of Nanoscopic Temperature Fields and Hot Spots	75
4.1 Why Moore got a Fever . . . . .	76
4.2 Nanoscale Thermometry by the Heat Flux Reference Method	77
4.3 Local Self-Heating of Nanoscale Metal Interconnects . . . . .	82
4.4 Observation of Nanoscale Hot Spots . . . . .	90
4.5 Temperature Resolution and Topography Artifacts . . . . .	95
4.6 Conclusions . . . . .	98

---

5	Imaging Local Joule and Peltier Effects in InAs Nanowires	99
5.1	Asking Kelvin if Peltier is Cooler than Joule . . . . .	100
5.2	Dual Harmonic Detection for Scanning Probe Thermometry .	101
5.3	Observation of Joule and Peltier Effects in an InAs Nanowire	104
5.4	Bias-Dependent Investigation of Joule and Peltier Effects . .	113
5.5	Bipolar versus Unipolar Detection . . . . .	116
5.6	Conclusions . . . . .	120
6	Final Remarks	121
6.1	Conclusion . . . . .	121
6.2	Outlook . . . . .	123
	References	125
	Acknowledgments	137
	Appendix: Calibration Assumptions and Uncertainty Estimations	139
	Publication List	143
	Curriculum Vitae	145



# 1

## Hot Topics and Cool Ideas

As physical sciences, life sciences and technologies explore nanoscopic transport and conversion processes, they face a common question. How is thermal energy transferred and converted? If we can answer this question, we understand a major principle of nature. It is the transfer of thermal energy, heat, that affects the physical properties of matter, that governs the kinetics of chemical reactions, and that triggers biomolecular mechanisms in living organisms. It is the conversion of thermal energy that rules our technologized lives, the speed of our computers, and even our own physical existence.

Understanding this unifying principle of nature puts the measurement of temperature into an exceptional perspective. Scanning probe thermometry provides a fundamental link between diverse nanosystems, all dealing with the control and conversion of thermal energy carriers, such as electrons, phonons and photons. The progressive specialization of science and technology tends to obscure this underlying thermal context.

### 1.1 Thermal Measurements by Local Scanning Probes

Various methods, such as infrared thermography, optical interferometry, fluorescence thermography and thermorefectance microscopy, exist to explore thermal effects and properties [1, 2]. These techniques have an optical-diffraction-limited resolution and can hardly be used to quantify thermal

processes on nanoscopic length scales. This lack of spatial resolution is a major hurdle for nanoscience and -technology as the emergence of thermal nonequilibrium processes, such as the formation of nanoscopic hot spots in transistors (few to tens of nanometer in size) cannot be studied by these techniques.

To address this issue, thermal scanning probe techniques have been developed with spatial resolution down to tens to hundreds of nanometers [3–15, 15–19]. The general attempt to quantify thermal properties using thermal scanning probes is referred to as scanning thermal microscopy (SThM) [20]. In SThM, a temperature-sensitive probe is brought into contact with a sample surface to establish a thermal interaction between a sensing element of the scanning probe and a sample (see Fig. 1.1). SThM has been applied to probe thermal properties like thermal conductivities [14, 17, 21–23] and thermal processes such as phase transitions [8, 24] and Joule heating [13, 15, 25–29]. Different kinds of thermal scanning probes have been employed using fluorescence [30], thermocouple [29] or thermoresistive [31–34] sensing elements. Also non-specialized probes can be used to study thermal properties on nanoscopic length scales based on techniques such as scanning Joule expansion microscopy [35–39] or scanning tunneling microscopy [40]. Regardless what kind of thermal scanning probe is used, all approaches face similar challenges as we will illustrate in the following.

Thermal scanning probe systems are based on the measurement of some kind of temperature sensitive physical effect of a scanning probe sensor that needs to be related to some thermal property of a sample in interaction with the probe. Effects typically used include the temperature dependence of the electrical resistance [27], the Seebeck effect [29], optical fluorescence [30] or the bimetal effect [41, 42]. The application of numerous further sensing mechanisms could easily be imagined, as essentially all physical properties show a more or less pronounced temperature dependence.

Using the temperature dependence of the electrical resistance as a sensing principle is particularly convenient as signals can be acquired with reasonable effort. Accordingly, resistive thermal probes are most common, and various types of probes have been developed and are commercially available [20]. Their operation is typically based on two apparently different modes, either an active heating by an applied sensing current or a passive operation by applying only a small DC and/or AC sensing current [20]. Typically, either the temperature of the scanning probe sensor or the applied power is kept constant [20]. For nanoscopic thermal measurements, all these apparently different modes of operation are equivalent, as ultimately a heat-

flux-related signal (indicated as  $\dot{Q}$  in Fig. 1.1) between the scanning probe and the sample is measured.

In the following, we provide an overview about some major challenges thermal scanning probe measurements face.

A first common challenge is the need to relate the measured sensor signal, to the temperature of the scanning probe sensor. This is indicated as  $T(\text{signal})$  in Fig. 1.1). Depending on the physical property used as sensing mechanism, this requires different kinds of calibration steps as typical scanning probes cannot directly act as primary thermometer. In the case of resistive probes, the temperature of the scanning probe relates to the electrical resistance of the sensor element and can be quantified in relation to the electrical power dissipated in the probe [27, 43]. Different approaches for calibration of resistive silicon scanning probes are discussed in chapter 2.4 of this thesis.

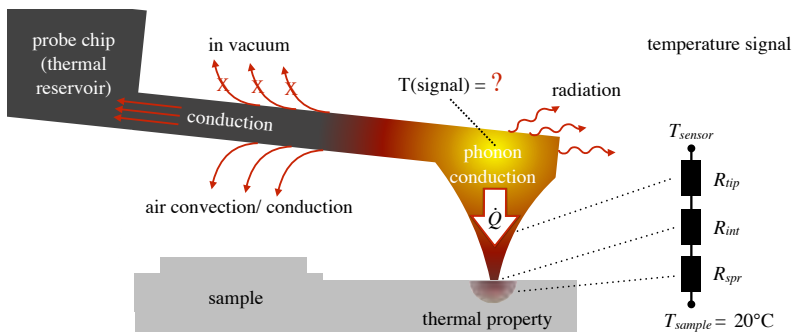


**Figure 1.1: Illustration of a thermal scanning probe measurement**

The temperature dependent sensor signal  $T(\text{signal})$  needs to be related to the heat flux ( $\dot{Q}$ ) between the scanning probe heater/sensor and the sample. Different kinds of heat transfer mechanisms, such as convection/conduction (only in air), radiation and phonon heat conduction across the tip-sample contact can contribute to the thermal interaction between the probe and the sample. Thermal properties of the sample are typically inferred from the phonon transport related heat flux across the contact, which is a function of different thermal resistances, such as the thermal resistance due to the tip ( $R_{tip}$ ), the interface resistance between the tip and the sample ( $R_{int}$ ) and the spreading resistance ( $R_{spr}$  within the sample).

A second challenge of thermal scanning probe measurements is the need to establish and control the thermal interaction between the scanning probe sensor and the sample. Different mechanisms of heat transfer between the probe and the sample are indicated in Fig. 1.1. Both the position of the

scanning probe relative to the sample surface, as well as the scanning probe environment need to be controlled, e.g., by establishing vacuum conditions, controlling the ambient temperature and humidity. Control of the environment is particularly needed to minimize parasitic heat flow between the scanning probe sensor and the sample, for example via gas-mediated conduction [12, 44, 45]. In ambient conditions and non-contact mode operation, the thermal interaction between the probe and the sample is dominated via gas-mediated conduction, which is a function of the tip-sample distance. Hence the thermal scanning probe is measuring a topography related signal that cannot easily be related to some thermal property of the sample beneath the probe. If the scanning probe is in contact with the sample, the thermal interaction is a function of both, the gas-mediated topography-related conduction and phonon heat conduction across the tip-sample contact. Both of these two conduction mechanisms can potentially be dominant, depending on the length of the tip, e.g., the distance between the scanning probe sensor and the sample and the size of the solid-solid contact defined by the sharpness of the tip apex [12, 44, 45]. For thermal scanning probe measurements with nanoscopic resolution, the thermal conductance of the solid-solid contact is typically less than that via gas conduction and thermal properties of the sample cannot be inferred. Accordingly, operation in vacuum conditions is required [14].

A third common challenge is the need to sensitively measure the thermal interaction between the scanning probe sensor and the sample, indicated by the large white arrow across the tip-sample contact in Fig. 1.1. Here, operation in vacuum conditions provides a further advantage as the thermal interaction between the scanning probe sensor and the sample gets localized to the area defined by the size of the scanning probe tip apex [45]. This is beneficial to achieve a higher spatial resolution. Also model descriptions of thermal transport between the scanning probe and the sample can be simplified as the gas-mediated conduction/convection is excluded.

The sensitivity to which extent the thermal interaction between the probe and the sample can be measured depends not only on the type of temperature dependent physical sensing mechanism, but also on the thermal isolation of the scanning probe sensor against its thermal reservoir. This situation is indicated in Fig. 1.1 as heat conduction along the cantilever into the probe chip. The possibilities to eliminate this parasitic heat flow along the cantilever are limited by a trade-off between the thermal isolation of the sensor and the need for a certain mechanical stiffness of the cantilever to enable scanning probe operation.

Sensitive detection of the thermal interaction between the scanning probe and the sample becomes increasingly challenging as the spatial resolution of

the thermal scanning probe measurement is increased. The thermal conductance between the scanning probe and the sample is strongly dependent on the size of the tip-sample contact and dominated by the thermal interface resistance ( $R_{int}$ ) for nanoscopic contacts [45].

The ultimate challenge of all thermal scanning probe measurements is to assign a meaningful thermal property to the signal acquired by the scanning probe in relation to the sample in contact. Relating the sensor signal to the thermal properties of the sample is often complicated and requires not only control and sensitive measurement of the thermal tip-sample interaction but also a fundamental understanding of the thermal transport across the contact [10, 12, 44].

To understand the challenge related to the interpretation of thermal scanning probe signals, we will consider the thermal interaction between the scanning probe and the sample in some more detail.

The thermal interaction can be described as a heat flux ( $\dot{Q}$ ) between the sensor and the sample. Variations in the heat flux between the sensor and the sample can be related to changes of the thermal conductance ( $G$ ) between the scanning probe and the sample and to changes of the temperature difference between the scanning probe sensor and the sample as

$$\dot{Q} = (T_{sensor} - T_{sample}) \times G. \quad (1.1)$$

One major branch of thermal scanning probe measurements aims to relate the thermal conductance ( $G$ ) between the scanning probe and the sample to the local thermal conductivity ( $\kappa$ ) of the sample by measurement of the heat flux ( $\dot{Q}$ ) for a known temperature difference  $\Delta T$ . The measurement and comparison of thermal conductivities are a fundamental pillar of materials science and the reported abnormal thermal conductivities, meaning deviations between the thermal conductivity of materials in form of nanostructures and that of their bulk counterparts are fascinating [46, 47].

These deviations are related to the different kinds of structural size dependencies that appear as the characteristic length of a structure gets comparable to or smaller than the mean free path, the wavelength and/or the phase coherence length of phonons [47]. Phonon heat conduction gets reduced because phonons with a mean free path exceeding the critical dimension of a structure no longer contribute to thermal transport. In certain periodic structures such as superlattices, also the wave character of phonons may become important [2, 47, 48].

For the same reasons, thermal conductivities of nanoscale structures deviate from those of their bulk counter parts, heat-flux-related signals of thermal

scanning probe measurements cannot easily be related to the thermal conductivity of the sample in contact with the scanning probe. The thermal conductance ( $G$  in  $WK^{-1}$ ) between the scanning probe and the sample is not only due to the thermal conductivity of the sample ( $\kappa$  in  $Wm^{-1}K^{-1}$ ), but comprises significant components related to the scanning probe tip and the interface between the tip apex and the sample. This situation is illustrated in Fig. 1.1 describing the thermal resistance to heat flow between the scanning probe sensor and the sample as a series of thermal resistances due to the tip ( $R_{tip}$ ), the interface between the tip and the sample ( $R_{int}$ ), and the spreading resistance within the sample ( $R_{spr}$ ).

We may actually consider the tip-sample contact as kind of thermal filter between the properties of interest, e.g., the thermal conductivity of the sample, and the sensor element of our scanning probe. We call it a filter because certain phonons contributing to the thermal conductivity in the sample are not permitted to contribute to the heat conduction across the tip-sample interface. The interface acts as a thermal barrier, with a thermal interface resistance related to the phonon mismatch between the silicon scanning probe tip, covered with a native oxide on one side and the sample material on the other side. Not only the interface but also the scanning probe tip itself significantly contributes to the thermal resistance between the scanning probe sensor and the sample. Considering that the thermal conductivity can be described as accumulative function of the mean free path of all phonons contributing to heat conduction at a given temperature [49, 50], we can easily understand that the thermal conductance between the scanning probe sensor and the sample is suppressed by the structural size of the tip, which could be approximated as a conical nanowire [45].

Generally, we would need to characterize both the thermal resistance of the scanning probe tip and the tip-sample thermal interface resistance in order to characterize the thermal conductivity of a sample in contact. While we might be able to approximate the thermal conductivity of the tip [45], estimation of the position dependent thermal interface resistance  $R_{int}(x, y)$  is hardly possible.  $R_{int}(x, y)$  is not just a function of the adjacent materials [51, 52], but even more complex as it relates to a weak mechanical contact with a position dependent contact area that is sensitive to nanoscopic and even atomic features on the sample surface [53]. As a major consequence, it is difficult to relate the signal acquired by thermal scanning probes to the thermal conductivity ( $\kappa$ ) of the sample in contact. This will be further illustrated in chapter 3, which reports thermal transport measurements across graphene layers.

In light of this discussion, reported thermal conductivity measurements obtained with thermal scanning probes might be considered from a different

perspective. Only in rare cases, such as of a large tip-sample contact, may the relative contribution of the thermal interface resistance in defining the tip-sample heat flux become negligible. In this case, the thermal conductivity of a material in contact might be inferred by relative comparison of a sensor signal acquired in contact with an unknown material to a signal acquired in contact with a known reference material [14, 54]. In contrast, high resolution thermal scanning probe measurements have typically an interface-dominated character that prohibits the direct quantification of the sample thermal conductivity.

In the next section, we will introduce a second branch of thermal scanning probe measurements that is also challenging and deals with the quantification of sample temperatures on nanoscopic length scales.

## 1.2 Fundamentals of Scanning Probe Thermometry

The science and practice of temperature measurements is called thermometry. At the beginning of this section, we will highlight some elementary differences between contact thermometry on the macroscale and scanning probe thermometry to illustrate the challenges related to the quantification of nanoscopic temperature fields. In the second part, we will establish some fundamentals of scanning probe thermometry, relevant for the experiments and techniques presented in chapter 4 and chapter 5 of this thesis.

One of the most widely used principles to measure temperature on the macroscale is to bring a thermometer into thermal contact with an object of interest. The general idea behind such a contact thermometer is illustrated in Fig.1.2(a). The thermometer, here a fever thermometer, can thermally equilibrate to an object, here illustrated by the famous scientist Lord Kelvin, after thermal contact is established. The thermometer is thermally well coupled to the body of Kelvin, compared with the isolation to its thermal reservoir (the ambient air). The thermometer has a smaller heat capacitance than the body of Kelvin and equilibrates to his body temperature. Accordingly, the body temperature ( $T=37^\circ\text{C}$ ) can directly be inferred from measuring one temperature-sensitive physical property of the thermometer, e.g., the electrical resistance of the calibrated platinum sensor in the fever thermometer.

In contrast, let us next consider the case of a macroscopic thermometer contacting a nanoscopic object. A thermal scanning probe cantilever can be considered as a macroscopic thermometer with a microscopic thermal sensor element to quantify temperature fields by forming nanoscopic contacts.

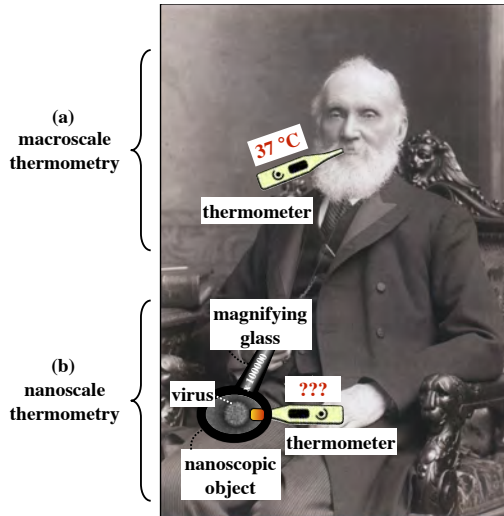


**Figure 1.2: Comparison between macroscale and nanoscopic thermometry**

(a) Typical example of macroscale thermometry, here indicated by the measurement of the body temperature of William Thomson, 1st Baron Kelvin, using a fever thermometer (source: Wikipedia (with no copyright restrictions on this historical image))

(b) Illustration of the challenge of nanoscale thermometry in comparison with the macroscopic case. A large thermometer, well coupled to its thermal reservoir (the hand of Kelvin) needs to quantify the temperature of a nanoscopic object, here symbolized by the virus seen through a magnifying glass.



We illustrate this situation in Fig. 1.2(b) by indicating a virus (symbolizing our nanoscopic object), being contacted by a large thermometer using a magnifying glass. The thermometer is huge compared with the size of the virus ( $\sim 50$  nm) and has a larger heat capacitance. Additionally, the thermometer is significantly better coupled to its thermal reservoir (Kelvins hand) than to the virus. Accordingly, the thermometer cannot equilibrate to the temperature of the virus at a temperature different from the thermal reservoir. Likewise, the thermal scanning probe sensor cannot equilibrate in contact with a sample at a temperature different from the temperature of its thermal reservoir (the chip body), because the thermal resistance to the tip-sample contact is typically two to three orders of magnitude higher than those between the sensor and its thermal reservoir. Instead, the scanning probe sensor experiences a heat flux.

From the illustration in Fig. 1.2(b,) we may also infer that care is needed not to perturb the virus. Just imagine if our magnifying glass would lead to the focusing of some light rays causing an undesirable strong thermal interaction with the virus. In terms of our experiments this means that a strong thermal coupling between the scanning probe and the sample needs to be avoided in order not to perturb the temperature field beneath the scanning probe tip. In thermal scanning probe measurement of high spatial resolution, this can typically be achieved as the thermal interface resistance of the nanoscopic tip-sample contact ( $10^8$  K/W) is dominant and larger than the thermal resistance to heat flow between the nanoscopic volume beneath the scanning probe tip and its embedding environment[55].

Noting that the thermal scanning probe sensor typically cannot thermally equilibrate is fundamental to the understanding of scanning probe thermometry experiments presented in chapter 4 and chapter 5 and in contrast to the macroscopic case illustrated in Fig. 1.2(a). Essentially, the scanning probe sensor can only acquire a heat-flux-related signal, which indeed contains information about the temperature difference between the sensor and the sample, but not exclusively as the heat flux is also a function of the position-dependent thermal resistance  $R_{ts}(x, y)$  across the tip-sample contact. As the scanning probe and the sample are not in equilibrium, the signal contains two unknowns and two measurements are needed to infer information about the sample temperature.

Surprisingly, this is hardly recognized in literature, and attempts to quantify nanoscopic temperature fields using scanning probes commonly assume the thermal resistance as a position-independent constant, approximated from literature values and simulations[15, 28, 29, 56]. However, assuming  $R_{ts} = \text{constant}$  is only leading to reliable temperature measurements if the heat flux between the scanning probe and the sample is nullified in each pixel

of a scanning probe measurement. Practically, this can hardly be achieved and nanoscopic temperature field measurements reported are typically disturbed by local variations of the thermal resistance between the scanning probe sensor and the sample. This disturbance becomes apparent, when the thermal interaction between the scanning probe tip and the sample changes, e.g., because of topography-related variations in the size of the contact area or material dependent thermal conductivity variations [57]. The problem gets reinforced as the thermal scanning probe measurements approach a high spatial resolution on the order of 50 nm and less, because the relative dependence of the heat-flux-dependent signal on the thermal resistance increases as the thermal resistance increases with the decreasing size of the contact, whereas the temperature difference does not scale directly with the contact size.

Accordingly the primary challenge of nanoscopic temperature measurement using local scanning probes seems to be the need to account for an unknown contact-size-related thermal resistance component in the heat-flux related signal measured by the scanning probe. As the tip-sample contact geometry is not well known in most scanning probe measurements, experiments often appear unreliable.

An interesting attempt to overcome this hurdle was suggested by Chung et al. [58]. They reported the quantification of temperature fields on nanoscopic length scales from an extrapolation of heat-flux-dependent scanning probe signals measured at different temperatures of the sensor to zero heat flux. The suggested null point method appears quite intuitive because it resembles the idea of the macroscopic equilibrium contact thermometry. If the heat flux between the sensor and the sample gets zero and thermal equilibrium is established, the sensor signal is independent of the thermal resistance to the sample. The sample temperature equals the sensor temperature and can directly be inferred from a single measurement as in the case of the fever measurement illustrated in Fig. 1.2(a).

However, a pixel-wise heat flux nullification during the scanning mode operation is difficult to be implemented and ultimately limited by the thermal time constant of the scanning probe sensor. All approaches so far reported, trying to adapt a null point method, infer sample temperatures from the measurement of heat-flux-related signals at different temperatures of the scanning probe and a linear extrapolation to zero heat flux [26, 58, 59]. Accordingly, this approach suffers from the same artifacts as those measurements that infer temperature directly from rescaling of heat-flux-related signals by a position-independent thermal resistance. We can conclude that whenever thermal equilibrium between the scanning probe sensor and the sample cannot be achieved, scanning probe thermometry requires the in-

clusion of a position-dependent thermal resistance ( $R_{ts}(x, y)$ ) between the scanning probe and the sample.

We addressed this issue by introducing a double-scan method, taking the need for two measurements into account. In the following, we will provide some fundamentals about this approach, which is the base of the techniques developed in chapter 4 and 5 of this thesis. In the double-scan-technique, temperature fields are quantified by first acquiring the heat-flux-related signal of the scanning probe in contact with a sample for a known temperature difference, followed by a measurement of the heat-flux-related signal at an unknown temperature difference and relating the change in the signal to the changes of the sample temperature. In the following, we will illustrate this method as reported by Menges et al. [27].

To quantify the heat flux through the tip into the surface,  $\dot{Q}_{ts}$ , the small difference between Joule heat generation in the heater,  $P_{heater}$ , and the heat flux away from the heater along the cantilever,  $\dot{Q}_{cl}$ , need to be quantified upon tip-sample contact. Therefore, the cantilever temperature needs to be calibrated first. For resistive scanning probes, heater calibration relies on measuring the current-voltage response of the cantilever and relating the electrical power dissipated to the temperature of the heater. When the scanning probe is in vacuum and the tip is not in contact with the sample, heat is mainly dissipated through the cantilever legs into the chip body (see Fig. 1.3(a)). The thermal resistance of the cantilever legs,  $R_{cl}$ , can be determined by equating the heat flux,  $\dot{Q}_{cl}$ , to the electrical power  $P_{heater}$  needed to reach a certain temperature  $T_{heater}$ . This necessitates knowledge of the exact temperature in the heater-sensor. As the temperature at the maximum electrical resistance of the cantilever is a function of the doping level of the heater [60], the measured electrical resistance of the probe can be correlated to the temperature of the heater by assuming that all electrical power dissipated leads to an increase of the heater temperature. Further details on the calibration of resistive thermal scanning probes, the underlying assumptions and the limitations can be found in chapter 2.4 and the appendix of this thesis.

In a second step, the change in heat flux by opening the heat flow channel through the tip into the surface (see Fig. 1.3(b)) needs to be quantified. This can most conveniently be done by measuring the power and the heater temperature during an approach of the tip to the surface. Fig. 1.3(d) shows the thermal resistance  $R_{th}$  as a function of piezo-displacement during the tip-sample approach. In this example, we can observe a change of thermal resistance resulting from the contact of  $\sim 730$  K/W. The tip-sample thermal

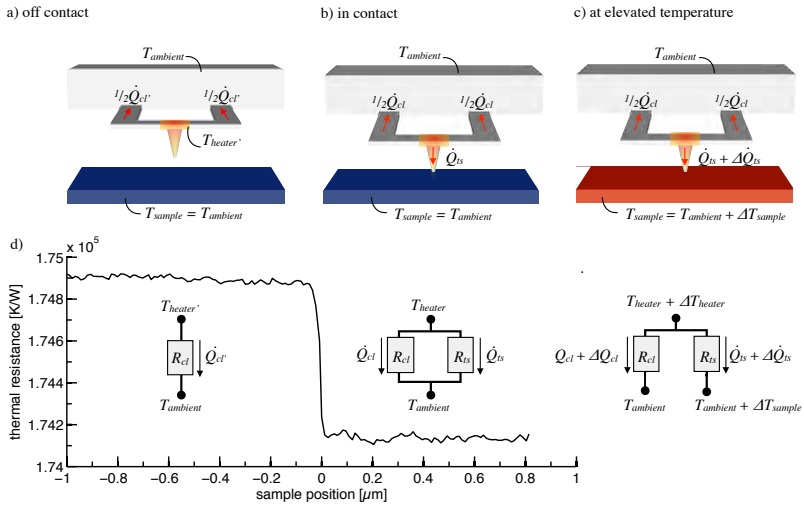


**Figure 1.3: Illustration of principle of the double scan technique [27]**

Schematic of the tip-surface arrangement for the tip being out of contact a), in contact with the sample at ambient temperature b) and in contact with the sample at elevated temperature c).

Panel d) shows the cantilever thermal resistance as function of the piezo-displacement during a tip-sample approach. The sample position was set to zero at the contact point.

resistance  $R_{ts}$  is calculated as

$$R_{ts} = (T_{heater} - T_{ambient}) / \dot{Q}_{ts} , \quad (1.2)$$

with  $T_{ambient} = 20^\circ\text{C}$  and  $\dot{Q}_{ts}$  the tip-sample heat flux.

This calculation of the tip-sample thermal resistance  $R_{ts}$  is made for each pixel of an image while raster-scanning the tip across the sample.

To determine the sample temperature, it is actually not necessary to disentangle the individual contributions to the thermal resistances of the tip-sample contact (see Fig. 1.1). Being able to quantitatively determine the total thermal resistance  $R_{ts}$  allows one to measure the temperatures directly, as explained in the following.

To determine the temperature of the sample in the volume defined by the spreading resistance ( $\approx (d/2)^3$  with  $d$  being the contact diameter of the tip-surface contact [61], all we need to know is the change in heat flux  $\dot{Q}_{ts}$ . For the sample at room temperature, we have a tip-sample thermal resistance defined by Eq. 1.2. If the surface temperature changes by  $\Delta T_{sample}$ , then the heat flux changes to

$$\dot{Q}_{ts} + \Delta\dot{Q}_{ts} = (T_{heater} + \Delta T_{heater} - T_{ambient} - \Delta T_{sample}) / R_{ts} , \quad (1.3)$$

and we arrive at

$$\Delta\dot{Q}_{ts} = (\Delta T_{heater} - \Delta T_{sample}) / R_{ts} . \quad (1.4)$$

Note that this assumes that  $\Delta T_{sample}$  is sufficiently small to require  $R_{ts}$  to be the same for the idle and the heated device. By interesting Eq. 1.2 into Eq. 1.4, the sample temperature can be calculated as

$$\Delta T_{sample} = \Delta T_{heater} - (T_{heater} - T_{ambient}) \times \frac{\Delta\dot{Q}_{ts}}{\dot{Q}_{ts}} \quad (1.5)$$

Although the double-scan-method described is a promising approach for the further development of scanning probe thermometry, the method is limited by the need to acquire two consecutive scans, putting strict requirements on the reproducibility of the tip-sample thermal contact. Furthermore, the need to relate two large heat-flux-related signals dominated by thermal resistance variations to extract a small temperature-related signal variation limits the temperature sensitivity of the approach. These two limitations are addressed in the course of this thesis work and motivate the development of a preferential single-scan scanning probe thermometry method presented in chapter 4 of this thesis.

### 1.3 The Concept of Temperature on the Nanoscale

As this thesis work explores the quantification of temperature in nanosystems, we provide a brief introduction to the concept of temperature on the nanoscale. This is important because the concept of temperature may become questionable as experiments facilitate the characterization of thermodynamic nonequilibrium processes on nanoscopic length scales.

The human perception of temperature is the first step towards a concept of temperature. The heat perception of the skin is in particular interesting as the sensing principle, inferring temperature from a heat flux, shows similarities to the basic idea of scanning probe thermometry. Without the direct experience of hot and cold in our daily life, we may not even find any motivation to investigate the temperature of nanosystems. Considering this intuitive approach, temperature had already been measured before it was first defined, which is an interesting perspective for an experimentalist quantifying temperature fields on nanoscopic length-scales, potentially in the context of local thermodynamic-nonequilibrium.

A detailed theoretical discussion about the concept of local temperature in non-equilibrium nanosystems is beyond the scope of this experimental thesis and we refer to a review by Hartmann [62] that discusses the locality of temperature on nanoscopic length scales, and to a text book by Biró [63], which discusses the fundamentals of temperature for the more theoretically inclined reader. In contrast, this thesis work is motivated by the question whether temperature can be meaningfully measured on nanometer length-scales, a question that is practically motivated and relevant as numerous local thermal effects are important for the understanding of energy transfer and conversion processes in nanosystems. As we follow an experimental approach, we aim to provide a practical definition of temperature as quantified in experiments presented in this thesis. Further we will discuss if there is indeed something like a temperature in the sense we can explore it at macroscopic length-scales. In particular, chapters 4 and 5 will bring this discussion to the real world as experimentally quantified temperature fields with spatial resolution down to 10 nm require a practical definition.

The concept of temperature rests on the laws of thermodynamics and is defined as

$$T = \left( \frac{\partial U}{\partial S} \right)_{V,N} \quad (1.6)$$

by the partial derivative of the internal energy  $U$  of a system with respect to

the entropy  $S$  at constant volume and number of particles. Here, temperature is defined as an intensive property based on thermodynamic equilibrium. This definition of temperature can appear quite abstract and more intuitive is the statistical description of temperature as the average kinetic energy of particles of a substance, something we might even sense in the form of fast colliding gas molecules giving rise to the temperature we can feel on our skin.

In this kinetic description, temperature is inferred by relating the pressure and the volume of a gas to the average molecular kinetic energy ( $E_{avg}$ ) of the gas particles and described as

$$T = \frac{2}{3k_B} \times E_{avg}, \quad (1.7)$$

where  $k_B$  is Boltzmann's constant. Major challenges concerning the concept of temperature arise if we need to give up the definition base of thermal equilibrium and that of a sufficiently large statistical ensemble, e.g., by approaching nanoscopic length scales and local energy conversion and transfer processes.

In order to illustrate this, let us first consider the definition of temperature in the sensor element in our scanning probe cantilever. The scanning probe sensor element is still of microscopic size (approx.  $3 \times 3 \times 0.5 \mu\text{m}$ ) and certainly fulfilling the requirement of a sufficiently large statistical ensemble. However, it is continuously self-heated by an electrical current, causing a thermodynamic nonequilibrium. This global nonequilibrium, does not mean that the temperature of a scanning probe sensor cannot be defined, because local thermodynamic equilibrium within the sensor element can still prevail. Local thermodynamic equilibrium means that for each element or position within the scanning probe sensor the requirements of thermodynamic equilibrium are fulfilled in good approximation, meaning that the properties of each element is similar to that of its neighboring elements. In the statistical picture this would mean that the distribution of all phonons excited within each element of our sensor can be described by the Bose-Einstein statistics. We can still use Eq. 1.7 to define an effective temperature at each location, equivalent to the average energy of phonons at this location.

In our experiments, we typically heat the scanning probe sensor to an average temperature  $T_h$  related to the electrical power dissipated in the sensor. If we now move the scanning probe tip into contact with a sample, we obviously connect the sensor at temperature  $T_h$  to a sample at temperature  $T_s$ . A question typically arising for this experimental configuration concerns the

temperature of the tip-sample contact. This question directly relates to the question whether we can define a local temperature within the sensor, with the small difference that we now try to examine whether we can define a continuous temperature profile between the scanning probe sensor and the sample.

Along the scanning probe tip, we can expect that a temperature can be defined for the same reasons as a temperature for the scanning probe sensor could be defined. In the sample volume beneath the tip, we can also define temperature as long as local thermodynamic equilibrium prevails. For the interface itself, we cannot define a temperature as the interface has no physical size. We rather expect to observe a discontinuity in the temperature profile because of the thermal interface resistance between the scanning probe tip and the sample.

For the sample volume beneath the tip, e.g., a self-heated segment of a nanowire, it can be difficult to infer if locally a thermodynamic equilibrium prevails. The self-heating current certainly leads to a global thermodynamic non-equilibrium. The question whether local thermodynamic equilibrium within the nanowire is achieved appears to depend on the thermal interaction strength between the nanowire and its substrate as well as on the thermal coupling between our scanning probe sensor and the nanowire. A weak thermal coupling between the scanning probe and the nanowire appears needed to ensure that the temperature field is not perturbed. In our measurements, such a situation can typically be achieved because the mechanical contact between the nanoscopic tip apex of the scanning probe and the sample leads to a thermal resistance larger than the thermal resistance to heat flow between the self-heating sample volume beneath the scanning probe tip and its embedding environment. If local thermodynamic equilibrium prevails we can measure meaningful temperature fields with spatial resolution down to 10 nm as presented in this thesis.

On the other hand, we may ask what would happen if local thermodynamic equilibrium does not prevail, but if instead there is something like a local breakdown of the temperature. Situations like this are for example known to appear in a slip-flow regime of gas particles where the temperature close to the wall of a tube remains constant as the gas particles enter a ballistic transport regime [64].

A situation similar to that of the gas particles close to the wall of a vessel might potentially appear in the vicinity of nanoscopic heat source with a size smaller than the average phonon-mean free path of its embedding environment. The phonon transport in the vicinity of such a heat source enters a quasi-ballistic transport regime. Accordingly we might expect to observe a situation similar to that observed in the slip-flow regime of gases. The observation of a constant signal regime in the vicinity of a nanoscopic heat



source might indicate that here a temperature term is assigned to a region, which does not fulfill the requirement of local thermodynamic equilibrium and accordingly cannot to be described following the temperature definition of Eq. 1.6.

Nevertheless, we may always assign a local sample temperature value to the signal measured by the scanning probe sensor. However, this temperature is not necessarily a meaningful value to predict temperature dependent physical properties. On the other hand, we may ask what a local breakdown of the classical temperature definition means for temperature-dependent physical properties. Does the temperature dependence also break down on small length scales, meaning that physical properties as they may experimentally be characterized by a local scanning probe acquire a non-thermal character, or is just the conceptual definition of temperature problematic in these situations? For clarification of this kind of question it may be of interest to investigate nanosystems showing some kind of long range order, like strongly correlated metal-oxides or magnetic systems. Still it appears unclear how one might experimentally distinguish whether or not the locally measured physical property follows a thermal character.

In our current understanding, it makes sense to assign temperature to scanning probe thermometry measurements on nanoscopic length scales, although the theoretical, conceptual definition of temperature may be challenged by these experiments. We anticipate that experimental observations such as those reported in this thesis stimulate the theoretical discussion to assign meaningful concepts of temperature to nanoscopic nonequilibrium processes as they are frequently observed in nanosystems. In our experiments, we always define the sample temperature ( $T_s$ ) as a quantity relating the heat flux ( $Q_{ts}$ ) between the scanning probe sensor at temperature  $T_h$  and the sample to the thermal resistance ( $R_{ts}$ ) to heat flow

$$T_s = T_h - R_{ts}\dot{Q}_{ts}, \quad (1.8)$$

with the thermal resistance  $R_{ts}(T_h, T_s)$  being a function of the temperature difference if  $T_h \gg T_s$ . Since we already included Lord Kelvin in this thesis introduction, we would like to close this sections with one of his quotes: *To measure is to know.*

## 1.4 Scope and Motivation

In the preceding sections we described the experimental challenges arising from the need to locally quantify thermal transport and the temperature on nanoscopic length scales. Furthermore, we discussed some conceptual challenges arising as the experimental investigation of thermal nonequilibrium processes in nanosystems becomes tangible.

Challenges, however, always relate to opportunities and the nanoscopic investigation of temperature fields holds remarkable technological relevance as various processes are based on the interaction of thermal energy carriers such as electrons, phonons and photons on nanoscopic length scales. The quantification of temperature holds information about the energetics of these processes, ultimately aiming to manipulate and control the transfer and conversion of energy.

It is particularly this linking between information and thermal energy transfer and conversion processes that is exciting. The emergence of thermodynamic nonequilibrium processes on nanoscopic length scales, like the formation of local hot spots in the drain region of transistors, is not only challenging today's CMOS technology, but our general approach to information processing. It is fascinating to note that the appearance of these hot spots is less a by-product of a particular type of computing machine, but the logical consequence of irreversible logic, manifested on small length scales.

This universal nature becomes clearer by the fact that not only our computers get hot as we use them, with power densities ( $150 \text{ W/cm}^2$ ) exceeding those of a rocket nozzle [65], but also our own brain cannot memorize a single word of this sentence without dissipating about 25 Joule of heat per second [66]. Whenever information is created or deleted, regardless whether this is related to the switching of a transistor or the configurational change of a protein, tiny amounts of heat are dissipated, essentially one bit of entropy times the temperature of the environment [67, 68]. The liveliness of the world as it is expressed in the permanent creation, deletion and the transmission of information is linked to the dissipation of heat, proceeding at an incredible rate and starting from small length scales. Living in the information age therefore means exploring the warming of the world, whereby thermometry is a key to understand the processes and principles behind it.

Within this global context, we believe that further advance in current understanding of science and technology requires progress in nanoscale thermometry. We intend to address this need by developing and building a highly sensitive sub-nanoWatt per Kelvin thermal scanning probe microscope (chapter 2) and novel methodologies for the quantification of temperatures in nanosystems. This thesis seeks to overcome the experimental lack of tools

and techniques to quantify thermal transport (chapter 3) and temperature down to sub-10 nm length scales. This spatial resolution is technologically required for the characterization of local thermal processes in nanosystems, such as the self-heating of individual transistors in integrated circuits. We further aim to demonstrate the ability to address technologically relevant challenges related to nanoscopic thermodynamic nonequilibrium processes by the direct study of hot spots in metal interconnect test structures (chapter 4) and semiconductor nanowires (chapter 5).

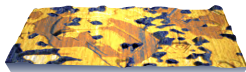
Our merging of hot topics and cool ideas at the end of this introduction may seem paradox, but sometimes nothing burns more than the cold. It is the unexpected experience that makes science exciting and life special. Still, we can just hope to find an ice cube in the desert, that starts to melt as soon as we touch it, either getting hot and dry with time or giving rise to the growth of something unique by spending life and shadow.

## 1.5 Organization

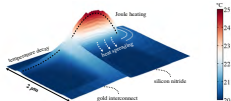
The main part of the thesis work is organized into four chapters. Each chapter is devoted to one set of experimental work, starting with an abstract followed by a brief introduction. Subsequently, all methods and techniques are introduced before the experimental results are presented and discussed in the main body. Each chapter ends with a short summary highlighting the major findings and conclusions.



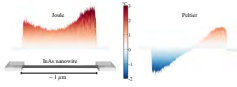
In chapter 2, we report on the development of a vacuum-based scanning thermal microscope. We first provide a short motivation for the development of a high-resolution thermal microscope. Subsequently, we illustrate the design and the development of the instrument, including all major components such as the optical beam deflection detection, the scanning probe head and the sample stage. Finally, we discuss the calibration of the thermal scanning probe sensor and its electrically noise-limited thermal resolution.



In chapter 3, we use the heated tip of the scanning thermal microscope cantilever to study thermal transport across graphene layers. We first provide a short introduction into thermal transport properties of graphene in relation to the potential application as atomically thin heat spreader. Afterwards, we report the investigation of heat dissipation into graphene sheets of different thicknesses, on a silicon oxide and on a silicon carbide substrates. We relate the experimental observations to an analytical model and previously reported thermal conductivities of graphene. Finally we discuss the spatial resolution of our measurements in relation to frequently observed topography artifacts.



In chapter 4, we describe a novel method for the quantification of nanoscopic temperature fields using a scanning probe microscope. We first motivate the development of a nanoscale thermometry method by referring to self-heating of integrated circuits. Next, we derive the fundamental principle of scanning probe thermometry, and subsequently apply the method to quantify self-heating of metal interconnects. Finally, we discuss the spatial and thermal temperature resolution of our measurements in relation to nanoscopic hot spots observed near lithographically defined defects.



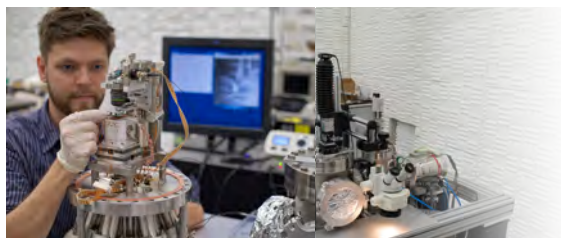
In chapter 5, we introduce a dual harmonic detection method for scanning probe thermometry. We first motivate the development of the method by noting the fundamental challenge of separating different thermophysical effects that can typically only be observed as superposition in thermal scanning probe measurements. Afterwards, we derive the principle of dual harmonic scanning probe thermometry and demonstrate the method by simultaneous imaging of Joule heating and Peltier effects at metal/nanowire contacts. We report systematic studies on the voltage bias dependence of both effects, and validate our temperature measurements by comparison of a bipolar and a unipolar measurement scheme.

In the final chapter of the thesis, we provide a summarizing conclusion of this thesis work, and present a brief outlook on possible directions for future research.



# 2

## A Scanning Thermal Microscope for Nanoscale Thermometry



In this chapter, we report on the development of a vacuum based scanning thermal microscope. The instrument enables quantification of thermal transport properties and local temperature fields in nanosystems with sub-10 nm lateral thermal resolution at sub-nanoWatt per Kelvin conductance sensitivity. This unique microscope is built inside an electromagnetically shielded, temperature stabilized laboratory and rests on a 68-ton concrete block, floating on actively controlled air-springs. The microscope features combined thermal and optical detection. The temperature of the scanning probe can be quantified with sub-mK precision. The temperature difference between the scanning probe sensor and the sample is adjustable over four orders of magnitude. We will discuss the design, the implementation and the performance of this microscope.

## 2.1 A Thermometer for the Nanoscale

Significant efforts towards nanoscale thermometry are devoted to the development of nanoscale thermometers based on luminescent organic dyes, quantum dots and fluorescent nanoparticles [69, 70]. However, nanoscale thermometry does not require the development of nanothermometers, but rather a thermometer for the nanoscale, a scientific instrument that combines local thermal sensing with the measuring capability of a microscope. The development of such a thermal microscope is motivated by the technological need to quantify nanoscopic temperature fields in electronics, photonics, plasmonics, microfluidics and life sciences. The impressive variety of applications underlines the universal nature of temperature measurements and highlights the implication of thermal energy transfer and conversion processes for nanotechnology. Thermometry promises significant progress in the understanding of thermal processes, such as hot spot formation in electronics or intracellular temperature regulation in living organisms [71]. The dependence of many nanoscale devices on temperature is unfortunately not paralleled by the progress in thermal nanometrology, the technique to perform accurate, quantitative temperature measurements in nanosystems. Well-established optical methods for thermal imaging like infrared microscopy, thermoreflectance microscopy or Raman thermometry have diffraction limited spatial resolutions on the range of a few hundred nanometers to microns, which is not sufficient to meet the requirements of many technological needs encountered in nanotechnology. In contrast, scanning probe-based thermal microscopes can achieve combined high spatial resolution and temperature sensitivity [55]. In the following section, we will discuss the design and the building of a highly-sensitive thermal microscope for scanning probe thermometry, a thermometer for the nanoscale.

## 2.2 Design and Development of the Microscope

The design and building of a high-vacuum scanning thermal microscope comprises several key components that need to be considered. An often overlooked aspect of potentially tremendous impact is the laboratory environment.

### The laboratory environment

The performance of a scientific instrument is directly linked to its surroundings. All sources of interferences impacting its functionality have to be considered and their effect minimized. Impressive examples, illustrating this



strategy are the Hubble space telescope which is located in low earth orbit to eliminate light absorption by the atmosphere or the Large Hardron Collider at CERN, which is located 100 m underground to minimize interferences with natural radiation. We are not aiming for a comparison between our efforts to construct a thermal microscope and these two outstanding instruments, but only want to highlight the need to consider its overall design settings.

Like for any scanning probe microscope, mechanical vibrations, temperature fluctuations and electromagnetic radiation are interference sources potentially limiting the spatial resolution and sensitivity. Typically, scanning probe systems comprise active/passive vibration-damping systems and may be placed inside environmental-control chambers. Our new microscope is built inside a specially shielded, environmentally controlled laboratory [72] of the Binnig-Rohrer Nanotechnology center, supporting our efforts to push the frontiers of nanoscale thermal metrology. We will briefly discuss the relevance of this laboratory environment on the design and operation of our microscope.

Fig.2.1 illustrates the experimental arrangement with the vacuum scanning thermal microscope situated inside the electromagnetically shielded laboratory. Sensitive equipment like the amplifiers are placed inside the temperature-stabilized user-room, close to the experiment. All equipment potentially interfering with the function of the microscope is placed inside a utility room, including the computer for data acquisition as well as the control units of positioners and pumps. The ability to isolate sensitive equipment of the experiment from potential noise sources is beneficial for our efforts. At the same time we encountered challenges and constraints in building the instrument inside such a well controlled laboratory environment. The separation of the microscope from the data-acquisition and control units, required long connection distances for both the electrical cabling and the vacuum system. For the cabling, we had to find a trade-off between the separation from potential interference sources and the increasing probability of picking up electromagnetic disturbances by the long cables. With respect to the vacuum system, we had to avoid mechanical excitation of the concrete base via the vacuum hose connecting the chamber to the scroll pump situated in the basement of the utility chamber. The vacuum hose can easily transfer mechanical excitations from the scroll pump onto the floating concrete, inducing unwanted vibrations in our scanning probe microscope. We use ultra-flexible hose that is freely suspended between the wall of the room and the concrete base to minimize this effect.

The electromagnetic shielding and in particular the temperature stabilization are beneficial for our studies as thermally induced drifts of electronic and

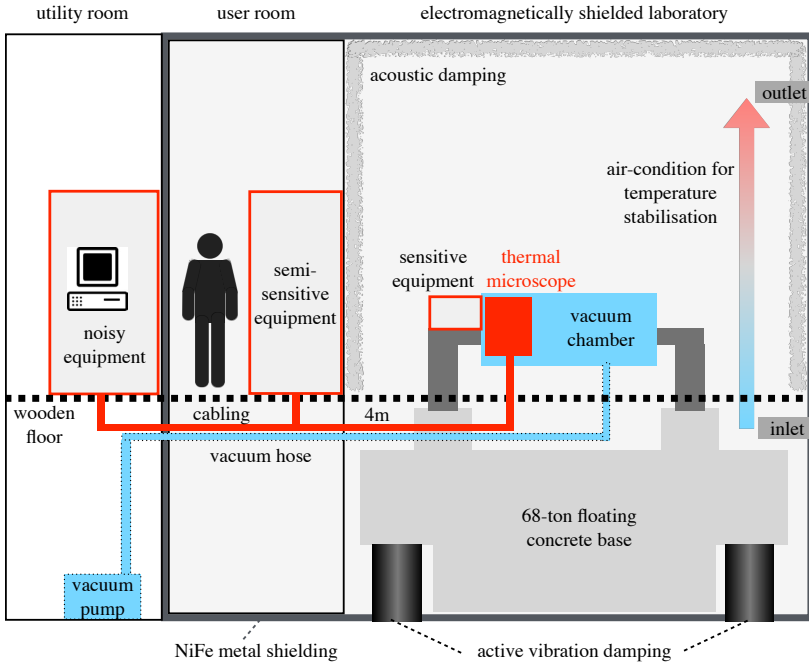


**Figure 2.1: The thermal microscope within the shielded laboratory**

The microscope is placed inside an electromagnetically shielded, temperature stabilized laboratory and resting on an actively vibration damped concrete base. Noise-equipment is separated from the experiment and placed inside the utility chamber.

mechanical systems are reduced. Testing the newly built instrument outside the laboratory would allow one to quantify the direct benefits related to just the laboratory environment. Qualitatively, we observed significant improvements compared with our previous scanning thermal microscope, as demonstrated in the experiments presented in the subsequent chapters.

## The vacuum system

The unique environment of our experiment gets even more special, considering that vacuum conditions are needed to accomplish quantitative scanning probe thermometry [27]. The vacuum chamber, housing the scanning probe microscope, is shown in Fig. 2.2. It is built from standard CF-parts (con-

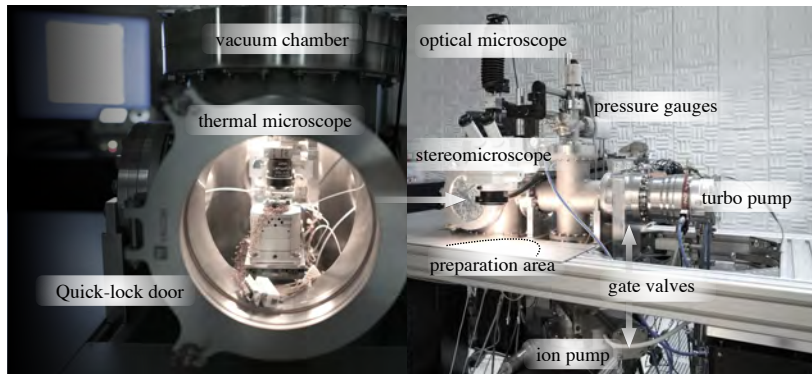


**Figure 2.2: The vacuum chamber system housing the microscope** fixed to a metal frame, directly resting on the floating concrete base of the laboratory. Access to the microscope is ensured by a quick-lock door for convenient exchange of the sample and the scanning probe. By the stereomicroscope mounted next to the quick-lock door, alignment of the multi-pin probe card to the electrical contact pads of a sample device is possible without the need to detach the cabling of the probe card.

flat flanges), except for the bottom flange of the main chamber, which is customized with respect the electrical and optical feedthroughs. The design keeps the number and type of feedthroughs variable to preserve flexibility for future modifications. The vacuum chamber is fixed to a metal frame that directly rests on the vibration-isolated concrete base of the room. Further vibration isolation by the air-springs below the metal frame is not needed. The chamber is ultra-high-vacuum (UHV) compatible, except for minor components, although just high vacuum conditions are needed for the current experiments. One not-UHV-compatible component is the quick-lock

door, which could potentially be replaced by a load lock chamber at a future development stage of the instrument. The quick-lock door ensures fast and easy access to both the sample and the cantilever holder. Two gate valves (Vacom and VAT) are installed to separate the main chamber from vacuum pumps when needed. The turbo pump (Pfeiffer HighPace 300) together with the scroll pump are initially used to pump vacuum levels of below  $10^{-6}$  mbar before the ion pump (Varian Nobel Diode) takes over pumping. The turbo pump is shut down during experiment in order to avoid mechanical excitation of the microscope and electrical interferences noise of the pump control electronics on our measurements. Typically it takes about 5 h of pumping, starting from ambient pressure and including the microscope with some non-fully-vacuum-compatible parts, such as the PCB boards of the optical readout, until scanning probe measurements can be started.

### The scanning probe microscope

Fig. 2.3 shows the scanning thermal microscope. The microscope is built on a rigid L-shaped stainless-steel support structure, resting on four posts forming a strong fixation to the bottom flange of the vacuum chamber. In contrast to most vacuum-based scanning probe systems, there is no additional mechanical damping (e.g. an eddy current system) needed, as the entire microscope is sufficiently isolated against mechanical excitations by the floating base of the room, at least for the spatial resolution currently required.

As visible in Fig. 2.3, our experiments require extensive cabling. In particular, the sample holder and sample stage of the microscope comprise numerous connections. The cable to the sample has 14 wires connected to a multi-pin probe card and a multi-pin connector on the side of the feedthrough. These wires exert, despite the thin diameter, a noticeable mechanical force on the piezo scanner but provide significant extra functionality as multiple nanoelectronic devices can be contacted in parallel by the probe card.

The entire microscope consists of several complex subsystems such as the optical beam deflection detection, the scanning probe head and the sample stage. Mechanical parts of the microscope haven fabricated by M. Tschudy and the IBM model shop according to our design and drawings. In the following, we will introduce the different main components of the microscope individually.

### The optical system

The main component of the optical system is the optical beam deflection (OBD) detection. We decided to build a compact OBD to track the can-

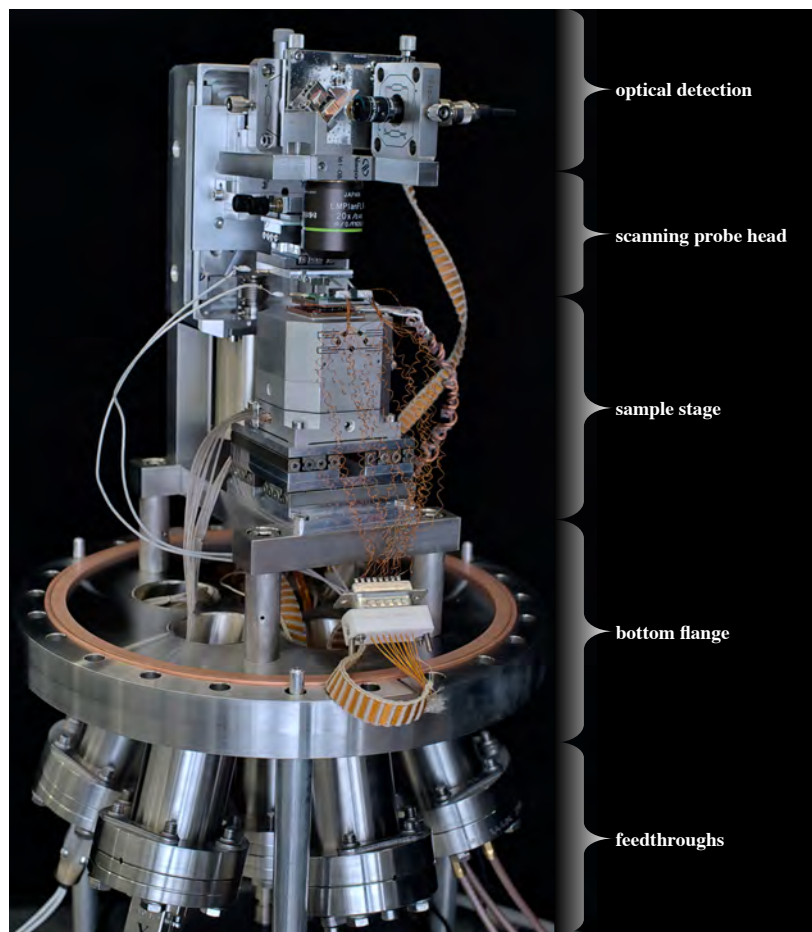


**Figure 2.3:** Photograph of the scanning thermal microscope mounted to the bottom flange of the vacuum chamber and comprising various components, such as the optical beam deflection detection, the scanning probe head and the sample stage.

tilt motion during regular contact-mode atomic force microscopy (AFM) operation, instead of an interferometric approach, as the focussing objective is simultaneously needed for visualization of the imaging region. Unconventionally, the entire OBD including the read-out electronics is housed inside the vacuum chamber, as close as possible to the optical signal acquisition by the photo diode. By including the electronic board into the vacuum chamber, we made a compromise between full UHV compatibility of the system and the complexity of optical signal acquisition, potentially capable for detection at very high bandwidth.

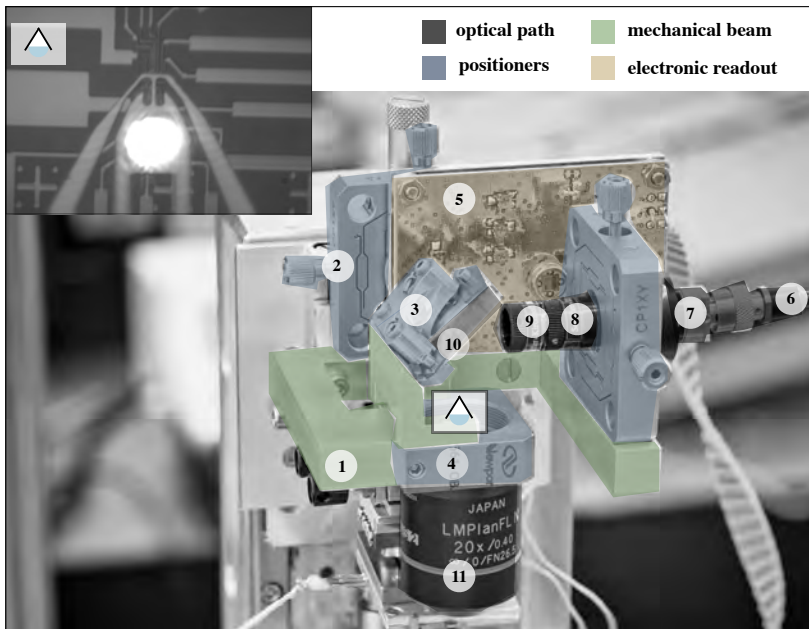


**Figure 2.4: The optical head of the microscope** illustrating the assembly of the optical beam deflection detection including different positioners, optical components and the electrical read-out board.

Fig. 2.4 shows an image of the optical head, indicating the optical components (6-10), the positioners (2-4) and the electronic readout board (5). All components are held by an aluminum beam (1), fixed to the slide of the z-axis coarse-positioner. The laser source is a 660-nm laser (51nanoFI from Schaefer Kirchhoff) specifically developed for application in scanning probe

systems. The laser source provides a strongly collimated polarized beam with a maximum output power of 6 mW. To avoid back-reflection of laser light into the laser cavity, we use fiber connectors with an angled physical contact (APC) connector (6) with an  $8^\circ$  angled polished fiber end. The laser light is coupled into the vacuum chamber via a polarization preserving single mode fiber, using a high-vacuum fiber feedthrough. The fiber end is attached to a collimator (7) followed by a polarizing beamsplitter cube (8) that is transparent to the incoming beam and redirects the back-reflected beam from the cantilever onto the photodiode detector directly attached to the electronic readout board. This is enabled by the  $\lambda/4$  wave-plate attached between the beam splitter cube and the focusing objective, which turns the linearly polarized light into circularly polarized light, rotating the beam polarization by  $45^\circ$  during each light passage. As the back-reflected beam passed the wave-plate two-times its polarization is in total rotated by  $90^\circ$  and therefore redirected by the beamsplitter cube onto the quad photo diode, through a hole that was drilled into the fixation ring of the cube, enabling redirecting of the laser beam. The photo-detector is directly soldered onto the electrical readout board built by B. Veselaj. The underlying electronics (5) are based on an original design by R. Enning et al. [73] and we refer to this work for further information.

Positioning of the laser beam path is achieved by various positioning ele-

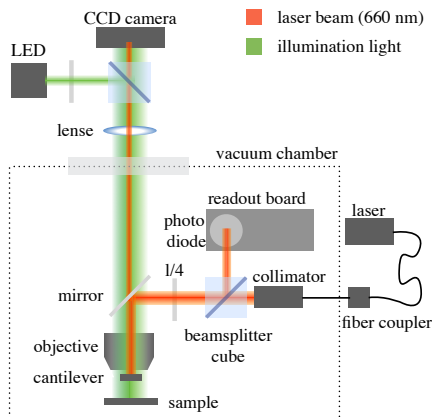


**Figure 2.5: Illustration of the optical detection principle** including a schematic of the laser beam path and the white-light illumination for optical visualization of the scanning probe.

ments. Fig. 2.5 provides a schematic of the beam path. The fiber collimator

is fixed by a lens holder (SM05 Thorlabs) screwed into a xy-flexure cage positioner (Thorlabs), which allows the laser beam to be adjusted via two manual micrometer screws in a range of  $\pm 1.5$  mm. For the initial coarse positioning of the laser beam, the entire flexure cages can be moved within a range of  $\sim \pm 5$  mm, inside grooves milled into the aluminum beam. The collimated laser beam is reflected into the objective by an  $45^\circ$  angled mirror (dichromatic shortpass filter 600 nm from Edmund Optics), mounted on a mirror hold with two degrees of freedom for fine adjustment. The laser beam is finally focused to the backside of the heatable scanning probe cantilever by the objective (Olympus LMPLFLN-BD) with a magnification of  $20 \times$  a working distance of 12 mm and a NA of 0.4.

Note that optical signal acquisition by the OBD using the thermal scanning probes is more challenging than with regular AFM cantilevers. The silicon cantilevers have a thickness of only 300-500 nm, comprise no reflective coating and are partially transparent for a 660-nm wavelength beam. In their original application as writing heads in probe-based memory cells [74], optical detection was not required, as topography sensing was accomplished by the distance-dependent heat flux signal of an integrated sensor resistor [45]. Here, we require traditional optical detection because the former approach cannot be applied under vacuum conditions. The optical topography detection is however limited by the partial transparency of the cantilever, giving rise to optical interference between reflections coming from the scanning probe and those coming from the substrate, as regularly observed in force-distance curves.

Another helpful component of our optical system is the optical microscope built on top of the main chamber (see Fig. 2.2). The optical image acquired by the CCD camera outside the vacuum chamber allows us to position the sample surface with respect to the cantilever, a very helpful feature to locate nanoscale device of typically no more than  $1 \times 1 \mu\text{m}$  in size. Moreover, it enables convenient alignment of the scanning probe cantilever with respect to the beam path of the detection laser, as the reflected laser spot on the cantilever can be directly visualized.

The last component of the optical system is the stereomicroscope, installed right in front of the quick-lock door. Although it is just a minor component of our thermal microscope setup, it turned out to be a critical element, as it enables sample exchange without the need to detach any cables. Nanoscale devices, in particular the nanowires studied in chapter 5, can be very sensitive to changes of the electronic connectors, potentially causing electrical discharges and the installation of the optical stereomicroscope diminished the accidental destruction of sensitive devices during the preparation handling.



## The sample stage system

Fig. 2.6 shows the sample stage system consisting of the xy-coarse positioner (1) carrying the piezo scanner (2), the Peltier heating/cooling stage (3) and the sample holder (4). The most important component of the sample stage is the closed-loop 3-axis piezo scanner (Mad CityLabs NanoHS3) directly mounted on top of the xy-coarse positioner. The scanner has a range of  $10\ \mu\text{m} \times 10\ \mu\text{m} \times 10\ \mu\text{m}$  and a step-size resolution of 0.3 nm. The coarse positioner consists of two piezo stick-slip stages (Smaract SLC2460), each having one parallel linear guide, mounted on top of each other. Each axis features a travel range of 24 mm, with a minimum nominal step size of 50 nm. For coarse positioning in the z-direction, the optical system and the probe head system are moved relative to the sample stage using a stepper-motor-driven spindle positioner (Pi-Micos PLS85-UHV). Here, we decided to use a mechanically robust positioner with a maximal load-carrying capability of 3.5 kg.

Another part of the sample stage system is the sample holder: a thin stainless-steel plate (7) with two threads in the corners, for fixation of our multi-pin probe card (6). The multi-pin probe card was designed to ensure free access to the scanning region from one side and to fit the contact-pad layout already established in the group in which this thesis was conducted. The probe card was fabricated by SQC Goldach according to our design. It is made from a PCB board with 14 copper beryllium needles. Two multi-pin connectors are directly soldered onto the probe card.

Below the sample holder is a Peltier stage, equipped with a temperature sensor (AD590MF) to set and control the sample temperature. The Peltier stage comprises a Peltier element sandwiched between two copper plates and can nominally create a temperature difference of  $\pm 70^\circ$  with respect to ambient temperature. The copper plates are bonded onto the Peltier element by thin indium foils. The temperature sensor is glued to the side of the copper top-plate, which has four glued-in magnets on the bottom side for mechanical fixation of the stainless steel sample plate. Currently, the Peltier stage can cool down the sample top side to  $\sim 0^\circ\text{C}$  and heat up to around  $100^\circ\text{C}$ .

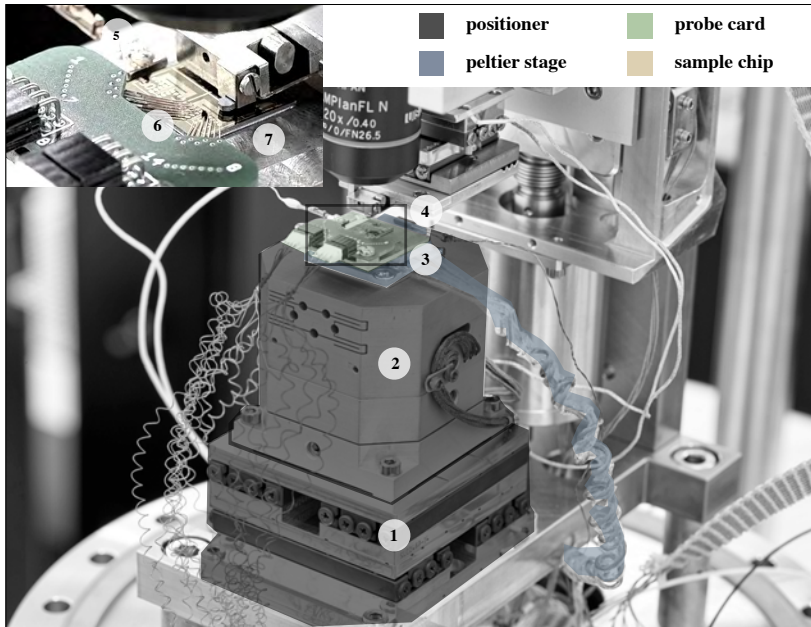


**Figure 2.6: Image of the sample stage system** including the xy-coarse positioner, the piezoscanner, the Peltier cooling-heating stage and the sample holder with the multi-pin probe card for electrical addressing of nanoscale devices.

## The scanning probe head

Fig. 2.7 shows an image of the scanning probe head, including a magnification of the cantilever region. The scanning probe head has an independent xyz-coarse positioner (1, 3), a major component of the microscope needed to align the cantilever with respect to the optical beam path and the sample surface. The probe head comprises a xy-positioner (3) (Smaract SLC2430), a manual xy-tilt (2) (Melles Griot MicroLab Low Profile) and a manual z-positioner (1). It is designed to ensure fast and free optical access to the cantilever holder. In combination with the optical microscope image, it allows precise positioning of the cantilever with sub-micron resolution.

The cantilever holder is mounted on the xy-coarse positioner, which has a travel range of 12 mm. The positioner is built from two linear piezo positioners (SLC2430 from Smaract), directly stacked on top of each other. This provides sufficient positioning flexibility to align the scanning probe cantilever in the optical beam path or moving it away from the objective for probe exchange. The manual z- and tilt-positioners were prepared for vacuum compatibility by removing the black anodization of aluminum and replacement of the greases.

The cantilever holder comprises a base plate with three glued-in magnets (4), three electrical contact pins and a clamping head (5) mechanism for the scanning probe designed by A. Knoll and fabricated by the IBM model shop. Three conical rods, screwed into the xy-positioner are used to define the position of the scanning probe holder, while the magnetic forces are used for mechanical fixation.

The scanning probe chip (6) gets clamped by a copper beam. The mechanical clamping mechanism is very beneficial to ensure reuse of the cantilevers. However, its implementation is challenging due to the space constraints related to the cantilever geometry and the difficulty to ensure straight positioning of the scanning probe on this length scale.

For scanning operation, the probe has to be tilted by an angle of  $(4-6)^\circ$  along the long axis of the probe, relative to the plane surface of the sample stage. Alignment of the probe angles is accomplished by the two-axis tilt positioner. As long as the tilt of a sample does not change significantly, no readjustment of the tilt angles is needed after an exchange of the scanning probe or the sample.

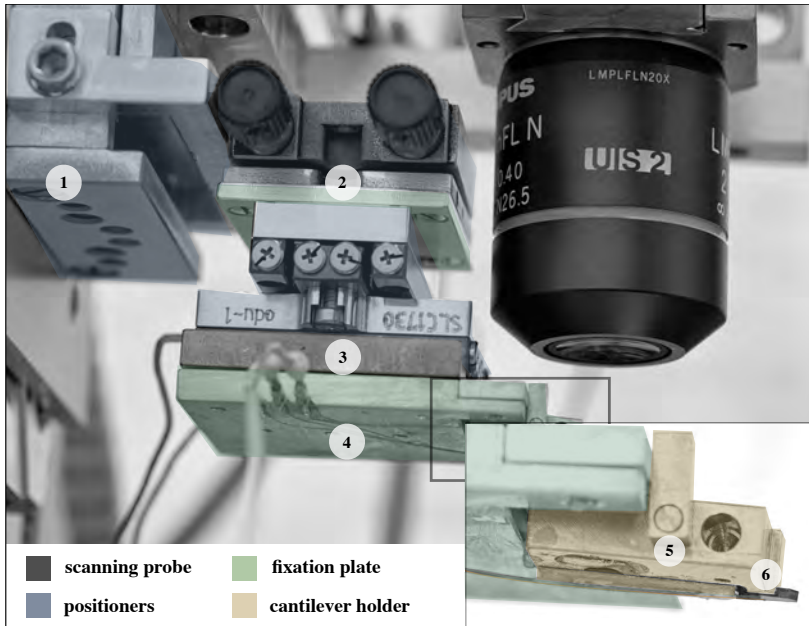


**Figure 2.7:** Image of the scanning probe head comprising the different positioners and the cantilever holder. The scanning probe is mechanically clamped by a copper beam coming from the side of the holder, not visible in the photo, while electrical contacts to the scanning probe are established by copper beryllium wires glued to a second copper beam on the bottom of the scanning probe holder.

## The resistively heatable silicon scanning probe

The resistively heatable silicon scanning probes used in this thesis were fabricated by U. Drechsler. The scanning probe consists of a mono-crystalline silicon body with large metal pads for electrical contacts. The chip is electrically contacted by copper beryllium wires glued to the copper beam of the holder as shown in Fig. 2.7. Fig. 2.8 shows a scanning electron microscopy

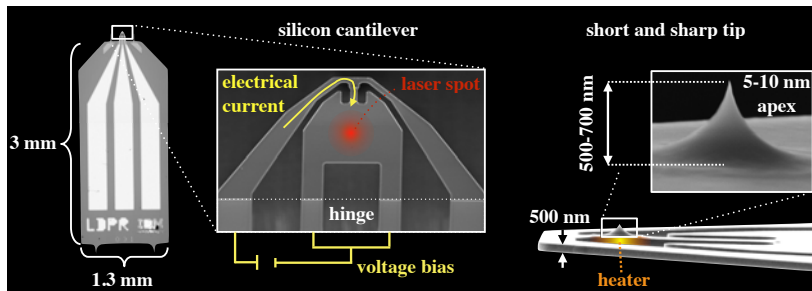


**Figure 2.8:** The resistively heatable silicon scanning probe illustrated by an optical image of the scanning probe chip and SEM micrographs of the cantilever indicating the electrical and optical sensing principle.

(SEM) image of the cantilever. Such micrographs provide insights about important cantilever characteristics and are regularly recorded before and after experiments. In particular, they provide information about the tip apex, its sharpness and opening angle. The tip-apex radius defines the tip-sample thermal resistance. The opening angle has a strong influence on the thermal resistance of the tip [45]. Typical probes have tips with a length of 500–700 nm and a sharp tip-apex radius of 5–10 nm initially. In certain experiments, knowledge about the thickness of the cantilever hinge is also useful as it defines the mechanical stiffness of the cantilever. Our typical cantilevers have a nominal spring constant of 0.15–0.20 N/m and a resonance frequency in the range of 50 kHz, making them well suited for contact-mode operation. The cantilever is highly phosphorus doped ( $10^{20}$  at/cm<sup>3</sup>) for good electrical conductivity. The heater region of  $(4 \times 6) \mu\text{m}$  below the tip has a nominal dopant density of  $5 \times 10^{17}$  at/cm<sup>3</sup>. The thermal resistance of the cantilever when situated in vacuum is typically  $2 \times 10^5$  K/W. The thermal resistance is mainly defined by the heat flux from the heater region along the anchor beams of the cantilever into the chip body. The thermal isolation of the heater region is maximized in a trade-off between the mechanical and thermal properties of the lever. For scanning probe operation, we require

a critical thickness of the cantilever, which is already a thin beam of only 300 nm in the region of the hinge. More than 90% of the total power dissipation in the cantilever occurs in the small region of the heater element below the tip. The heater equilibrates in a few microseconds. The electrical resistance is on the order of 1.2 k $\Omega$  at room temperature and increases to about 3.3 k $\Omega$  at 550 °C. Overall, the heater can be heated up to 1000 °C. Further details on the cantilever, its design and fabrication are reported by Drechsler et al. [33].

## 2.3 Instrument Control and Data Acquisition

Instrument control and data acquisition are built around an ADwin-Pro II real-time system. The ADwin-Pro II has an independent central processing unit (CPU) to execute all time-critical task in real-time, independently of the CPU of the measurement PC. This guarantees reliable operation of all deterministic functions, such as the scanner motion, independently of the workload of the measurement PC. The system is built in a modular fashion and capable of running multiple processes in parallel. Further details on the ADWin-Pro II system can be found on the company's website ([www.adwin.de](http://www.adwin.de)).

### The Instrument Control

When discussing the instrument control, we will differentiate between control related to the control of the vacuum system, control of the optical system, control of the scanning probe/sample system, and control of the scanner and positioner motion. Fig. 2.9 provides an overview of these four major blocks of the instrument control.

The vacuum control system comprises independent control units for the vacuum pumps and pressure gauges. Control of the vacuum environment is an important aspect of the experiments as the thermal measurements depend on a high-vacuum environment and a pressure in the range of  $10^{-7}$ - $10^{-6}$  mbar. The ion pump (Varian Noble Diode) and the turbo pump (Pfeiffer High-Pace 300) are directly connected to the MidiVac and Pfeiffer DCU control units. The pumps can be separated from the main chamber by manually controlled gate valves. The ion pump is running 24 h and just separated from the main chamber during sample and probe exchange, while the turbo pump is separated and switched off during the scanning probe experiments. The vacuum levels in the main chamber and pre-vacuum system are monitored by three different pressure gauges, namely the compact capacitance gauge, the full-range BA and a Pirani gauge. They are connected to the

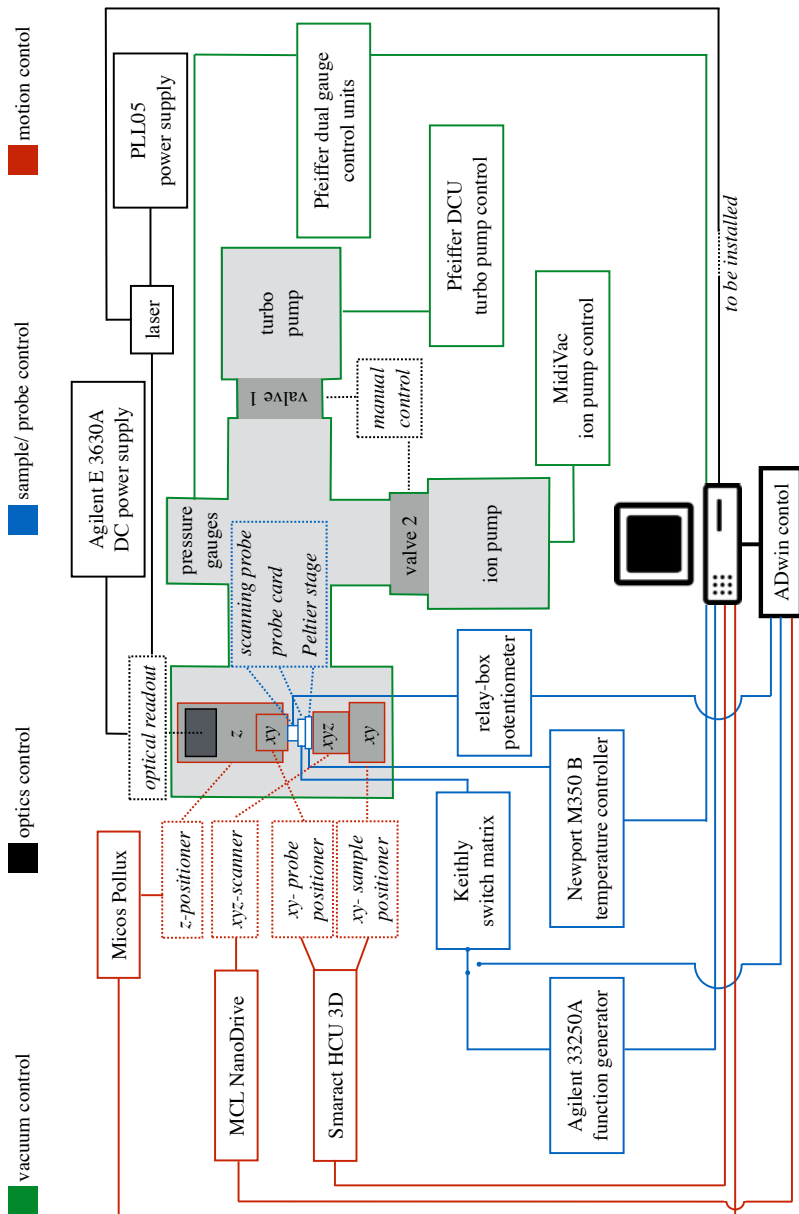


Figure 2.9: Schematic of instrument control and data acquisition system separated into control related the vacuum, the optics, the scanning probe/sample system, and the motion control.

Pfeiffer Dual gauge control units, which are programmed to automatically switch between the different sensing gauges in dependence of the vacuum level. The Dual gauges control units are connected to the measurement PC to read-out the pressure level, which allows switching off the high voltage supply of the piezo-scanner in case of any disturbances.

The major components of the optical control system consist of the laser connected to the PLL05 power supply and the optical readout board powered by a triple voltage DC power supply (Agilent E3630A). Control of the laser is not yet fully implemented and the laser intensity is manually adjusted by the potentiometer attached to the laser unit. A further development stage of the instrument will include an interface between the measurement PC and the laser.

The DC voltage supply used for the optical readout board also powers the relay card of the relay-box potentiometer, a part of the scanning probe/sample control system. Implementation of the relay-box potentiometer as automated potentiometer to compensate for voltage offsets in the heater/sensor resistor signal is a major improvement in the scanning probe control system. The relay-box potentiometer is implemented to realize an automated Wheatstone bridge for compensating the cantilever sensor voltage offset, as further discussed in the next section of the data acquisition. In each measurement the Wheatstone-bridge has to be balanced by adjusting the variable potentiometer, which can now be done either via a manual potentiometer or via the relay-box potentiometer. The relays are controlled via the digital output-input card (DOI) of the ADwin. The cantilever voltage bias is controlled by the ADwin digital-analog output card (DAC).

Other components of the scanning probe/sample system include the Agilent Function Generator (33250 A) as AC voltage supply for the sample devices. A manual switch to change between the ADwin DAC and the function generation as voltage supply, and a switch matrix (Keithly 7001) to address different needles of the multi-pin probe card. The temperature control of the Peltier stage is connected to the measurement PC and the Peltier element and the temperature sensor inside the vacuum chamber.

The motion control of the positioner and the scanner includes the control unit for the piezo-driven coarse positioner from Smaract (HCU-3D), the control for the stepper-motor-driven z-positioner from PI-Micos (Pollux) and the controller of the piezo-scanner from MadCitylabs (MCL NanoDrive). The first three channels of the ADwin DAC are connected to the MCL NanoDrive, the high-voltage amplifier/controller of the piezo scanner. The piezo-scanner is controlled by the DAC of the ADwin, which can deliver output voltage biases in a range from -10 to 10 V. A ten volt output bias correspond to the 10 m travel range of the piezo-scanner. For scanner motion a sinusoidal voltage signal is generated by the ADwin DAC.



Next we will discuss data acquisition and the processing of signals.

## Data Acquisition and Signal Processing

The central part of our the data acquisition is the ADwin real-time system. The independent CPU of the Adwin is connected to the measurement PC via Ethernet. The ADwin processes are programmed in ADBasic, a system-specific software development tool, executed from a higher-level Matlab interface on the measurement PC.

The ADwin system currently comprises one output card (DAC), one output-input card (DIO), and two analog-digital input cards (ADC). The ADC has a large local memory, which allows temporarily storing all data recorded during a measurement scan before the data is transferred to the PC for post-processing in Matlab. During this thesis, data acquisition speed could be enhanced up to 350 kHz.

Fig. 2.10 provides an overview about the acquisition of thermal signals, position and device signals.

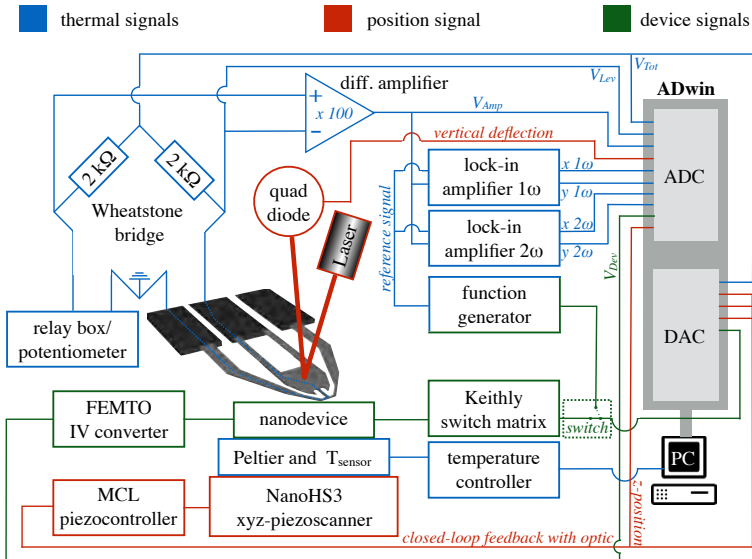


**Figure 2.10: Overview of the data acquisition** separated into thermal signals, position signals, and device related signals.

First, we will discuss the acquisition of thermal signals from the scanning probe. The scanning probe is powered by a DC voltage coming from the ADwin DAC. The output voltage is split behind the output, while one signal is read back as  $V_{Tot}$  and the second one is passed to the scanning probe cantilever. The voltage drop across the scanning probe is measured in a Wheatstone bridge configuration, comprising  $2k\Omega$  series resistors in each branch, of which one includes the scanning probe and the other a relay-box potentiometer for automated voltage offset compensation before the differential amplifier. The signal of the scanning probe branch is split before the differential amplifier, with one signal read back as  $V_{Lev}$  by the ADwin ADC and the second one going into the differential amplifier.

The differential amplifier (Stanford SR-640) is controlled via the measurement PC and used to filter (typical 50 kHz) and amplify the signal of the scanning probe with a typical gain of 40-60 dB. For a fully compensated bridge, the differential signal output of the amplifier contains the relative change of the scanning probe resistance in relation to the heat flux into the nanodevice. The amplified voltage signal is split, while one signal is passed to the ADwin ADC and the second line is passed to the lock-in amplifiers (Stanford SR-830), which are locked to the frequency of the AC voltage applied to the active nanoscale device under study. The lock-in amplifiers are recording the first and second harmonic of the amplified signal of the scanning probe. The implementation of a lock-in detection scheme for the active device measurement has greatly improved the temperature sensitivity in thermometry measurements as shown by the data presented in chapter 4 and chapter 5. The lock-in signals are recorded by the ADwin ADC and post-processed in Matlab.

The voltage bias across the nanodevice is constant and therefore not permanently recorded during measurement scans, but the device current-voltage response is initially characterized prior to the scans. A voltage is applied by DAC and directed to the device by adjustment of the Keithly switch matrix. A current amplifier (FEMTO DHPKA 100) is used to amplify the signal with a typical gain of  $10^3$  V/A. During measurement scans, the device is powered by an AC voltage bias coming from the Agilent function generator (33250 A), which is also connected to the reference input channels of the lock-in amplifiers for phase-sensitive detection of the scanning probe response.

A minor component of the thermal signal acquisition is the temperature signal of the Peltier sample stage recorded by a AD590MF temperature sensor connected to the temperature controller (Newport Model 350B). The temperature controller is connected to the measurement PC via a USB interface and allows one to acquire the sample temperature.

Apart from the thermal and device signals, acquisition of position signals is important for operation of the microscope. The position of the closed-loop

piezo-scanner is directly recorded from the sensors integrated into the scanner, by connection of the analog position signal output of the MCL piezo-controller to the ADwin ADC. For constant force operation, the vertical deflection signal of the scanning probe cantilever is recorded simultaneously by the optical beam deflection detection setup.

In the following sections we will illustrate how the instrument control and data acquisition can be applied for calibration and characterization of the scanning probe cantilever.

## 2.4 Calibration of the Heatable Scanning Probes

The first step towards quantitative scanning probe thermometry is to establish the correlation between the electrical resistance and the temperature of the scanning probe cantilevers. Therefore, each scanning probe sensor needs to be calibrated prior to experiments.

### Electrical Fix Point Calibration

Fix point calibration is a common approach for calibrating thermometers. Typically, the triple point, the freezing point or the melting point of some well-characterized substances, such as water, is used as reference for calibrating a thermometer. In our experiments we do not use a material's phase change, but the distinct change in the electrical conductivity of the silicon sensor as the calibration fix point.

First, we measure the current-voltage response (I-V curve) of the cantilever (see Fig. 2.11(a)) and calculate the corresponding resistance versus power relation as shown in Fig. 2.11(b). The current ( $I=(V_{Tot} - V_{Lev})/R_{series}$ ) is calculated from the voltage drop across the  $2\text{ k}\Omega$  series resistor in the Wheatstone bridge while sweeping the input voltage bias. The resistance increases typically from  $1.2\text{ k}\Omega$  up to  $3.3\text{ k}\Omega$  illustrating the strong temperature dependence of silicon's electrical resistance. In contrast to a simple linear relation, as in the case of a platinum resistance thermometer, we observe a more complicated dependence, reflecting the competition between increasing electron-phonon scattering with increasing temperature of the sensor and decreasing electrical resistance due to thermal excitation of intrinsic charge carriers into the silicon conduction band. The power dissipated at maximum resistance is our calibration fix point and specific for the given doping concentration of our heater/sensor element. The doping concentration determines the temperature required beyond which thermally excited, intrinsic charge carriers dominate conduction. Here, we refer to this temperature as intrinsic temperature  $T_{int}$ , which can be calculated as  $T_{heater} = T_{int} = 550^\circ\text{C}$  from the known doping level of the cantilever [60]. Based on the known intrinsic tem-

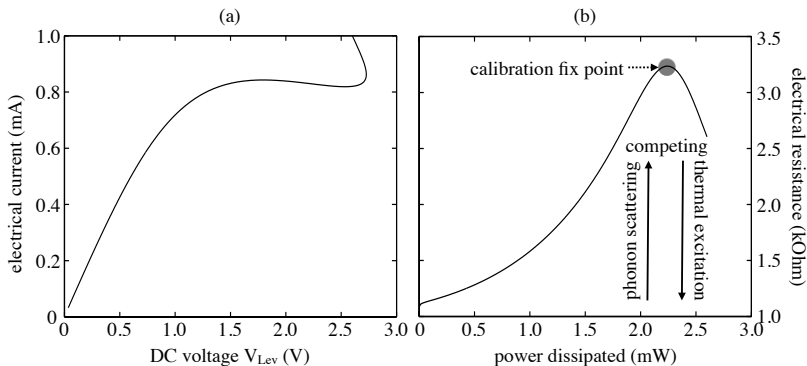


**Figure 2.11: Electrical fix point calibration**

(a) Shows the current voltage characteristic (I-V curve) of the scanning probe and (b) the corresponding power versus resistance dependence, reflecting the competition between phonon scattering related increase and thermal carrier excitation decrease of the resistance.

perature  $T_{int}$ , we calculate the thermal resistance of the cantilever as  $R_{th} = (T_{int} - T_{ambient})/P_{max}$ , where  $T_{ambient}$  denotes room temperature ( $20^\circ$ ) and  $P_{max}$  is the electrical power delivered to the cantilever at the resistance maximum. Knowing the electrical input power needed to reach  $T_{int}$  we determine arbitrary heater temperatures from linear scaling of the electrical input power as  $T_{heater} = T_{ambient} + P/P_{max} \times (T_{int} - T_{ambient})$ .

This procedure of electrical fix point calibration holds several assumptions. In particular, we assume (i) that the temperature at the resistance maximum can be predicted from the nominal doping level of the resistor, (ii) that the electrical input power  $P$  equals the heat flux  $\dot{Q}$  into the heater, and (iii) that the thermal resistance for heat flow away from the heater along the cantilever beams is independent of temperature. A detailed discussion of these assumptions, their validity and an error estimation can be found in the appendix. In total, we expect a combined uncertainty of determining the absolute cantilever heater temperature of about 20%. Note that this is a conservative estimation of the accuracy of the sensor temperature, while the resolution of the sensor ( $\sim 100 \mu\text{K}$ ) is significantly higher. To experimentally verify the electrical fix point calibration, various reference calibration measurements have been performed.

## Reference Calibration by Raman Thermometry

In a first approach, we applied Raman thermometry to determine the heater temperature in comparison to the fix point calibration method described above. The heater temperature was determined using a LabRam HR Raman microscope from Horiba with a 633 nm laser. The laser was focused directly onto the cantilever heater (as shown in Fig. 2.12(a), while significant laser-induced heating was avoided by using a laser power of only  $12 \mu\text{W}$ . As the Stokes peak position, frequently applied to infer temperature is potentially sensitive to mechanical strain in the cantilever, the heater temperature was measured using the Stokes/AntiStokes ratio according to the relation [75]:

$$\frac{I_S}{I_{AS}} = A \left( \frac{\omega_S}{\omega_{AS}} \right)^3 \exp \left( \frac{\hbar c \omega}{k_B T} \right), \quad (2.1)$$

where  $\omega_S$  and  $\omega_{AS}$  are the frequencies of the Stokes and AntiStokes photons,  $\hbar$  is Plancks constant,  $c$  the speed of light,  $\omega$  the optical phonon frequency,  $k_B$  Boltzmann's constant and  $T$  the absolute temperature. The constant  $A$  is determined by the absorption constants and Raman cross sections at the Stokes and AntiStokes frequencies and in our case  $A=0.675$ .

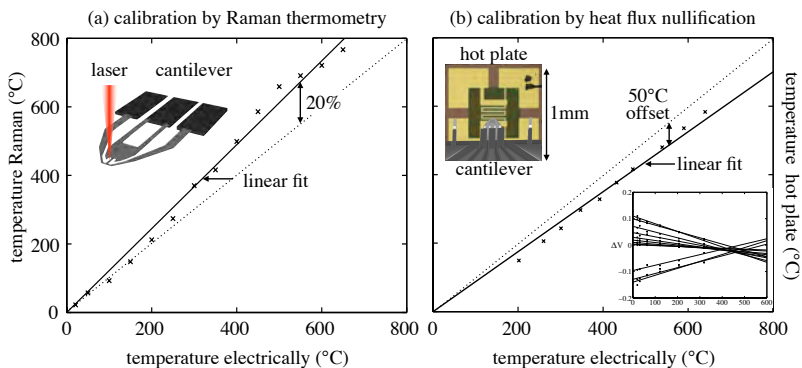


**Figure 2.12:** Heater temperature versus power dissipated as calibrated by Raman thermometry and electrically.

Fig. 2.12(a) shows the temperature of the sensor measured by Raman thermometry as a function of the electrically determined heater temperature. We observe a deviation between the temperature determined by the two different calibration methods, increasing with increasing power dissipated in the scanning probe. Applying a linear fit to the Raman temperatures we

observe a relative deviation of  $\sim 20\%$  between the two calibration methods as extracted from the difference in the slope of the linear fit in Fig. 2.12(a), indicating a temperature of about  $700^\circ\text{C}$  at the maximum electrical resistance of the scanning probe. The observed deviation is likely related to a lower doping concentration of the cantilever sensor than intended by the fabrication process. Still the absolute deviation is within the uncertainty of the estimated calibration error of the electrical fix point calibration. Note that a measurement accuracy of  $\sim 20\%$  is typical for thermal transport measurements on nanoscopic length scales and potential systematic errors in the calibration of the scanning probe cantilever effect all data points in a scanning probe measurements in the same way. Further details about the calibration of resistively heated silicon cantilever by Raman thermometry are reported by Nelson [43].

### Reference Calibration by Heat Flux Nullification

In addition, we performed calibration experiments based on nullification of the tip-sample heat flux. The idea of this calibration procedure is to adjust the temperature of the cantilever heater with respect to a known temperature of a reference sample until heat flux across the tip-sample contact becomes nullified and thermal equilibrium between the scanning probe heater and the hotplate is achieved. As temperature reference, we used a micro-hotplate from Kebaili Corporation (KMPH 100) calibrated by Raman thermometry (Fig. 2.12(b)).

As the hotplate material itself is not Raman active, silicon nanowires with a diameter of 80 nm were deposited on the hotplate surface. The hotplate was correspondingly calibrated directly from the temperature dependence of the Stokes first-order optical Raman shift of a nanowire in vacuum conditions. Here, mechanical strain effects are rather unlikely to interfere with a temperature induced shift of the Stokes peak. The Stokes peak position of the nanowire was observed to shift linearly with the electrical power dissipated in the hotplate. The slope of the Raman frequency shift versus power was found to be  $-0.22\text{ cm}^{-1}\text{mW}^{-1}$ . Assuming the slope of the Raman frequency shift versus temperature of silicon nanowires matches  $-0.022\text{ cm}^{-1}\text{C}^{-1}$  as previously reported [75], we determined the temperature dependence of the hotplate on the power dissipated to be  $10^4\text{ K/W}$ .

Knowing the temperature of the reference hotplate, the cantilever heater was calibrated by measuring the magnitude of the jump in the electrical signal  $\Delta V_{Amp}$  upon tip-sample contact by approach curves similar to those illustrated in the chapter 1.3.1. The magnitude of the measured signal jump

upon tip-sample contact is proportional to the heat flux between the heater and the hotplate and thus to the temperature difference and the thermal contact resistance. The inset in Fig. 2.12(b) shows the tip-sample voltage jumps upon contact measured at different cantilever power as function of the hot plate temperature. As the MEMS hotplate could not be heated up to 600 °C (maximum of  $\sim 300$  °C), we determined the temperature of thermal equilibrium between the cantilever heater and the hot plate by linear extrapolation of the voltage signal jumps, measured upon tip-sample contact for different heater temperatures, to zero heat flux, corresponding to the temperature where the scanning probe heater temperature equals the hot plate temperature. The extracted heater temperatures are plotted in Fig. 2.12(b) as function of the electrically calibrated heater temperature. By a linear fit, which corresponds to our assumption of a linear dependence of the heater temperature on the electrical power dissipated, we find a deviation between the two calibration methods of 12 %. The hot plate calibration via the heat flux nullification method indicates that the electrical fix point calibration is valid within our estimated uncertainty.

In summary, we illustrated the calibration of the scanning probe by three different methods. All three approaches can be applied to determine the temperature of the cantilever within our estimated uncertainty of 20%. For scanning probe experiments presented in the following chapters, the electrical fix point calibration is the method of choice and needs to be performed for each individual cantilever sensor prior to experiments, to establish the relation between the electrical and thermal properties. In the following section of this chapter, we will study the noise-limited thermal resolution of our thermal microscope.

## 2.5 Noise Characterization and Thermal Resolution

The following studies were conducted in attempts to locate and minimize external disturbances such as 50 Hz interferences onto our measurement signals. At the same time they provide interesting insights into the fundamental noise limits of our thermal microscope. A quantitative noise characterization of only the scanning probe sensor is beyond the scope of this section. We rather aim to characterize the noise of our DC thermal signal acquisition, representative for our experimental conditions, which includes additional noise sources like the Wheatstone bridge, the differential amplifier and the ADwin input and outputs.

The thermal resolution of the microscope is ultimately limited by the electri-

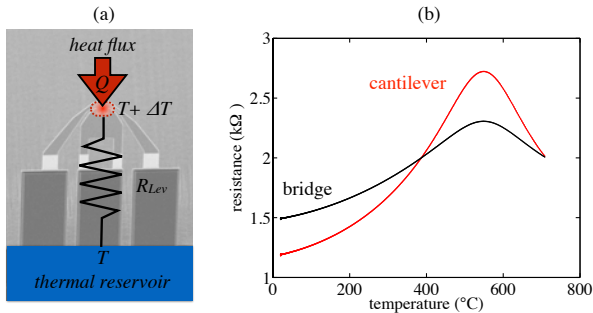


**Figure 2.13: The scanning probe heat flux sensor**

(a) Illustration of the scanning probe sensing principle, with a sensor heater exposed to a heat flux, separated from a thermal reservoir.(b) Resistance versus voltage dependence of the scanning probe sensor and the Wheatstone bridge

cal noise inherent to the voltage signal measured across the scanning probe sensor. The scanning probe is a kind of microscopic heat flux sensor with a thermal resolution related to the properties of the silicon sensor/heater resistor. Achieving high thermal resolution requires a high thermal resistance  $R_{Lev}$  of the sensor against its thermal reservoir (Fig. 2.13(a)) and precise measurement of the temperature change ( $\Delta T$ ) of the heater/sensor. The heat flux  $Q$  causing the temperature change, can be related to a tip-sample heat flux created in contact with a sample at a temperature different from the thermal reservoir or directly by self-heating of the sensor element in response to an applied sensing bias. The thermal resistance of the cantilever  $R_{Lev}$  against the thermal reservoir is a fixed property of the scanning probe and related to its particular design. The temperature resolution, however, is not just related to the inherent properties of the scanning probe but also to our measurement circuitry, ultimately limited by the electrical noise.

In our measurements, we apply a constant voltage bias  $V_{Tot}$  to the probe and infer changes in the sensor temperature from changes in the voltage bias measured across the scanning probe (see previous section). Fig. 2.13(b) shows the related change of the sensor resistance as function of the sensor temperature in comparison to the Wheatstone bridge equivalent resistance. The voltage at the differential amplifier input is sensitive to the intrinsic electrical noise of the cantilever sensor resistor ( $R_{Lev}$ ) within the Wheatstone bridge, as well as to external noise sources, interfering with the measurement. To quantify the electrical noise in our measurements, we measured the noise associated voltage signal spectral density ( $V_{SSD}$ ).



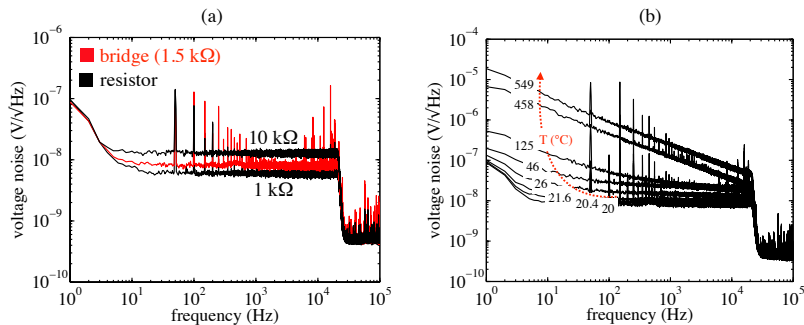


**Figure 2.14: Voltage signal spectral densities**

- (a) of the scanning probe sensor in the Wheatstone bridge in comparison to reference metal resistors  
 (b) of the self-heated scanning probe sensor at different temperatures.

Fig. 2.14 shows the  $V_{SSD}$  measured at ambient temperature in comparison to metal test resistors, with the filter edge at 20 kHz to exclude signal aliasing. Note that the signal spectra are not obtained by a single measurement but by hundred averages. Averaging allows one to resolve the fundamental noise level of the signal more clearly as it leads to a smoothing of the signal spectrum.

The noise of the sensing voltage illustrated in Fig. 2.14 has different components, which could be categorized into intrinsic noise and extrinsic noise. The intrinsic noise is mainly defined by the Johnson noise inherent to any electrical resistor and related to the thermal fluctuations of the charges in the resistor. The voltage signal of the Johnson noise can be calculated as  $V_{Johnson} = \sqrt{4k_B T R}$ , where  $k_B$  is Boltzmann's constant,  $T$  is the temperature and  $R$  is the electrical resistance of the resistor [76]. If we consider the scanning probe cantilever resistance only, we estimate a fundamental Johnson noise of  $4.4 \text{ nV}/\sqrt{\text{Hz}}$  for a 1.2-k $\Omega$  resistor at ambient temperature. However, the scanning probe is placed in a Wheatstone bridge configuration and the additional resistors contribute to the measured noise. Assuming that the Wheatstone bridge (two 2 k $\Omega$  series resistor and two 1.2 k $\Omega$ ) is balanced, the differential amplifier sees a resistance of 1.5 k $\Omega$  ( $2 \times 2 \times 1.2 / (2 + 1.2) \text{ k}\Omega$ ) corresponding to a slightly larger Johnson noise level of  $4.9 \text{ nV}/\sqrt{\text{Hz}}$ . Experimentally we observe a noise floor of  $7.8 \text{ nV}/\sqrt{\text{Hz}}$ . The offset is likely due to the input noise of the differential amplifier (Stanford SR 640), which has a nominal input noise of  $6 \text{ nV}/\sqrt{\text{Hz}}$ .

Apart from the intrinsic noise we observe discrete noise peaks, like those at 50 Hz and its higher harmonics, clearly related to extrinsic noise sources interfering with the measurement. Significant efforts were needed to minimize these 50 Hz-related noise peaks to about  $100 \text{ nV}/\sqrt{\text{Hz}}$ . The remaining noise interference, including peaks at higher frequencies, seems to be related to the earth ground of the instrument, which is a shared ground with all tools of the clean-room. Depending on time of day and the instrument operation, the peak magnitudes of 50 Hz-interferences can be observed to increase by up to one order of magnitude, without any changes in the measurement circuitry, indicating the dependence on the shared earth ground. A separate ground for the shielded laboratory is planned to be implemented in the future.

In order to estimate the temperature resolution in our measurements, we need to relate the  $V_{SSD}$  to the equivalent temperature signal spectral density ( $T_{SSD}$ ). The  $T_{SSD}$  is related to the  $V_{SSD}$  as

$$T_{SSD} = \frac{\partial T}{\partial R_{Lev}} \frac{\partial R_{Lev}}{\partial V_{Lev}} \times V_{SSD} \quad (2.2)$$

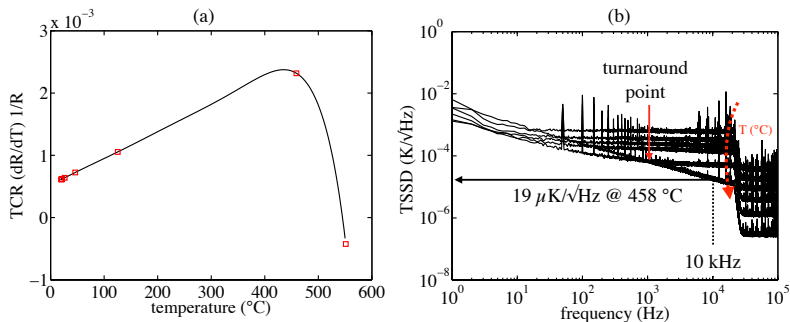
Equivalently, we can express Eq. 2.2 as

$$T_{SSD} = \frac{V_{SSD}}{TCR} \frac{R_{series} V_{Tot}}{R_{Lev} (V_{Tot} - V_{Lev})^2} \quad (2.3)$$

Illustrating that the signal is a function of the applied voltage bias, the  $2 \text{ k}\Omega$  series resistor in our Wheatstone bridge and the temperature coefficient of resistance (TCR) of the bridge.

Based on eq. 2.3, strategies to increase the temperature resolution of a thermal scanning probe sensor can be inferred. Eq. 2.3 illustrates that the  $T_{SSD}$  decreases with increasing voltage bias applied to the scanning probe. In common resistance thermometers this approach is typically not considered as a high sensing bias leads to self-heating in the sensor, which has to be avoided in equilibrium thermometry. Since our measurements are not based on thermal equilibrium between the scanning probe and the sample but on heat flux measurements, intentional self-heating is used to enhance temperature resolution.

Apart from increasing of the voltage bias, using a sensor with a high electrical resistance and a high TCR appears beneficial. Both properties are inherent to the material and geometry of the silicon sensor element of our scanning probe. The TCR of the equivalent resistance of the balanced Wheatstone bridge can be directly calculated from the resistance versus temperature dependence of the scanning probe, determined by the electrical fix-point calibration introduced in the previous section.



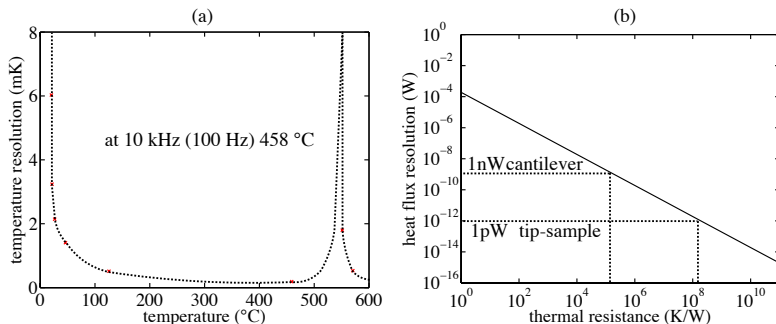
**Figure 2.15:** (a) Temperature coefficient of resistance (TCR) as a function of the sensor temperature and (b) equivalent temperature signal spectral density (TSSD) associated to the temperature noise in the scanning probe signal with time showing drift and change in noise rms (correlates to  $1/f$ )

Fig. 2.15 shows the TCR as function of the sensor temperature. The TCR initially increases nearly linearly with temperature reaching a maximum of  $\sim 2.5 (mK^{-1})$  followed by a decay, crossing a  $TCR=0$  at the maximum resistance in Fig. 2.13(b). Considering only the TCR, one might conclude that the optimal temperature resolution of the thermal scanning probe is at a temperature of about  $415^\circ C$ . However, the TCR is not to be confused with the temperature resolution of the scanning probe, which also depends on the electrical noise in the sensing voltage needed to quantify the electrical resistance of the sensor.

Predicting the temperature resolution of the sensor as function of the sensor temperature requires a temperature dependent analysis of the  $V_{SSD}$ . The voltage sensing bias has a temperature dependent noise that counteracts the benefits of the TCR initially increasing with temperature. This is illustrated in Fig. 2.14(b). We observe a strong increase of the low frequency noise. All noise sources contributing to this low frequency noise are collectively summarized as  $1/f$  noise, as the noise scaled as power spectral density is inversely proportional to frequency. While the Johnson noise could be approximated, the  $1/f$  noise is difficult to predict. One approach to estimate the low frequency noise is suggested by Hooge, who relates the  $1/f$ -noise signal to the number of charge carriers in the resistor as

$$V_{Hooge} = V_{Lev} \times \sqrt{\alpha/(Nf)} \quad (2.4)$$

with  $\alpha$  being the Hooge factor (on the order of  $10^{-5}$  and  $N$  the carrier density in the silicon sensor [76]. Eq. 2.4 indicates that Hooge noise is only relevant when a voltage bias is applied to the sensor and expected to increase with increasing bias. Additionally, the trapping and detrapping of charge carriers has been suggested to contribute to the  $1/f$  noise, leading to resistance fluctuations [76]. Fig. 2.14(b) illustrates the increase in low frequency noise by orders of magnitude. Combining the observed trends of the TCR and the temperature dependent  $V_{SSD}$  measurements, we can understand the temperature dependence of the temperature equivalent noise signals ( $T_{SSD}$ ) shown in Fig. 2.15(b). The  $T_{SSD}$  illustrates that the temperature noise initially decreases with temperature, indicated by the red-dotted arrow in Fig. 2.15(b). However, for higher temperatures the noise starts to increase in the lower frequency range with a turn-around point dependent on the frequency. If we consider, for example, the curve corresponding to a heater temperature of  $458^\circ\text{C}$ , we find that the temperature noise at frequencies up to  $1\text{ kHz}$  is enhanced due to the increasing  $1/f$  noise, corresponding to the significant temperature-dependent drifts of the scanning probe resistance typically observed at high temperatures. However, at higher frequencies we observe a reduction of the temperature noise, reflecting the competition between the increasing TCR and the increasing voltage noise. Although the voltage noise at  $458^\circ\text{C}$  is significantly larger than at lower temperatures over the entire frequency range (see Fig. 2.14(b)), the temperature-dependence of the TCR leads to a minimum in the temperature noise that can be approached at high frequencies, requiring a high total measurement bandwidth.



**Figure 2.16: Temperature noise and heat flux noise**

(a) Temperature noise estimated for a  $10\text{ kHz}$  frequency in a  $100\text{ nm}$  bandwidth as function of the sensor temperature, (b) heat flux resolution as function of thermal resistance, indicating the expected minimal heat flux that can be detected by the cantilever and across the tip-sample contact.

At a frequency of 10 kHz, a typical excitation frequency used in our lock-in thermometry measurements presented in chapters 4 and 5, we observe a temperature signal noise floor of  $19\mu\text{K}/\sqrt{\text{Hz}}$ . To estimate of the temperature noise equivalent to our DC measurements, we would need to integrate the noise signal over the entire relevant frequency from about 1 to 10 kHz. However, in our thermometry measurements, we reduce the bandwidth to about 100 Hz using a lock-in amplifier. Exemplary, we will estimate here the temperature resolution at 10 kHz in a 100 Hz bandwidth as ( $T_{noise} = T_{SSD}(10\text{ kHz}) \times \sqrt{100\text{ Hz}}$ ), as representative for our thermometry measurements, which corresponds to a temperature resolution of the sensor of  $T_{res}=190\mu\text{K}$ . Note, that this temperature resolution is a function of the sensor temperature. Fig. 2.16(a) illustrates that the temperature resolution is in a sub-mK regime for a broad temperature range from about 100 to 500 °C for the particular frequency and bandwidth. Fig. 2.16(a) directly illustrates that intentional self-heating of the scanning probe sensor to a temperature of about 400 °C is beneficial to optimize the temperature resolution.

Apart from the temperature resolution we are interested to estimate a heat flux resolution of our scanning probe ( $Q_{res} = T_{res}/R_{Lev}$ ), which depends on the thermal resistance of the cantilever against its thermal reservoir. Considering a typical thermal resistance of the cantilever of  $2 \times 10^5\text{ K/W}$ , we expect that a heat flux as small as 1 nW can be resolved in a bandwidth of 100 Hz (see Fig. 2.16(b)). The thermal resistance of the tip-sample contact is approximately three orders of magnitude larger, indicating a heat flux noise of 1 pW for a  $2 \times 10^8\text{ K/W}$  tip-sample thermal resistance. We will experimentally demonstrate heat flux measurements approaching this picoWatt regime in chapter 4 of the thesis.

In numerous experiments we are interested to sensitively probe variations of tip-sample thermal conductance, like in the experiments presented in the next chapter on graphene. The thermal conductance resolution is related to the heat flux and the equivalent thermal conductance noise can be estimated as  $G = Q_{res}/(T_{heater} - T_{ambient})$ . This indicates that the conductance noise gets minimized with increasing temperature bias between the scanning probe and the sample. Based on Fig. 2.16(a), we can conclude that the heater temperature can be increased to about (100-500) °C without significant reduction of the temperature resolution and consequently the heat flux resolution. Accordingly, thermal conductance or resistance measurements as those presented in the next chapter are preferentially to be performed at a temperature of about 400 °C. Assuming a 1 nW heat flux resolution of the scanning probe cantilever and a temperature bias of 400 °C between the scanning probe heater and the sample we can estimate an equivalent thermal conductance noise of 2.5 pW/K. Such a conductance

resolution would be sufficient to probe thermal transport across individual molecules. A temperature difference of  $400\text{ }^{\circ}\text{C}$  across a molecule would be a rather large. Still, a stable measurement arrangement can be expected as long as the molecular is well coupled to a substrate. A significant heat flow across the molecule is not expected, due to the large thermal resistance of the atomic sized contacts. An atomic contact is expected to have only a thermal conductance of  $0.6\text{ nW/K}$ , corresponding to the thermal conductance quantum at  $400\text{ }^{\circ}\text{C}$ . Experimentally, we already demonstrated thermal conductance studies across self-assembled monolayers [77] and in chapter 3 we will present thermal transport measurements across individual graphene layers.

Our discussion indicates the fundamental limits for our thermal measurements related to the intrinsic properties of our silicon scanning probe and our measurement circuitry. Approaching this intrinsic noise limit in experiments is challenging. In chapters 4 and 5, we will presented experimental results approaching the thermal resolution limits estimated in this section, while those measurements presented in the next chapter illustrate the achievable thermal resistance resolution in a DC scanning probe measurement at higher bandwidth.

## 2.6 Conclusions

In summary, we reported on the design and the construction of a new high-vacuum scanning thermal microscope. We illustrated and described all key-components of the instrument such as the optical beam deflection detection, the scanning probe head and the sample stage. The major principles of the instrument control and the data acquisition were introduced. Furthermore, we presented different experiments for calibration of the resistive silicon scanning probes, of which the electrical fix-point-calibration was identified as the method of choice. Calibration of each scanning probe is required prior to experiments to establish the relation between the electrical and thermal properties of the sensor resistor.

Finally, we characterized the electrical noise of the thermal data acquisition. We measured a voltage signal noise floor of  $7.8 \text{ nV}/\sqrt{\text{Hz}}$ , which is within a factor of two of the estimated fundamental Johnson noise limit of the instrument. We related the measured electrical noise to an equivalent temperature signal noise level of about  $40 \mu\text{K}/\sqrt{(\text{Hz})}$  at a sensor temperature of about  $400^\circ\text{C}$ , a typical temperature used in our experiments. Assuming typical measurement conditions for thermometry experiments, we estimated a sub-mK temperature resolution of the scanning probe for experiments at 10 kHz in a 100 Hz bandwidth, corresponding to pico-Watt per Kelvin conductance sensitivity. By further reduction of the bandwidth, which is however difficult to combine with scanning mode operation of the microscope, we approach thermal resolution limits equaling those of the best reported resistance thermometers used in nanocalorimetry measurements [78]. In contrast to our microscope, such instruments have no spatially resolved imaging capability. Based on the noise characterization and the thermal resolution estimation, we expect an outstanding performance of the microscope in experiments.

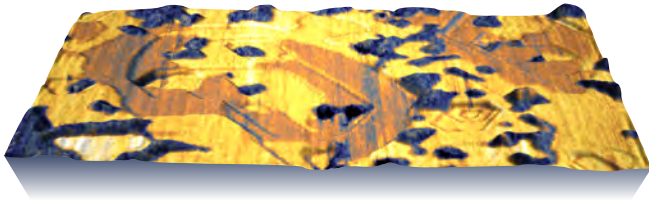
In the following chapters we show a variety of experiments, where the instrument is used to study thermal transport across individual atomic layers, self-heating of metal interconnects and local electro-thermal processes in nanowire devices. These experimental studies will directly illustrate the performance of the instrument.





# 3

## Mapping Thermal Resistance Modulations across Graphenes



In this chapter, we use the heated tip of a scanning thermal microscope cantilever to study thermal transport across graphene layers. We probe heat dissipation into sheets of different thickness, on both high and low conductive substrates. Our studies reveal a competition between interface-related suppression and spreading assisted enhancement of heat dissipation as a function of graphene layer thickness. A significant advance of our work is the quantification of thermal resistance modulations down to sub-10 nm lateral thermal resolution with sensitivity for the individual atomic layers. Our experiments provide deeper insights into the fundamentals of heat dissipation across graphene in nanoscopic contacts, graphene's potential as an atomically thin heat spreader and the high-performance of our scanning thermal microscope.

### 3.1 An Atomic Sheet for Heat Spreading

Recently, the integration of graphene heat spreaders was suggested to promote heat removal in nanoelectronics [79–82]. This application of graphene is motivated by an increasing relevance of local self-heating on nanoscale devices and numerous publications on the thermal conductivity [83, 84] of graphene, which holds the world-record. Impressive conductivities of up to  $\sim 5000$  W/(mK) [83] may suggest its suitability for heat removal. However, because graphenes thermal conductivities strongly depend on the size [85–88], the direction [89] and in particular on the configuration (e.g. suspended [83], supported [90] or encased [87]), one may question whether atomic sheets of carbon are generally suited as a heat spreader. Fig. 3.1 provides an overview of thermal conductivities of graphenes in dependence of the heat flow direction (in-plane versus cross-plane). Note that the term graphenes is used to describe single to few-layers of graphite sheets ( $\sim 1$ -10 layers).

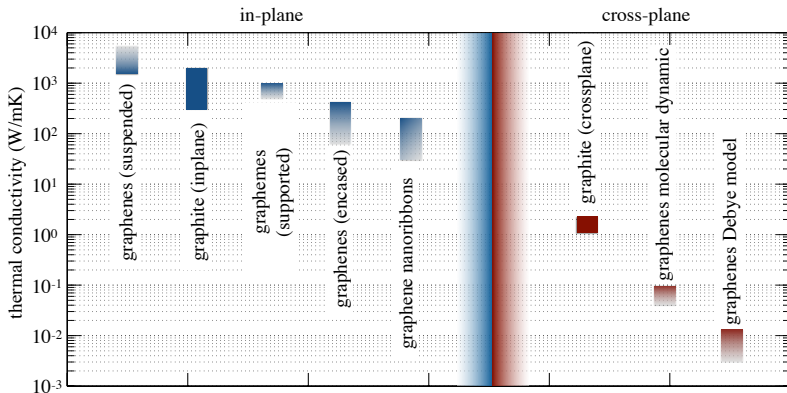


**Figure 3.1: Overview about in-plane and cross-plane thermal conductivities of graphenes**

The color trend in the bars represents the overall thickness dependence of thermal conductivity for each particular case. The inplane-thermal conductivities correspond to experimental values, reported in a review article by Pop et al. [91]. For the cross-plane direction only the graphite value corresponds to an experimental value [84], while the other two bars correspond to predictions of graphenes cross-plane conductivities based on a molecular dynamic simulation [92] and an approximation based on the Debye model [93].

One can immediately realize an enormous diversity in graphenes thermal conductivities spanning six orders of magnitude. This variety is important to note as in most potential device structures, graphenes are embedded

into or at least supported by some adjacent material that strongly affects graphenes intrinsic thermal transport properties. Nearby materials cannot only affect the absolute conductivity but also the thickness dependent trend of thermal conductivity can reverse in response to extrinsic effects. We refrain in this introduction from a further discussion of graphenes thermal conductivities, but refer to comprehensive reviews by Balandin [84], Pop et al. [91] and Sadeghi et al. [94], highlighting that the thermal conductivity of a material, in this case graphite, is not an intrinsic property but size dependent. Accordingly, the bulk thermal conductivity is hardly suited to predict the thermal transport property of a nanostructure without detailed structural information.

In fact, the technical realization of graphene heat spreaders is likely to require not only detailed knowledge of the intrinsic thermal properties of graphenes, but also a fundamental understanding of heat dissipation from nanoscopic contacts. A weak thermal coupling between a hot spot and a graphene heat spreader may turn out as a fundamental bottleneck for the predicted applications. Well-established experimental techniques to characterize graphenes thermal transport properties, either optically (e.g by Raman spectroscopy [95], time-domain thermoreflectance [96]) or electrically (e.g., by microscopic heater bridge [97], 3-omega configurations [87]) do not provide the spatial resolution to resolve heat dissipation down to the range of single nanometers. This is in particular problematic as on this length scale interface effects and quasi-ballistic transport properties dominate the superior intrinsic thermal conductivities of graphene sheets, ultimately limiting the development of potential applications.

Consequently, the need to study thermal transport properties with high spatial resolution, as well as the potential application of graphene in heat removal, motivate the investigation of graphene structures by scanning thermal microscopy. In this chapter, we are not aiming to quantify thermal conductivity of graphene sheets by scanning thermal microscopy, adding a further data point to Fig. 3.1, but we rather aim to study the yet unexplored dissipation of heat into graphene from nanoscopic heat sources. SThM provides the spatial resolution needed to gain insights about graphenes quasi-ballistic thermal transport properties [19, 55], which gains significance as the size of a hot spot is reduced to a size smaller than the actual phonon mean free path (mfp) of its surrounding. Interestingly, the tip of our resistive scanning probe can be used beyond direct visualization of local hot spots and temperature fields [27], also to act as nanoscale heat source. This is advantageous for understanding the fundamentals of heat dissipation across nanoscopic contacts [53], in particular across graphene. The hot tip apex forms contacts on the order of nanometers, essentially acting as variable hot spots. Since the hot contact can be moved to different locations, heat dissipation can be di-

rectly studied as a function of different parameters, such as the thickness of a graphene layer or the properties of a supporting substrate, e.g., roughness or material composition. While the ability for spatially resolved heat transfer studies in correlation to individual atomic layers is certainly promising for the further development of thermal nanoscience and engineering, it poses a challenge to the technique of SThM, and qualifies as a first test for the performance of our scanning thermal microscope.

### 3.2 Thermal Transport into Graphene on Silicon Dioxide

First, we studied thickness-dependent thermal transport modulations into graphene adsorbed on silicon dioxide ( $\text{SiO}_2$ ) [55]. Graphene flakes were prepared by mechanical exfoliation on a silicon wafer with 300 nm of silicon oxide.

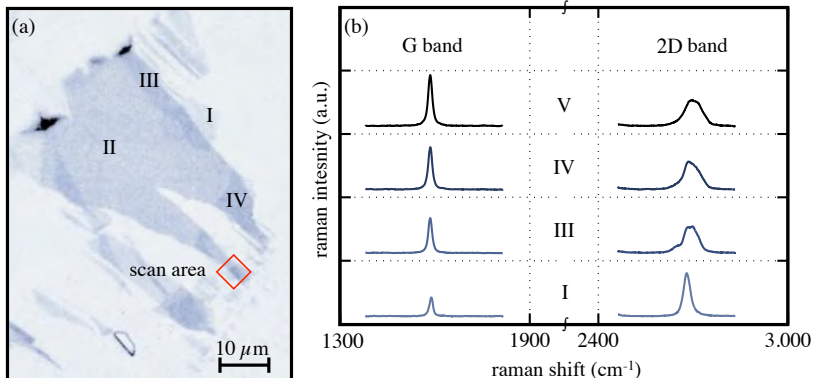


**Figure 3.2: Identification of graphene layers on  $\text{SiO}_2$**

by (a) an optical microscopy image and (b) Raman intensities of exfoliated graphene sheets as function of the layer thickness

An optical microscopy image of the graphene flakes studied is shown in Fig. 3.2(a). Optical microscopy is sufficient for screening large wafer areas for potential graphene flakes after the fabrication process. Nevertheless, the direct identification of absolute layer thickness can be challenging, either because of vanishing optical contrast or the small flake size. We verified the number of graphene sheets as depicted in the following studies by Raman spectroscopy, which allows identification of the layer thickness [98]. The

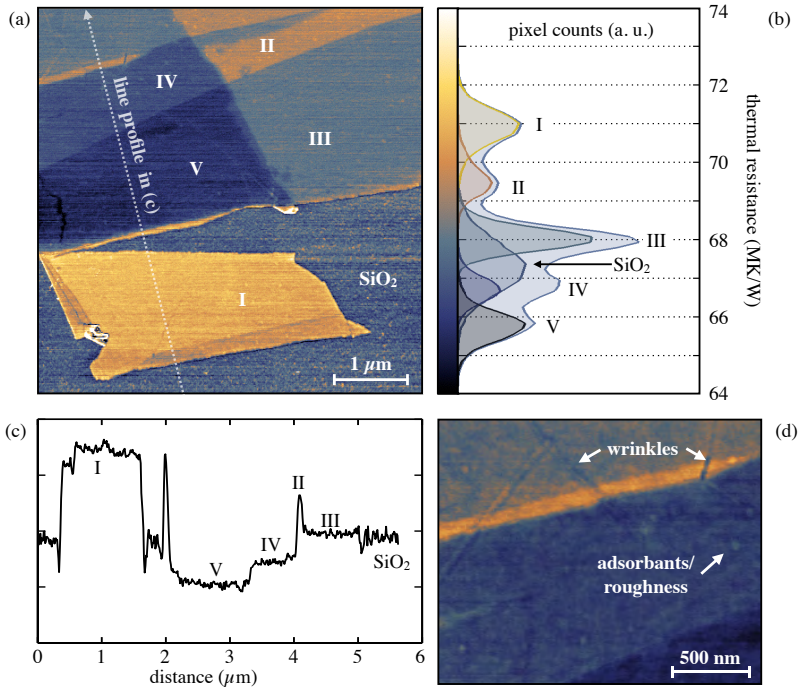


**Figure 3.3: Thermal resistance across graphene layers on SiO<sub>2</sub>**

(a) Thermal resistance image of graphene on SiO<sub>2</sub> (b) Image pixels vs. thermal resistance of the entire image and different layer regions, (c) Thermal resistance profile along layers of varying thickness, (d) Thermal resistance image at higher resolution, indicating the presence of wrinkles, surface roughness and possible adsorbates.

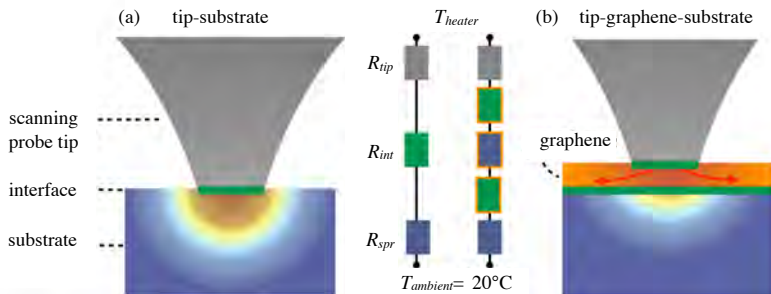
measurements were conducted using a LabRam HR Raman microscope from Horiba with a 633 nm laser in collaboration with E. Lörtscher. The results shown in Fig. 3.2(b), reveal the different layer thicknesses by changes of the characteristic shape, position, and intensity of the Raman G and 2D bands. While the single-layer graphene can be easily identified by the unique symmetric shape of its 2D band, it broadens and blue-shifts as the thickness of the graphene is increased. At the same time, the intensity of the G band increases linearly with layer thickness, as shown in Fig. 3.2(b). Details on the identification of the graphene layer thickness by Raman spectroscopy can be found in previous reports [98].

Fig. 3.3(a) shows a thermal image of the graphene flakes on SiO<sub>2</sub> as measured

in the region depicted in Fig. 3.2(a). The tip was raster-scanned in contact mode, with a heater temperature of  $\sim 770^\circ\text{C}$  and the sample at ambient temperature ( $T_{RT} = 20^\circ\text{C}$ ). The signal, scaled as a variation of the tip-sample thermal resistance, clearly correlates with the number of graphene layers. The brightest region corresponds to a single atomic layer, exhibiting the highest thermal resistance. With increasing number of graphene sheets the resistance decreases, dropping below the thermal resistance on bare silicon oxide for more than three layers. This can be inferred from the histogram plots in Fig. 3.3(b), which shows the image pixel counts versus thermal resistance for the entire image as well as for the different layer regions identified in Fig. 3.3(a). The thermal resistance profile in Fig. 3.3(c) reveals that silicon oxide and three layers of graphene have nearly the same thermal resistance. The thermal resistance profile corresponds to the location indicated by the line in Fig. 3.3(a) and slightly extends outside of the scan range of the presented image. Interestingly, the signal variation on the graphene sheets are smaller compared to those on the bare  $\text{SiO}_2$ , which indicates damping of the underlying surface roughness that may also relate to the thermal resistance measured by the thermal scanning probe.

At higher spatial resolution, we can observe wrinkles and nanoscopic thermal resistance variations, like those shown in Fig. 3.3(d). The thermal contrast at wrinkles appears to be dominated by the topography related change in the tip-sample contact geometry, rather than a local variation of the thermal coupling strength between the graphene sheet and the underlying substrate. Local inhomogeneities in thermal resistance within individual sheets of constant thickness may be related to the roughness of the underlying substrate and/or adsorbates, modifying the tip-graphene interaction respectively the graphene-substrate thermal interface resistance. Previous scanning probe studies have shown that hydrocarbons and water adsorbates are frequently present on the surface of graphene [99]. While the origin of these local signal variations remains unclear it is interesting to note this qualitative observation as it indicates sufficient sensitivity of our scanning thermal microscope to study thermal transport variations even beyond the identification of individual atomic layers [77].

Given the experimental data of Fig. 3.3, we aim to further investigate the thickness dependence of the thermal resistance across graphene. Qualitatively, we can understand the observed trend by first considering the case of the tip being in contact with the  $\text{SiO}_2$  substrate, as illustrated in Fig. 3.4(a). A more quantitative interpretation and justification of the diffusive thermal transport picture illustrated in Fig. 3.4 follows in the next section. The tip-sample thermal resistance depends on the thermal resistance of the tip ( $R_{tip}$ ), the thermal interface resistance ( $R_{int}$ ), and the thermal resistance of the substrate ( $R_{spr}$ ). As a graphene sheet enters the heat flow path (see



**Figure 3.4: Measurement Geometry**

Schematic of the nanoscopic tip-sample contact (a) without and (b) with graphene layers. The heat flux is modulated by variations in the thermal spreading resistance ( $R_{spr}$ ) and the thermal interface resistance ( $R_{int}$ ), while the resistance of the tip ( $R_{tip}$ ) is constant.

Fig. 3.4(b), the thermal resistance changes as the contact changes from a tip-SiO<sub>2</sub> contact to a tip-graphene-SiO<sub>2</sub> contact. Both the thermal interface ( $R_{int}$ ) and the spreading resistance ( $R_{spr}$ ) are expected to vary. Experimentally, we observe a resistance increase from  $(6.73 \pm 0.08) \times 10^7$  K/W on bare SiO<sub>2</sub> to  $(7.09 \pm 0.06) \times 10^7$  K/W with a single graphene layer (SLG). Considering graphene as higher conductive layer on top of a lower conductive, amorphous oxide, the resistance increase must be related to the newly formed interfaces at the top and bottom of the SLG, acting as phonon-scattering sites within the conduction path. This resistance increase may be surprising, considering the reported high in-plane thermal conductivity ( $\sim 600$  W/(mK) [97]) of graphene on silicon oxide. It indicates that heat dissipation by potentially enhanced lateral spreading within the graphene sheet is poor when taking into account the additional resistances of the newly formed interfaces.

This is a key experimental observation of this work. The single atomic layer blocks heat dissipation from the nanoscopic contact formed by the hot tip. The graphene sheet acts as a thermal barrier instead of promoting heat removal. At the same time, our experiments reveal a continuous decrease of thermal resistance with increasing thickness of the graphene sheet. While the absolute thickness to promote heat removal may depend on the size of the hot contact (see discussion in the next section), the observed trend of decreasing thermal resistance with increasing layer thickness appears as universal feature indicating the potential of few-layer graphene as an ultimately scaled heat spreader.

### 3.3 An Analytical Model of Heat Spreading into Graphene

Next we rationalize our results independently of the particular tip used for the experiments by relating the experimentally observed trend of thickness-dependent thermal transport to an analytical model of heat spreading. We aim for an intuitive description of the observed thickness-dependence and a simple model to predict heat dissipation from nanoscopic hot spots. First, we will justify the choice of a diffusive transport model for further analysis as this is a strong assumption considering the nanoscopic scales in our experiment.

Within the amorphous  $\text{SiO}_2$  substrate (nominal thermal conductivity of  $\kappa_{\text{SiO}_2}=1.4 \text{ W/mK}$ ), we can safely describe heat conduction as diffusive as the estimated size of the tip-sample contact ( $a=(12.5\pm 2.5) \text{ nm}$ ) is more than one order of magnitude larger than the average phonon mfp of  $\text{SiO}_2$  ( $\sim 0.5 \text{ nm}$ ). Within the graphene layer, a diffusive description of thermal transport may become less valid as our experiment is sensitive to both, in-plane and cross-plane properties. A diffusive transport model appears useful for the cross-plane direction, where thermal conductance has been predicted to scale as  $G_c \propto t_0^{-1}$ , with  $t_0$  being the thickness of the graphene layer [92]. This proportionality is typical for diffusive transport (Fourier's law), indicating that the majority of heat carrying phonons gets scattered between the weakly van-der-Waals-coupled sheets.

For the in-plane direction, strong dependencies of thermal transport on extrinsic scattering mechanism are reported. While suspended graphene sheets show highly ballistic transport properties, a cross-over from ballistic to diffusive heat flow regime has been observed for supported graphene nanoribbons [88]. Boundaries and adjacent materials such as the  $\text{SiO}_2$  substrate or the tip contact in our experiments can act as phonon-scattering sites that strongly suppress heat conduction in the in-plane direction of graphene. Considering these extrinsic effects on graphene's intrinsically high in-plane thermal conductivity we expect the dominant in-plane phonon mfp to be on the order of the heated contact length between our scanning probe tip and the sample. This estimation is supported by the absence of both a thermal resistance increase towards edges of the graphene flakes and a measurable flake size dependence of thermal resistance in our experiments. Taking these considerations into account, we apply a diffusive heat-spreading model for the qualitative explanation of our experimental observations.

To this end, we consider the tip-sample thermal resistance  $R_{ts}$  between our heated tip and the sample as the sum of several resistances (see illustration



in Fig. 4.5) and we define

$$R_{ts}(n) = R_{tip} + R_{int} + R_{spr}(n). \quad (3.1)$$

The unknown resistance of the tip ( $R_{tip}$ ) is expected to be independent of the layer number ( $n$ ) and is used as fitting parameter in the further analysis. The thermal interface resistance, ( $R_{int}$ ), between the tip (covered by a native oxide shell) and the graphene layers is assumed as constant since the thermal interface resistivity of the graphene/SiO<sub>2</sub> contact has been reported as independent of ( $n$ ) [100], and the size of the contact does not significantly change during one scan. We estimated  $R_{int}=2 \times 10^7$  K/W using a typically reported thermal interface resistivity of  $r_{intG}=1 \times 10^{-8}$  (m<sup>2</sup>K)/W for graphene/SiO<sub>2</sub> contacts, as values ranging from  $5.1 \times 10^{-9}$  (m<sup>2</sup>K)/W to  $4 \times 10^{-8}$  (m<sup>2</sup>K)/W [88, 90] haven been reported. Uncertainties in this value are included in the fitting parameter ( $R_{tip}$ ).

This attributes the experimentally observed thermal resistance variations to a thickness-dependence of heat spreading within a structure consisting of the thermally orthotropic graphene layer separated by an interface from the amorphous SiO<sub>2</sub> substrate (see Fig. 4.6). To describe the heat spread-

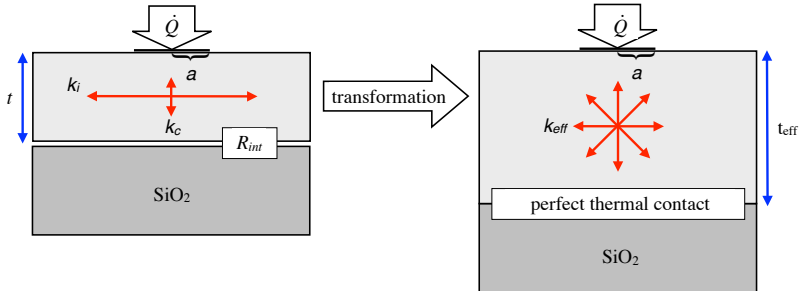


**Figure 3.5: Schematic of the geometrical transformation approach**

to scale an orthotropic graphene/SiO<sub>2</sub> structure into an isotropic structure with effective thermal conductivity and thickness of the layer by conductivity and thickness transformation.

ing, we consider the heated contact as an isothermal circular heat source of radius  $a = 12.5$  nm in perfect thermal contact with the graphene sheet. The thermal spreading resistance around such a hot spot in contact with a graphene sheet on top of a lower conductive SiO<sub>2</sub> substrate has no closed-form analytic expression. However, we suggest to derive an analytical approximate solution [101] based on creation of a thermally equivalent system as depicted in Fig. 4.6, consisting of an effectively isotropic graphene layer in

perfect thermal contact with the SiO<sub>2</sub> substrate. Here, we approximate the graphene-SiO<sub>2</sub> structure, consisting of an orthotropic layer separated by an interface from an isotropic substrate to a fully isotropic system by performing thickness and conductivity transformations of the thermal conductivity and the physical thickness of the layer as derived by Muzychka [102] and including the thermal interface resistance between the layer and the SiO<sub>2</sub> substrate as additional effective thickness.

$$k_{eff}(n) = \sqrt{k_i(n) \times k_c(n)} \quad (3.2)$$

$$t_{eff} = n * t_o \sqrt{k_i/k_c} + r_{intG} \kappa_{eff}(n) \quad (3.3)$$

express the effective thermal conductivities  $k_{eff}(n)$  and the thicknesses  $t_{eff}(n)$  in terms of layer-number-dependent ( $n$ ) in-plane ( $k_i(n)$ ) and cross-plane ( $k_c(n)$ ) thermal conductivities.

Fig. 4.9 provides an overview of the layer-number-dependent trend in effective thermal conductivity and thickness for different combinations of ( $k_i(n)$ ) and ( $k_c(n)$ ). For ( $k_i(n)$ ) and ( $k_c(n)$ ) we used values previously reported in literature [87, 90, 92, 93]. The calculated effective thermal conductivities

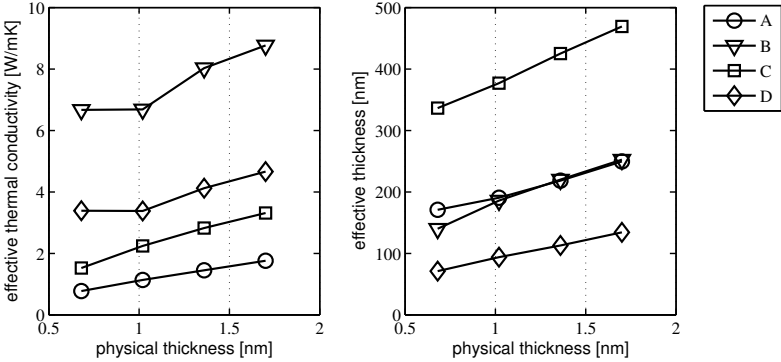


**Figure 3.6: Effective (isotropic) thermal conductivities and thicknesses vs. the physical graphene layer thickness**

for different in-plane and cross-plane conductivity combinations. The effective thickness includes the effective thickness of the SiO<sub>2</sub>/graphene interface. (A=[87, 93], B=[90, 92], C=[90, 93], D=[87, 92])

of the isotropic equivalent layers range from  $\sim 1$ -10 W/(mK) and are orders of magnitude smaller than the high in-plane thermal conductivities of the graphene layers. In contrast, the effective thickness of the isotropic equivalent layer is orders of magnitude larger than the physical thickness of the

graphene's of just a few atoms.

In all cases investigated, we observe an increasing trend of effective thermal conductivity with increasing  $n$ , and values larger than those of the underlying substrate, which is consistent with the picture of a higher conductive layer on top of a lower conductive substrate. Next, we extend an analytical approximate solution derived by Dryden [101], describing the spreading of heat from a circular heat source into an isotropic structure consisting of a high conductive layer on a low conductive substrate, to our experimental configuration. As the effective film thicknesses are significantly larger than the contact radius of our heat source we use the analytical thick-film approximation derived by Dryden to calculate thermal spreading resistances in comparison to our experimental data. Use of the thick-film approximation may not be intuitive considering the small physical thickness of the graphene films but is a direct consequence of the extreme anisotropy of the graphene layer. For effectively thick layers ( $2 < t_{eff}/a < \infty$ ), Dryden [101] derived an analytical expression for the thermal spreading resistance within 1% error of the full numerical solution as

$$R_{spr}(n) = \frac{1}{4ak_{eff}(n)} \left( 1 - \frac{2a}{\pi t_{eff}(n)} \log \left[ \frac{2}{1 + \frac{k_{eff}(n)}{k_{SiO_2}}} \right] \right), \quad (3.4)$$

where the first term is due to the constriction resistance within the layer and the second term is a correction for the relative layer thickness and conductivity ratio between the graphene film and the SiO<sub>2</sub> substrate. Following this approach, we calculate tip-sample thermal resistances  $R_{ts}$  using the unknown ( $R_{tip}$ ) as fit parameter, a constant tip-graphene thermal interface resistance of ( $R_{int}=2 \times 10^7$  K/W) and spreading thermal resistances calculated according to Eq. 3.4 for different combination of ( $\kappa_i$ ) and ( $\kappa_c$ ) illustrated in Fig. 3.1 (see exact values used in the following text). Although there is a significant temperature drop across the heat-spreading volume beneath our heated contact we neglect any temperature dependence of ( $\kappa_i$ ) and ( $\kappa_c$ ) in our analysis, as the effect is small compared to the systematic error in our measurement and model.

Fig. 3.7(a) shows the mean thermal resistances and corresponding standard deviations of the thermal resistance measurements in Fig. 3.3(a) as function of the physical graphene thickness. The thermal resistance decreases nearly linearly with increasing number of graphene layers. Note that the linear fit is a guide to the eye and a saturation of thermal resistance is expected for thicker graphene layers finally approaching the thermal spreading resistance of graphite. In comparison to our experimental results, we plotted thermal resistances as calculated by our analytical model starting from layer number

two. For a single layer of graphene, the model cannot be applied as  $\kappa_c$  of a single atomic layer is not defined. The comparison demonstrates, a qualitative agreement between the model and our experimental results, indicating that the resistance decreases indeed because of  $\kappa_{eff} > \kappa_{SiO_2}$  with increasing layer thickness. Considering additionally the increasing trends for  $\kappa_i(n)$  and  $\kappa_c(n)$  with increasing ( $n$ ), a thermal resistance reduction with thickness is expected by both the geometrical scaling of the layer as well as by the effective thermal conductivity increase.

The tip-sample thermal resistances calculated with  $\kappa_c(n)$  from Debye approximation (0.003-0.013 W/(mK)) [93] tend to overestimate the thickness dependence, in combination with  $\kappa_i(n)$  reported for both encased (186-240 W/(mK)) [87] and supported (720-850 W/(mK)) [90] graphene flakes. In contrast, the  $\kappa_c(n)$  predicted based on molecular dynamic simulations (0.06-0.09 W/(mK)) [92] is leading to an underestimation compared to the experimental trend, but still with a slightly better fit. These discrepancies may

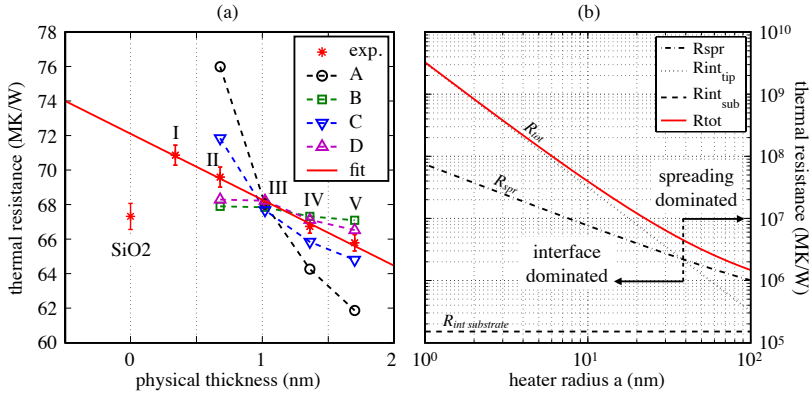


**Figure 3.7: Comparison between the experimental data and the model prediction**

(a) Thermal resistance vs. graphene thickness in comparison to our model prediction based on different in-plane and cross-plane conductivities reported in literature, with A=[87, 93], B=[90, 92], C=[90, 93] and D=[87, 92] (b) Thermal resistance as function of the heat source radius for the case of three graphene layers with  $\kappa_{eff}=3.38$  W/(mK) and  $t_{eff}=93.9$  nm, disentangled for the different resistances involved.

be due to the fact that reported thermal conductivities do not reflect the actual values in our nanoscopic contact where graphene is exposed to strong size and scattering effects. It is not clear which of those previously reported thermal conductivities are best suited to describe the thermal conductivi-

ties in our measurement configuration as so far no experimental or theoretical values have been reported for a nanoscopic hot tip in contact with a graphene/SiO<sub>2</sub> structure.

The validity of our analysis is further supported by the fact that the resulting fitting parameters  $R_{tip}$  for each of the combinations of  $k_i$  and  $k_c$  are 5.9, 6.5, 5.0 and  $6.2 \times 10^7$  (K/W), are consistently in the range of what is expected from previous studies using resistively heated silicon scanning probes comparable to those in our experiment [27].

The analysis indicates that even for nanoscopic hot spots heat dissipation can be consistently explained within a diffusive thermal spreading model, as long as the phonon mfp of the surrounding material is smaller than the heater size. As our model allows predicting heat dissipation from nanoscopic hot spots we may extrapolate to thermal resistances of hot spots different from those of the actual tip-sample contact size in our experiments. This may prove valuable for the design of atomically thin graphene heat spreaders. Fig. 4.10(b) shows the thermal resistance as function of the heater size radius for the case of three graphene layers with  $\kappa_{eff}=3.38$  W/(mK) and  $t_{eff}=93.9$  nm, divided into the individual contributions of the interface and the spreading resistances. One can immediately predict that for small contacts, in this example for heater size radii smaller  $\sim 40$  nm, the tip-graphene thermal interface resistance dominates the overall heat dissipation across the tip-sample contact.

To summarize this discussion, we may repeat the assumptions inherent to our simple analytical model: We assumed (i) diffusive transport within the graphene and the SiO<sub>2</sub> substrate, (ii) validity of the continuum-theory-based equation derived by Dryden even for atomically thin layers, (iii) the validity of the anisotropy equation derived by Myzychka even under these extreme anisotropies, (iv) isothermal temperature at the heat source, (v) approximation of the interface resistance between the graphene and SiO<sub>2</sub> as an additional increase of effective layer thickness, and (vi) negligible temperature dependence of the material properties for the temperature drop across the graphene.

While these assumptions can be made for the case of the SiO<sub>2</sub> substrate, leading to results in agreement with our experimentally observed trends, diffusive transport on this length scale is more questionable in the following studies on heat dissipation into graphene on a single-crystal silicon carbide (SiC) substrate. Therefore, we refrain from applying the model to the experimental results presented in the next section.

### 3.4 Thermal Identification of Graphene Flakes on Silicon Carbide

Complementary to previous studies on the graphene/SiO<sub>2</sub> structure, we investigated thermal transport into graphene on SiC. This is particularly interesting as it may provide further insights into a substrate dependence of heat dissipation into graphene. The single-crystalline SiC has a bulk thermal conductivity of  $\sim 370$  W/(mK), two orders of magnitude larger than that of amorphous SiO<sub>2</sub>. Considering the small effective thermal conductivity of graphene, as derived in the previous section, we are now probing a system consisting of a lower conductive layer on a higher conductive substrate.

The graphene/SiC sample investigated was fabricated by C. Dimitrakopoulos [103]. The sample has a complicated surface morphology with numerous steps and pits, making identification of graphene layers challenging. Identification of graphene was based on a combination of knowledge about the surface morphology, the surface graphitization process and the phase contrast between graphene regions and SiC as observed in tapping mode AFM. It is also known from preliminary experiments reported by Menges (Master thesis) that graphene can be thermally distinguished from the regions of carbon-enriched SiC using SThM. Here, we aim to demonstrate thermal identification of graphene layers of different thickness at high lateral thermal resolution.

The SiC surface is beneficial for our goal to achieve high spatial resolution, as it provides higher tip-wear stability than the rough SiO<sub>2</sub> substrate. Additionally, we used a sharper tip, with an initial tip apex radius of  $r \sim (4 \pm 1)$  nm, as determined from a SEM micrograph. The related tip-sample contact size is now smaller and the thermal conductivity of the substrate is higher than in previous experiments on SiO<sub>2</sub>, hence we expect to investigate thermal transport in a quasi-ballistic regime. While the small size of the contact is beneficial for achieving high spatial resolution, it poses an additional challenge for our measurements, as the tip-sample heat flux is less than that in the experiments on SiO<sub>2</sub>.

Despite the different substrates and the corresponding two orders of magnitude difference in mfp, we observe a similar thickness-dependent modulation in tip-sample thermal resistance as observed on SiO<sub>2</sub>. Fig. 4.8(a),(b) show the topography and the corresponding thermal resistance image of a SiC wafer partially covered by single and bilayer graphene. The surface topography was measured by the heated scanning probe at ambient pressure. Under these conditions the surface morphology of the SiC crystal surface is resolved using the strong distance dependence of gas mediated thermal conduction between the heated scanning probe and the sample. The can-

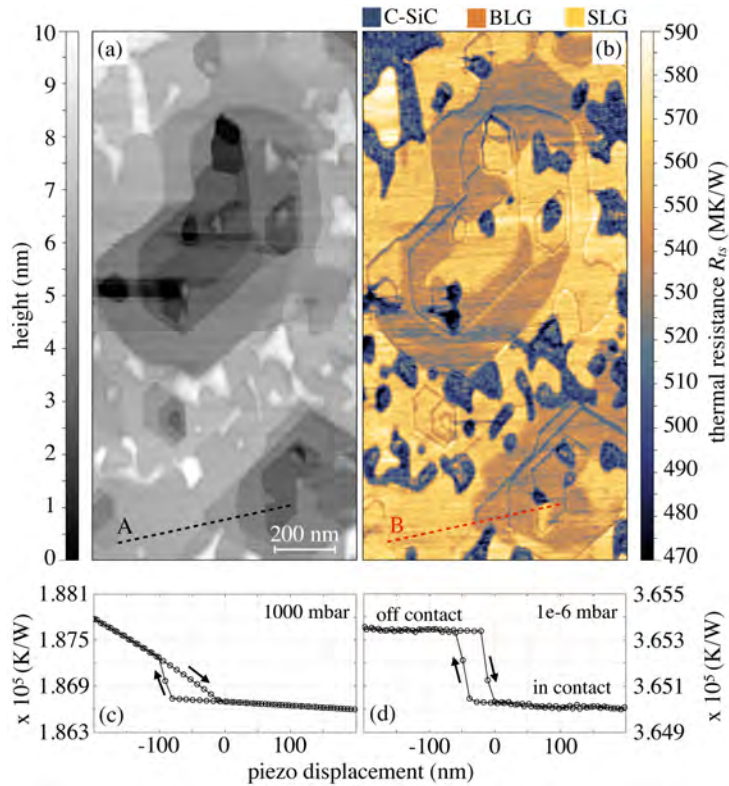


**Figure 3.8: Thermal resistance measurements on the graphene/SiC structure** (a) Topography image of the graphitized SiC surface in correlation to (b) the thermal resistance image of the same region with the SiC buffer layer (C-SiC), bi-layer graphene (BLG) and single layer graphene (SLG), (c) tip-sample approach curve under ambient pressure and (d) high-vacuum conditions illustrating the different character of the signal acquired by the scanning probe as function gas pressure.

tilever raw signal was scaled to height variations using the derivative of the cantilever voltage drop versus the piezo-displacement directly before contact as scaling factor. The optical beam deflection detection, described in chapter 2.2 was not yet implemented during these experiments.

In contrast, Fig. 4.8(b) shows the same sample region studied in vacuum clearly revealing modulations of the tip-sample thermal resistance in correlation with the graphene coverage. The overall thermal resistances are significantly higher than those measured on the SiO<sub>2</sub> structure, which can mainly be attributed to the decrease in tip-sample contact area (sharper tip). Again, thermal resistance increases when moving from the substrate (dark region) to a graphene region, followed by a decrease from  $5.6 \times 10^8$  K/W on the single layer to  $5.4 \times 10^8$  K/W on the bilayer graphene.

This trend may be surprising, considering the high bulk thermal conductivity of the single-crystalline SiC substrate in comparison to the estimated effective thermal conductivities of graphene. By considering a structure consisting of a lower conductive layer on top of a higher conductive substrate and a diffusive transport picture, one expects an increasing thermal resistance with increasing layer thickness. This clearly contradicts our experimental observation and is attributed to a transition from diffusive to ballistically dominated transport between the experiments on amorphous SiO<sub>2</sub> and those on crystalline SiC. As the mfp of the underlying SiC is well above the size of the heated contact, transport becomes strongly interface dominated and the simple analytical heat spreading model introduced in the previous section cannot be applied. Consistently, we find a decrease in thermal resistance from single to bilayer graphene of  $2 \times 10^7$  K/W. More importantly, our scanning thermal microscope achieves sufficient sensitivity to identify graphene layers of different thicknesses despite the significantly smaller thermal contact and high thermal conductivity of the underlying substrate. With respect to the performance of our scanning thermal microscope, we will next discuss the lateral resolution of our measurements as this is a unique feature of our experiments.

### 3.5 Lateral Thermal Resolution and Topography Artifacts

The combination of high lateral thermal resolution and sensitivity in experiments on SiC can be attributed to the efforts reported in chapter 2. The partially graphitized SiC sample is well suited to test the spatial thermal resolution of a SThM system as material contrast can be observed with nearly zero topography variation.

Fig. 4.11 shows the cross-sectional profiles of the topography and thermal



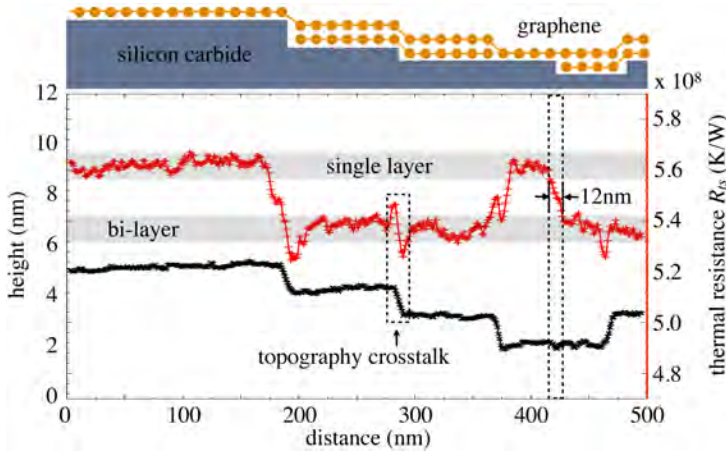


**Figure 3.9: Topography and thermal resistance profiles,** obtained from the regions depicted as A and B in Fig. 4.8, in correlation to a cross-sectional schematic of the sample, indicating the variation of graphene layer thickness at zero-height variation.

resistance of the regions depicted in Fig. 4.8. From the thermal resistance profile (red line) one can clearly distinguish the two signal levels corresponding to single and bilayer graphene, respectively. In the corresponding topography profile (black line), we observe multiple height levels, which are hardly correlated with the measured thermal transport as long as the surface coverage does not change. This is true in particular for the thermal resistance variation observed at  $\sim 425$  nm from the line-scan origin in Fig. 4.11 where we observe a material contrast at apparent constant topography. We suggest to use the material contrast at apparent zero-height variation to extract the thermal lateral resolution from the region depicted. Here, we observe a variation of  $2 \times 10^7$  K/W in thermal resistance within a lateral distance of 12 nm. Taking the full-width half maximum as resolution criterion, we find a thermal lateral resolution of 6 nm, slightly larger than the apparent topographic lateral resolution indicating a spreading of heat in the periphery of the contact. We like to highlight here that the definition of lateral thermal resolution in the presence of tip-sample contact area variations may lead to an overestimation of the actual thermal resolution [19].

The consequences of such a crosstalk between the topography and the thermal resistance signal can even be observed at the  $\sim 1$  nm height steps in the profiles of Fig. 4.11. As the tip is moving from the higher level towards the edge the thermal resistance increases as the contact between the tip and

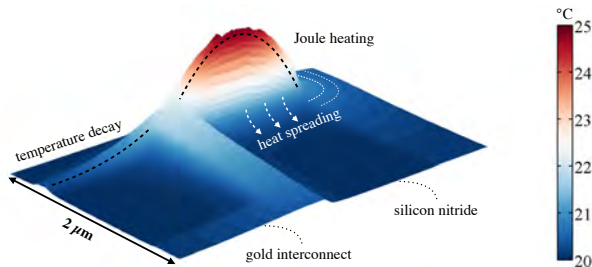
the sample shrinks. A maximum is reached when the tip-sample contact is minimized at the very edge of the step. When the tip contacts the lower level and the side of the step simultaneously, the thermal resistance is minimized. These topographic artifacts have to be carefully distinguished from true variations in the thermal properties of the sample that are not related to the geometrical change in tip-sample contact area.

### 3.6 Conclusions

In summary, we quantified the thickness-dependent modulation of thermal transport across graphene with 6 nm lateral thermal resolution on SiC and demonstrated sensitivity for the individual atomic layers. Thermal interface resistances were observed to dominate heat transfer across single-layer graphene within the hot nanoscopic contact on both low and high conductive substrates. The thermal resistance was found to decrease with increasing number of graphene layers on SiO<sub>2</sub>. This trend was attributed to thickness-dependent spreading of heat within the graphene sheets, in relation to previously reported thermal conductivities. Both the experimental observations and the presented analytical model may prove useful for the performance estimation of future graphene devices. Single-layer graphene sheets appear hardly suited to promote heat removal, whereas multilayer graphene, chosen in respect to the size of the adjacent hot spot may find applications for thermal management in nanoelectronics. In particular, the large thermal anisotropy of the layer appears promising, as it relates to an effective thickness much larger than the actual physical thickness, and consequently to beneficial form factors. We also highlighted the effect of topography artifacts on thermal scanning probe measurements, which are relevant even down to the sub-nm scale and can diminish the reliability of scanning thermal microscope measurements. The precise quantification of thermal transport between the scanning probe and the sample as demonstrated in this chapter, is a prerequisite for the development of further thermal scanning probe methods like the scanning probe thermometry presented in the next chapter. All major results of this chapter have been published in *Physical Review Letters* [55] and highlighted as Editors suggestion.

# 4

## Quantification of Nanoscopic Temperature Fields and Hot Spots



In this chapter, we describe a novel method for the quantification of nanoscopic temperature fields using a scanning probe microscope. By accounting for the local dependence of the tip-sample thermal resistance, we demonstrate imaging of nanoscopic temperature fields despite the presence of topography and material related heat-flux variations. The proposed method overcomes a major drawback of scanning thermal microscopy, namely, the strong dependence of heat-flux-related signals on the position-dependent tip-sample contact geometry, which gives rise to significant measurement artifacts. We apply the method to visualize self-heating of metal interconnects with 30 mK sample temperature resolution and report the observation of nanoscopic hot spots near lithographically defined defects.

## 4.1 Why Moore got a Fever

In the preceding two chapters, we described the development of a vacuum scanning thermal microscope and demonstrated its high performance [55]. Here, we will introduce a novel thermal scanning probe method to quantify self-heating of metal interconnects. As motivation to these studies, we provide a short introduction to the self-heating of integrated circuits (ICs) [65]. Computers get hot as we use them, not only because of fundamental thermodynamic reasons but also because the underlying CMOS technology is approaching its limit as a powerful, yet energy inefficient approach to information processing [65, 104]. As a consequence, the clocking frequency of most computers is limited to around 3-4 GHz to reduce the heat dissipated to an amount that can be removed by air or water cooling. While the need for cooling is a costly constraint [105], a speed limit is the end of any performance increase as the computational work delivered per watt scales with the clocking frequency [65]. We may actually compare this situation to the human body getting less productive as it is forced to limit its activities because of a fever. Hence, throttling of ICs is nothing more than the treatment of a symptom, while the underlying shortcomings of hardware technology remain unaddressed.

CMOS hardware is typically not considered as maldevelopment, as it has been the driver of technological and social revolutions in the past century. The ongoing scaling of CMOS to nanoscopic ICs, already forecasted by Gordon Moore in 1965 [106] is touted as success, ranked among the biggest technological achievements of mankind. It is just the self-heating, which is considered an issue that has to be managed, limiting performance and reliability [107]. However, as the cost-motivated scaling of CMOS technology is finally facing its performance limit, a rethinking can be observed.

The energy efficiency of computation, not the hardware cost, become the limiting factor for big-data processing systems [105]. The management of heat dissipation, i.e., the treatment of symptoms by technology such as cooling fans and copper heat sinks is no longer sufficient to face the exponential growth of data. Within the next 10 years, the power use of electronics for information processing is predicted to reach one third of the total energy consumption [65].

Most promising approaches addressing this trend seem to follow two major strategies. One strategy is, to develop low-power-consuming electronics based on the integration of new materials, devices and architectures. The second, probably more promising strategy in the long term, is to explore the fundamental thermal character of information processing [68] with the aim of developing energy-efficient, thermodynamically reversible computing principles.

A scanning thermal microscope, as developed in this work may be used to identify the underlying thermal mechanisms in nanosystems for information processing, with the goal of applying these findings for innovating and inventing technology in balance with thermal energy transfer and conversion processes. It is certainly of interest to explore how thermal effects can be used advantageously to manipulate and process information rather than treating the heat simply as a waste product.

The investigation of CMOS structures is a promising starting point as the technology is thermally limited [108]. All major device failure mechanisms observed in CMOS electronics, like electromigration, dielectric breakdown, thermal fatigue, are strongly temperature dependent. Essentially all important material and device properties, like the band gap of the semiconductors, the mobility of the charge carriers, or the device leakage current, exhibit a significant temperature dependence that strongly affects device performance [65]. Currently, average CPU temperatures of about 80-100 °C are considered as acceptable values, however, local hot spots on the order of tens of nanometers in size, forming in particular in the drain regions of transistors are predicted to have significantly higher temperatures [109].

These hot spots limit the performance of today's computers as they dictate the maximum clocking frequency beyond which device failures are observed at unacceptably high rate. It is therefore crucial to know both the magnitude and the spatial distribution of temperature fields on the scale of individual transistors and interconnects to understand the underlying physical processes. This is an enormous challenge as experimental techniques to spatially resolve temperature fields on nanoscopic length scales are not well established [1, 2]. Typically applied optical methods for temperature mapping of ICs, such as thermoreflectance microscopy [110], do not achieve the spatial resolution needed to study the formation of nanoscopic hot spots. Consequently, the development of near-field methods based on local scanning probes, capable of spatially resolving temperature fields down to the scale of few to hundreds of nanometers [18, 25, 27–29, 38], is substantial for the investigation of thermal processes in nanosystems. Here, we address this challenge by developing a novel method for scanning probe thermometry.

## 4.2 Nanoscale Thermometry by the Heat Flux Reference Method

In this section we derive a novel method to quantify local temperature fields by scanning probe thermometry, one of the most important methodological inventions of this thesis work. In contrast to previous attempts inferring the sample temperature from the measurement of a single-heat-flux-related

scanning probe signal [15, 18, 25, 28, 29], we demonstrate that simultaneous acquisition of a second, tip-sample thermal-resistance-related reference heat flux signal is necessary to minimize topography-related artifacts, frequently observed in studies reporting the quantification of nanoscopic temperature fields. Experimental demonstrations illustrating the principle follow in the next sections. For an introduction to the fundamentals of scanning probe thermometry, we refer to chapter 1.2.

The novel approach preserves the main idea of the double-scan technique (see chapter 1.2) that two signals are needed to quantify nanoscopic temperature fields [27]. The sample temperature ( $T_s$ ) can be derived from two measurements as

$$T_{s,2} = T_{h,2} - (T_{h,0} - T_{s,0}) \times \frac{Q_{hs,2}}{Q_{hs,0}}, \quad (4.1)$$

where  $T_h$  denotes the temperature of the scanning probe heater,  $T_s$  the sample temperature,  $Q_{hs}$  the heater-sample heat flux and the indices  $n$  relate to the initial scan ( $n = 0$ ) and the second scan ( $n = 2$ ) (see chapter 1.2 for a detailed introduction).

In the following we will illustrate how Eq. 4.1 can be used advantageously to calculate the sample temperature from two measurement signals acquired in a single scan. We can apply exactly the same equation (Eq. 4.1) derived for the double-scan-method (see chapter 1.3.2) to our newly proposed single-scan approach, with the difference that the indices  $n$  in Eq. 4.1 now relate to simultaneously acquired measurement signals (DC ( $n = 0$ ) and AC ( $n = 2$ )) instead of two different scans. Accordingly, one could consider the technique as an extension of the double-scan method.

In contrast to our previous approach, where the sample temperature is switched on and off between two scans, the sample temperature now will change many times during acquisition of each individual image pixel. Such a temporal temperature variation can be achieved, for example by optical laser pulse heating or modulation of a sample cooling channel.

As we are in particular interested in quantifying self-heating of nanoscale electronic devices, we can conveniently create the necessary temperature modulation by applying an AC voltage bias of frequency ( $\omega$ ) to the device. Considering pure Joule heating in the device in response to the AC voltage excitation, the device temperature is modulated as

$$T_s = T_{s,0} + T_{s,2} \sin(2\omega t) \quad (4.2)$$

comprising both a time-independent DC ( $n = 0$ ) and a time-dependent AC ( $n = 2$ ) component modulated at twice the excitation frequency ( $\omega$ ), as the electrical power ( $P = V^2/R$ ) dissipated in the device scales with the

square of the applied voltage.

As the sample temperature is modulated by Joule heating, both the heat flux ( $Q_{hs}$ ) and the temperature difference ( $T_{hs}$ ) between heater and sample are modulated if the tip is in contact with the device.

In contrast to the double-scan method, where the initial measurement was conducted for a known sample temperature ( $T_{s,0} = T_{s,ambient} = 20^\circ\text{C}$ ), both the steady-state DC temperature ( $T_{s,0}$ ) and the time-dependent AC temperature increase ( $T_{s,2}$ ) are unknown. However, the steady-state DC temperature of the sample ( $T_{s,0}$ ) and the magnitude of the AC temperature increase ( $T_{s,2}$ ) are related, and can be estimated [111] for an applied excitation frequency ( $\omega$ ) as

$$T_{s,0} = \sqrt{1 + (2\omega\tau)^2} \times T_{s,2} + T_{s,ambient} \quad (4.3)$$

with  $\tau$  being the thermal time constant of the device. The thermal time-constant  $\tau$  is unknown and can be experimentally derived by frequency-dependent measurements of the temperature field or estimated by simulations. However, if the excitation frequency ( $\omega$ ) is chosen small enough with respect to  $\tau$ , so that the device is always in steady-state, meaning that the device temperature is independent of the excitation frequency, we can approximate  $T_{s,0} \approx T_{s,2} + T_{s,ambient}$ . By substituting  $T_{s,0}$  into Eq. 4.1, we calculate the magnitude of the AC peak temperature increase as

$$T_{s,2} = \frac{T_{h,2}Q_{hs,0} - (T_{h,0} - T_{ambient})Q_{hs,2}}{Q_{hs,0} - Q_{hs,2}} \quad (4.4)$$

which equals, according to the assumption of steady-state, the DC temperature increase above ambient temperature. If steady-state is not fully achieved Eq. 4.4 leads to an underestimation of the DC temperature increase.

From Eq. 4.4 it follows that the sample temperature field in response to Joule heating is determined by the AC and DC components of the heater-sample heat flux ( $Q_{hs}$ ) and the heater temperature ( $T_h$ ). In our experiments, we do not directly measure these quantities, but infer them from the electrical voltage response of the cantilever sensor ( $V_{Lev}$ ), which is modulated temporally as

$$V_{Lev,n} = V_{Lev,0} + V_{Lev,2} \sin(2\omega t) \quad (4.5)$$

by the tip-sample heat flux, which affects the electrical resistance of the heater. The two different temporal components of this voltage bias can be measured by the DC and AC circuitry illustrated in chapter 2.3, which comprises a differential amplifier to sensitively measure the DC component

( $V_{Lev,0}$ ) and a lock-in amplifier to sense the AC component ( $V_{Lev,2}$ ).

Relating these voltage signals to the temperature of the heater ( $T_h$ ) requires prior calibration of the scanning probe, as discussed in chapter 2.4, to establish the relation between the temperature and the electrical resistance of the heater. Based on the electrical fix-point calibration discussed in chapter 2.4, we can derive the heater temperature as function of  $V_{Lev,n}$  as

$$T_h(V_{Lev}) \approx T_h(V_{Lev,0}) + T_h(V_{Lev,2}) \sin(2\omega t) \quad \text{with} \quad (4.6)$$

$$T_h(V_{Lev,2}) \approx \left. \frac{\partial T_h}{\partial R} \right|_{R_0} \times \left. \frac{\partial R}{\partial V_{Lev}} \right|_{V_{Lev,0}} \times V_{Lev,2}, \quad (4.7)$$

where higher-order terms can be neglected (see subsequent discussion).

Note that here we use a linearization although the temperature is a nonlinear function of the electrical resistance as shown in the cantilever calibration measurements in chapter 2.4. The validity of such a linearization process requires that changes in the heater temperature in response to tip-sample heat flux variations be small compared with the absolute temperature of the heater. This is the case in our measurements as the thermal resistance of the cantilever is typically three orders of magnitudes smaller than the thermal resistance of the tip-sample contact [55].

Apart from the heater temperature, also the heat flux  $Q_{hs}$  between the scanning probe sensor and the sample needs to be related to the electrical measurement signals. We assume that all electrical power dissipated in the cantilever is dissipated as heat in the cantilever sensor, as discussed in chapter 2.4, which means that the total electrical power dissipated ( $P_{el}$ ) equals the total heat flux ( $Q_{Tot}$ ). Energy conservation requires that the total heat flux equals the sum of the heat flux into the cantilever ( $Q_{Lev}$ ) and the heat flux across the sample contact ( $Q_{hs}$ ), which is defined as

$$Q_{hs} = Q_{Tot} - Q_{Lev} = P_{el} - Q_{Lev}. \quad (4.8)$$

The total heat flux, i.e., the electrical power ( $P_{el}$ ) dissipated in the cantilever, can be directly expressed as a function of the cantilever voltage ( $V_{Lev}$ ) as

$$P_{el} = \frac{1}{R_{series}} [V_{Tot}V_{Lev} - V_{Lev}^2], \quad (4.9)$$

with  $R_{series}$  being the 2 k $\Omega$  series resistor in our Wheatstone bridge measurement circuitry (see chapter 2.3). By inserting Eq. 4.5 into Eq. 4.9 and



separating  $P_{el}$  into its various temporal components

$$\begin{aligned}
 P_{el} &= P_{el,0} + P_{el,2} \sin(2\omega t) + P_{el,4} \sin(4\omega t) \quad \text{with} & (4.10) \\
 P_{el,0} &= \frac{1}{R_{series}} \left[ V_{Tot} V_{Lev,0} - V_{Lev,0}^2 - \frac{1}{2} V_{Lev,2}^2 \right] \\
 P_{el,2} &= \frac{1}{R_{series}} [V_{Tot} V_{Lev,2} - 2V_{Lev,0} V_{Lev,2}] \\
 P_{el,4} &= \frac{1}{R_{series}} [0.5V_{Lev,2}^2],
 \end{aligned}$$

we can derive the electrical power dissipated in the scanning probe in contact with the sample. Note that the higher-order term at  $(4\omega)$  is very small compared with the other terms, as  $V_{Tot} \gg V_{Lev,2}$ , and is not considered for further analysis. To finally derive  $Q_{hs}$ , we need to subtract the cantilever heat flux ( $Q_{Lev}$ ) from the total heat flux ( $Q_{Tot} = P_{cl}$ ).

The heat flux into only the cantilever ( $Q_{Lev}$ ) can be derived using the heater temperature ( $T_h(V_{Lev})$ ) of Eq. 4.7 as

$$\begin{aligned}
 Q_{Lev} &= Q_{Lev,0} + Q_{Lev,2} \sin(2\omega t) \quad \text{with} & (4.11) \\
 Q_{Lev,0} &= \frac{T_{h,0} - T_{ambient}}{R_{Lev}} \\
 Q_{Lev,2} &= \frac{T_{h,2}}{R_{Lev}}.
 \end{aligned}$$

Here, the thermal resistance of only the cantilever ( $R_{Lev}$ ) is needed and has to be derived prior the measurement scan from tip-sample approach curves as described in chapter 1.2.

By inserting Eq. 4.10 and Eq. 4.11 into Eq. 4.8, and Eq. 4.8 and Eq. 4.7 into Eq. 4.4, we can finally express,  $T_s$  as function of the measured DC ( $n = 0$ ) and AC ( $n = 2$ ) voltage components of  $V_{Lev}$  measured across the cantilever.

Note that for specific measurement arrangements, such as a constant heater temperature, Eq. 4.4 can be further simplified and expressed as

$$T_{s,2} = (T_{h,0} - T_{ambient}) \times \frac{P_{el,2}}{P_{el,0} + P_{el,2}}, \quad (4.12)$$

whereas the expression in Eq. 4.4 is a more general form that can also be applied for a constant input voltage bias applied the cantilever, as is the case in our experiments. For a constant applied electrical heating power, which is another common approach reported in scanning thermal microscopy experiments, the sample temperature can be directly inferred from the mea-

surement of the heater temperature DC and AC components as

$$T_{s,2} = (T_{h,0} - T_{ambient}) \times \frac{T_{h,2}}{T_{h,0} - T_{ambient} + T_{h,2}}. \quad (4.13)$$

In the following sections, we apply the novel method to quantify the self-heating of metal interconnect test structures, directly demonstrating the benefits of the proposed method.

### 4.3 Local Self-Heating of Nanoscale Metal Interconnects

The test sample consists of nanoscale gold interconnects on a silicon (111) substrate covered with 150 nm of amorphous silicon nitride ( $\text{SiN}_x$ ), illustrated in Fig. 4.1). The electrical contact pads are fabricated by photolithography and fit to the layout of our multi-pin probe-card. The narrow gold lines are fabricated via electron-beam lithography (Vistec EBPG5200) and patterned by a reverse lift-off process.

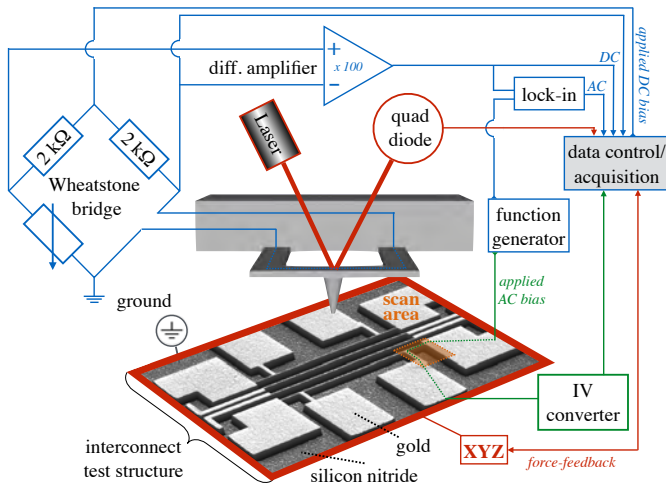


**Figure 4.1: Illustration of the experiment**

showing the thermal scanning probe in contact with a metal interconnect test structure. An AC voltage bias is applied to the gold interconnect segment indicated as scan area. The thermal signal of the scanning probe is acquired by the circuitry shown, which comprises a Wheatstone bridge, a differential amplifier, and a lock-in amplifier.

In a first study, a sinusoidal voltage ( $V_{pp}=3\text{ V}, f = \omega/(2\pi)=10\text{ kHz}$ ) is applied to the metal heater section depicted in Fig. 4.1 with a  $1\text{ k}\Omega$  resistor in series, giving rise to a steady-state DC temperature increase and a dynamic AC modulation of the sample temperature at twice the frequency of the applied voltage excitation. A constant DC voltage bias is applied to the scanning probe, creating a heat flux of few microWatt between the self-heated sensor element ( $\sim 383^\circ\text{C}$ ) and the sample. The large heat flux and sensor temperature are beneficial for optimization of the sensor thermal resolution as discussed in chapter 2.5.

The sensor signal of the scanning probe in contact with the sample gets modulated by the heat flux across the tip-sample contact and comprises a DC voltage component measured by the DC circuitry illustrated in Fig. 4.1 and a small AC component measured via the lock-in amplifier. As the electrical power dissipated inside the gold interconnect scales with the square of the applied voltage, the lock-in amplifier is tuned to the second harmonic of the modulation frequency ( $20\text{ kHz}$ ). The scan speed ( $3.3\text{ ms/pixel}$ ) is adjusted to ensure sufficient integration time ( $10\text{ ms}$ ) for the lock-in amplifier.

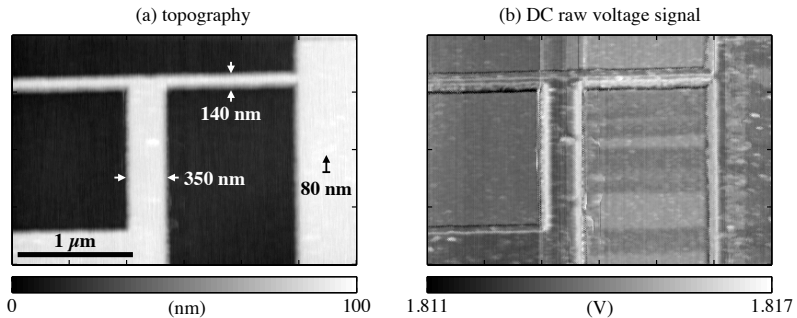


**Figure 4.2: Topography and DC voltage raw signals**

(a) Topography image of the interconnect segment and (b) raw signal of the DC voltage bias measured across the scanning probe.

Fig. 4.2 shows the sample topography and the DC raw voltage signals acquired simultaneously during one measurement scan. The topography image Fig. 4.2(a), was directly obtained from the z-axis voltage signal of the piezo-scanner sensor under force-feedback operation. The gold heater lines have a height of around  $80\text{ nm}$ . The thinner line has a measured width of  $\sim 140\text{ nm}$ . Simultaneously with the topography signal, we acquired the DC voltage bias across the cantilever sensor, as shown in Fig. 4.2(b). Signal variations are mainly observed in regions where the sample topography changes abruptly,

visible from a direct comparison with the topography image. In contrast, neither the two different materials (gold and  $\text{SiN}_x$ ) nor variations in relation to self-heating of the structure can be easily inferred from the DC voltage signal. This observation indicates that the DC signal is dominated by variations in the thermal resistance between the heater and the sample, which is mainly a function of the tip-sample contact geometry.

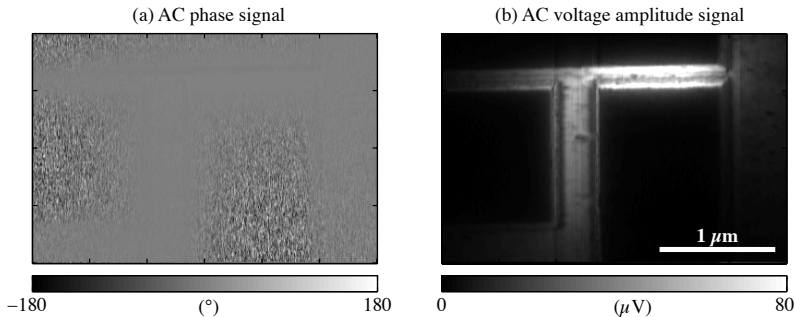


**Figure 4.3: AC voltage raw signal**  
scales as (a) phase and (b) voltage amplitude

Fig. 4.3 shows the simultaneously acquired AC signal scaled as the phase (a) and the voltage amplitude (b). We observe a constant phase signal of varying intensity along the self-heated interconnect and a strong voltage amplitude signal in the thinner segment of the interconnect. Additionally, signal variations are visible at the edges of the interconnect structure, which are apparently correlated to the sample topography changing the tip-sample contact geometry. These observations illustrate that the AC signal acquired by the scanning probe is sensitive to the heat flux between the sensor element and the sample, which is not only a function of the temperature difference between the scanning probe and the sample, but also of the thermal resistance. Previous reports that inferred the temperature by scanning thermal microscope [15, 28, 29] acquired AC signals similar to those shown in Fig. 4.3(b) and rescaled these signals to an apparent temperature map, weighting the measured heat-flux-dependent signal by a position-independent tip-sample thermal resistance approximated from literature and simulations. This procedure, as discussed in chapter 1.2, leads to significant topography artifacts, thereby hindering the quantification of temperature fields, as we will further discuss below.

Fig. 4.4(a) shows the apparent temperature field, calculated by rescaling the AC voltage signal by a position-independent average thermal resistance be-

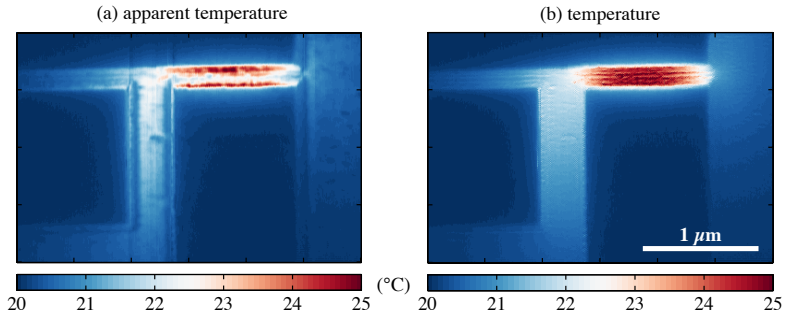


**Figure 4.4: Comparison between the apparent and the actual temperature field**

(a) Apparent temperature field calculated by rescaling of the AC voltage signal by a position-independent thermal resistance between the scanning probe sensor and the sample.

(b) Temperature field as calculated using the novel method, taking the position dependence of the thermal resistance into account.

tween the scanning probe sensor and the sample, illustrating these artifacts. Artifacts appear in particular in regions where the sample topography and consequently the tip-sample contact geometry change. For the thinnest segment of the interconnect, which is the region of greatest heat dissipation, the signal is strongly dominated by variation in thermal resistance, related to the tip-sample contact geometry as evident by comparison with the DC voltage raw signal. For this region, it is particularly difficult to quantify temperature fields using the AC signal only. The apparent temperature field erroneously indicates a very inhomogeneous temperature distribution along the interconnect, with nanoscopic features and a strong heating of the edges. Note that these features are topographic artifacts and cannot be considered for quantifying of the interconnect temperature.

To overcome this limitation, we suggest a novel scanning probe thermometry method based on the simultaneous acquisition of an AC and a DC reference heat flux signal between the scanning probe sensor and the sample as derived in the previous section. The direct visual comparison of the AC voltage amplitude and the DC voltage raw signal indicates that both signals are correlated by a thermal resistance dependence. Applying the proposed method we rescale the DC and AC voltage raw signals to variations of the heat flux ( $Q_{hs}$ ) and the temperature of the sensor element ( $T_h$ ) and calculate the sample temperature field ( $T_s$ ) according to Eq. 4.4.

Fig. 4.4(b) shows the calculated steady-state DC temperature increase ( $T_{s,0}$ ) in comparison with the apparent temperature field obtained by scaling the

signals by a position-independent thermal resistance between the scanning probe sensor and the sample. The direct comparison with Fig. 4.4(a) illustrates that the topography-related artifacts can be minimized by the proposed method. The experimental data shown in Fig. 4.4 is the direct verification of the method theoretically derived in the preceding section, and impressively demonstrates the benefits of the new approach compared with previous attempts that inferred temperatures by scanning probes [15, 18, 25, 28, 29]. The experimental demonstration of scanning probe thermometry in the presence of topography and material related heat flux variations is an important result of this work.

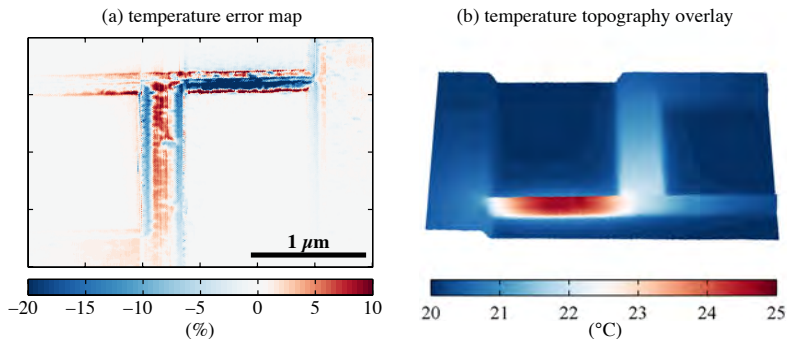


**Figure 4.5: Temperature error map and 3D temperature topography overlay**  
 (a) Temperature error map calculated as the difference between the apparent temperature and the actual temperature.  
 (b) Temperature-topography overlay clearly illustrating the absence of topography artifacts at the edges of the interconnect.

To clearly distinguish the difference between our approach and previous approaches that infer temperature fields by scanning thermal microscopy [15, 18, 25, 28, 29], we plotted a temperature error map, obtained by the difference between the apparent and the actual temperature field (see Fig. 4.4(a,b)) in 4.5(a). Deviations of up to 30 % are observed in regions where the tip-sample thermal resistance variations are largest. Our finding indicates that the temperature fields of nanoscopic objects can only be quantified by scanning thermal microscopy if local variations of thermal resistance due to the topography are taken into account. Considering our studies on thermal transport across graphene presented in the preceding chapter, topography related thermal resistance variations are significant even for sub-nanometer height variations. The interconnect structure studied here has a height of about 80 nm and still topographic artifacts are avoided. This is illustrated

in Fig. 4.5(b), which shows a temperature-topography overlay that proves the absence of edge-related artifacts. Note that the temperature field was low-pass-filtered (by a  $5 \times 5$  nearest-neighbor smoothing) to illustrate the spreading of heat into the contacts and the sample substrate more clearly. The unsmoothed temperature field, calculated directly from the raw voltage signal is shown in Fig. 4.4(b).

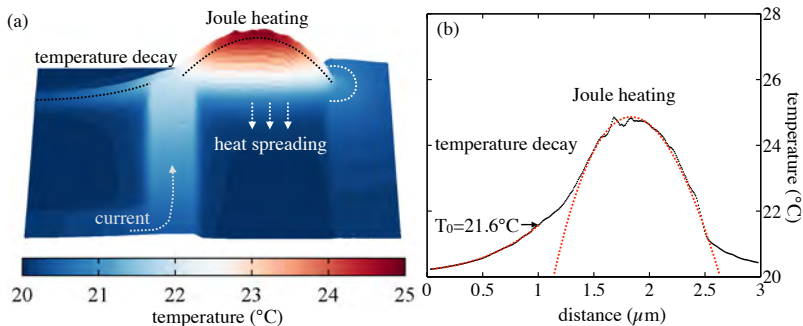


**Figure 4.6: Temperature field illustration**

(a) 3D plot of the temperature field presented as height variation, visualizing Joule heating of the thin wire segment, heat spreading into the substrate and the temperature decay into the unbiased floating interconnect segment.

(b) Temperature profile extracted along the center of thin interconnect segment. The dotted parabola indicating Joule heating of the interconnect segment is a guide to the eye.

In Fig. 4.6(a) we illustrate the self-heating of the interconnect structure as a 3D temperature field. This 3D representation allows us to visualize a parabolic temperature profile (see guide to the eye in Fig. 4.6(b)) along the thin interconnect element. Such a profile is expected for Joule heating of a metallic interconnect segment. The detailed shape of the temperature distribution in Fig. 4.6 is a function of the electrical power dissipated, the thermal conductivity of the gold interconnect, the thermal conductivity of the underlying  $\text{SiN}_x/\text{Si}$  substrate, and the thermal conductance of the interface between the interconnect and the substrate. The local quantification of the temperature field as accomplished in this thesis can be used to extract these thermal properties of the sample structure by fitting an appropriate model to the temperature distribution measured. Determination of the conductance of the interface between the substrate and the interconnect is of particular interest as this property cannot be easily estimated from literature values. Here, we will make an estimate of the thermal interface between the gold interconnect and the substrate based on the exponential temperature decay

observed in the unbiased floating segment of the interconnect in the upper left side of the interconnect structure.

To estimate the thermal interface conductance, the heat diffusion equation [27] has to be solved. We impose the measured temperature  $T_0 = 21.6^\circ\text{C}$  at the origin of the unbiased interconnect segment as a boundary condition. The 1D heat diffusion equation reads

$$A\kappa \frac{\partial^2 T}{\partial x^2} - g(T - T_0) = 0. \quad (4.14)$$

Here,  $A$  denotes the cross-sectional area of the interconnect segment,  $\kappa$  is the thermal conductivity of the gold interconnect,  $g$  the thermal conductance between the interconnect and the substrate per unit length,  $T$  the temperature, and  $x$  the position along the interconnect. For a boundary condition of  $T = T_0$  at  $x = 0$ , we find the following solution:

$$T(x) = T_0 \exp\left(-\sqrt{\frac{g}{A\kappa}}x\right) \quad (4.15)$$

The cross-sectional area of the interconnect is calculated from the measured topography of the interconnect as  $1 \times 10^{-14} \text{ m}^2$  and the thermal conductivity of thin gold films has been reported as  $100 \text{ W}/(\text{mK})$  [112]. Fitting Eq. 4.15 to the measured temperature profile as indicated in Fig. 4.6(b) with  $g$  as fit parameter, we extract a thermal interface conductance per unit length of  $4.6 \text{ W}/(\text{mK})$ . This corresponds to a thermal interface conductivity of  $4.6 \times 10^7 \text{ W}(\text{m}^2\text{K})$ , which is in the range of values expected for metal dielectric interfaces. Attempts comparing the quantified temperature field with more sophisticated models are currently in preparation.

It is also interesting to note that the visualization of the temperature field indirectly allows one to resolve the electrical current path in the sample by the related heat dissipation. Fig. 4.6(a) indicates the electrical current path between the left electrode and the bottom electrode. While the ability to map the current path by the related dissipation of heat may not be of high relevance for the presented self-heating experiment of an interconnect structure, it is of potentially high interest for studying percolative systems, such as phase-change memory cells, where the electrical current path is not a priori defined by the device structure.

At the same time the observation of heat spreading into the substrate is of interest. We can visualize the heat spreading over a distance of more than one micrometer away from the interconnect, which is indicative of a sample temperature resolution down to tens of mK. We will provide a more detailed analysis of the temperature resolution in the last section of this chapter.

To prove that the signal acquired by the scanning probe sensor is indeed



the temperature increase of the sample in response to pure Joule heating, we studied the interconnect temperature as function of the applied voltage excitation. The AC voltage excitation amplitude applied to the interconnect was continuously increased from 0 to 0.4 V, while the tip was scanned on a fixed position across the self-heating interconnect. Note that the interconnect studied corresponds to a different sample than the one shown in the previous experiments of this section. The excitation frequency (10 kHz) applied to the interconnect and the DC voltage bias applied to the scanning probe were kept constant.

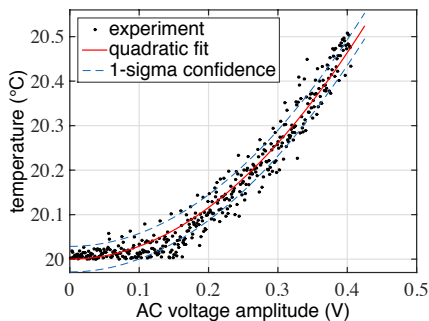


**Figure 4.7: Interconnect temperature as function of the voltage bias applied**  
 (a) Temperature of the interconnect as function of the applied AC voltage bias amplitude. The temperature is observed to increase quadratically with the bias, indicative of Joule heating of the interconnect.

Fig. 4.7 shows the measured DC sample temperature as a function of the applied voltage bias amplitude. We observe an increasing interconnect temperature with increasing voltage. Fitting of the temperature dependence reveals a quadratic increase of the DC sample temperature with increasing excitation voltage amplitude. This finding supports our assumption that we observe pure Joule heating in the second harmonic AC signal of the scanning probe sensor. The bias-dependent temperature evolution also indicates a noise-limited sample temperature resolution on the order of  $\sim 30$  mK in the 100 Hz bandwidth as indicated by the intersection of the 1- $\sigma$  confidence bound of the quadratic fit with the  $y$ -axis. Note that the sample temperature resolution could be further increased by narrowing the bandwidth of the measurement.

From the known electrical current applied to the interconnect, we can estimate the temperature increase of the interconnect as consistency check to the temperature determined by the scanning probe. On average, we applied an electrical current of  $485 \mu\text{A}$  to the  $10\text{-}\mu\text{m}$ -long interconnect. The

resistance of the interconnect alone is unknown but we can estimate the electrical resistance of the gold interconnect from the measured cross-sectional area of the interconnect inferred from the scanning probe topography signal ( $5.5 \times 10^{-15} \text{ m}^2$ ) and the electrical resistivity of gold ( $2.44 \times 10^{-8} \Omega\text{m}$ ) as  $44 \Omega$ . This corresponds to dissipated electrical power of  $10 \mu\text{W}$ .

In order to estimate the temperature increase of the interconnect, we divide the electrical power dissipated per unit length by the thermal conductance per unit length ( $g = 4.6$ ) as determined from the heat spreading into the unbiased segment of the interconnect in Fig. 4.6. Accordingly, we estimated a temperature increase of the interconnect of  $\Delta T = 10 \mu\text{W} / 10 \mu\text{m} \times 4.6 \text{ W}/(\text{mK}) = 0.46 \text{ K}$ . The estimated temperature is on the order of the experimentally observed temperature increase measured by the scanning probe. A more in-depth analysis would require the experimental characterization of the interconnect by an electrical four-point measurement scheme, which will be implemented in future experiments.

## 4.4 Observation of Nanoscale Hot Spots

In the following, we report on the self-heating of a 300-nm-wide gold interconnect structure with nanoscopic constrictions, acting as lithographically defined defects of enhanced heat dissipation. Each constriction consists of two parallel nanobridges with a nominal width of 40 nm and a length of 100 nm. The spacing between the nanobridges in each gap decreases from left to right as illustrated in the SEM micrograph of Fig. 4.8(a). The length of the interconnect exceeds our maximal scan range of  $10 \mu\text{m}$ , and we investigated self-heating of individual segments, indicated in Fig. 4.8(a).

In the first scan, we simultaneously mapped self-heating around two constrictions as shown in Fig. 4.8(b). The temperature map in Fig. 4.8(b) is calculated from the DC and AC voltage signals acquired as explained in the previous sections. We can directly image enhanced Joule heating around the nanoscopic constrictions, acting as hot spots within the 300-nm-wide interconnect.

Together with the temperature profile extracted along the center of the interconnect, we can observe an asymmetric temperature distribution around the first constriction as indicated by the red arrow in the temperature profile. This asymmetry is likely related to the additional cooling affect of the nearby electrode pad on the left side. In contrast, the temperature distribution around the second constriction is more symmetric, indicating that the spreading of heat into the substrate is the dominant path of heat dissipation. To gain further insights into self-heating in the vicinity of the constriction, we studied the second region depicted in Fig. 4.8(a) in more detail.

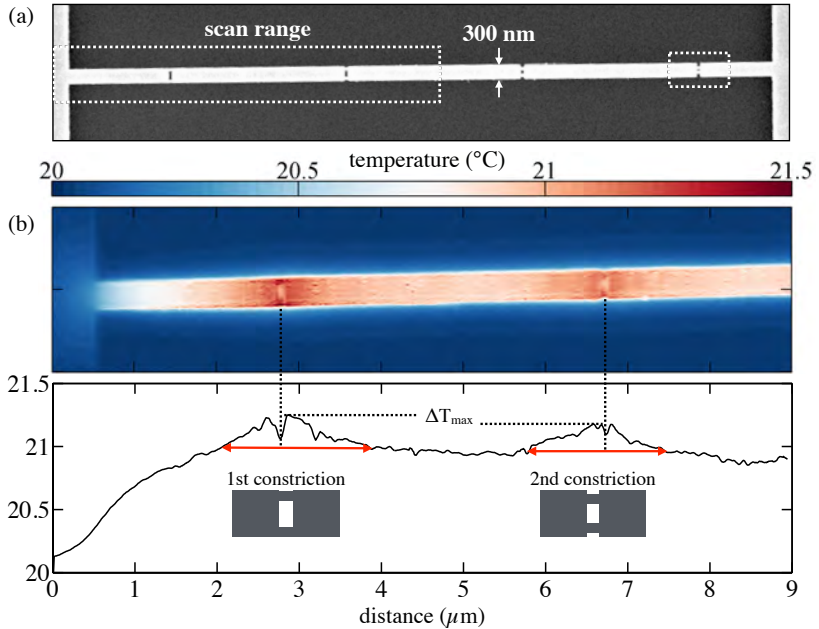


**Figure 4.8: Self-heating of a metal interconnect with nanoscopic constrictions**

(a) SEM micrograph of the 300-nm-wide interconnect with four lithographically defined constrictions. The constrictions have a width of 100 nm and 40-nm-wide bridges in between.

(b) Temperature field measured by scanning probe thermometry and the corresponding temperature profile extracted along the center of the interconnect structure. Hot spots are observed near the constrictions.

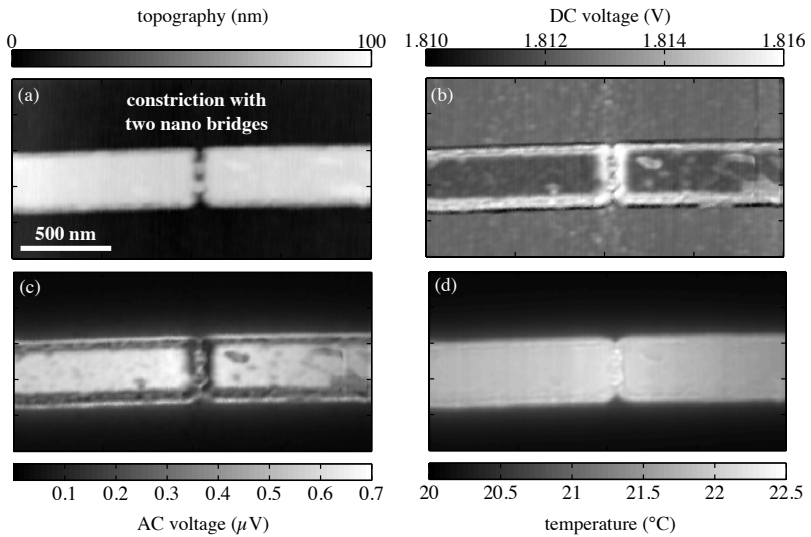


**Figure 4.9: Thermal characterization of a nanoscopic constriction**

(a) Topography image, (b) DC raw voltage signal and (c) the AC voltage amplitude in relation to (d) the temperature field determined by scanning probe thermometry.

Fig. 4.9 shows (a) the topography, (b-c) the DC and AC raw voltage signals and (d) the corresponding temperature map around the constriction. The two nanobridges of the constriction are separated by a 60 nm wide gap. While the constriction is resolved in the topography signal, the two nanobridges can be distinguished hardly in the voltage signals of the scanning probe sensor. The signals in the constriction are dominated by changes in the tip-sample contact geometry. The edges of the interconnect appear not to be etched straight down to the substrate, but tapered, with an increasing diameter towards the substrate. Despite the strong dependence on the tip-sample contact geometry as observed in the raw voltage signals, the temperature field in (d) looks very homogenous, indicating that we successfully account for the thermal-resistance-related variations of the tip-sample heat flux in the calculation of the temperature field.

To illustrate this more clearly, we plotted the temperature error map, like in the previous section, derived as the difference between the temperature field calculated for a variable ( $R_{hs}(x, y)$ ) and a constant ( $R_{hs}$ ) thermal resistance.

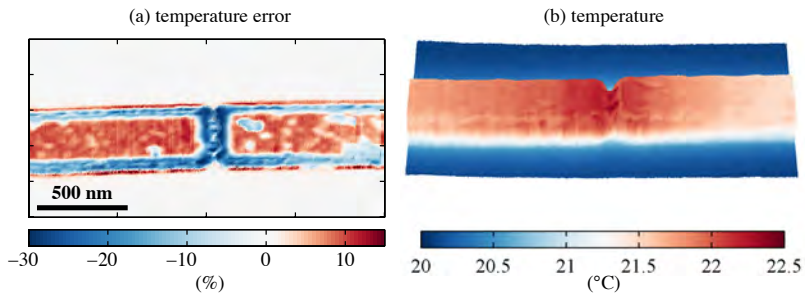


**Figure 4.10: Temperature error map and temperature-topography overlay.**

Fig. 4.10 illustrates that near the edges, and in particular in the vicinity of the nanobridges, the temperature cannot be quantified without accounting for tip-sample contact geometry related heat flux variations. The new method, however, accounts for most of the contact-geometry-related artifacts, as illustrated by the absence of edge artifacts in the temperature-topography overlay plot of the self-heated interconnect segment (b). In addition, Fig. 4.10(b) illustrates an asymmetric temperature field around the constriction, with the colder side towards the electrode pad outside the image area,  $\sim 2 \mu\text{m}$  away from the constriction. This asymmetry is comparable to the one observed at the opposite side of the interconnect structure and supports our interpretation that the observed asymmetry is related to

additional heat dissipation into the electrode pad.

Further note that the error map indicates a systematic overestimation of the temperature in the flat top region of the interconnect, if the signal is not locally weighted by the DC reference heat flux. Here, the signal difference is not related to a geometry-related heat flux variation as observed near the edges, but to the difference between the thermal resistances of the  $\text{SiN}_x$  substrate and the gold interconnect. This difference in thermal resistance is hardly visible in the DC raw voltage signal, as there the image contrast is dominated by the contact-geometry-related signal variations. However, if we calculate the tip-sample thermal resistance, we can directly observe the difference between the thermal resistance measured on  $\text{SiN}_x$  and the one on gold as shown in Fig. 4.11(a).

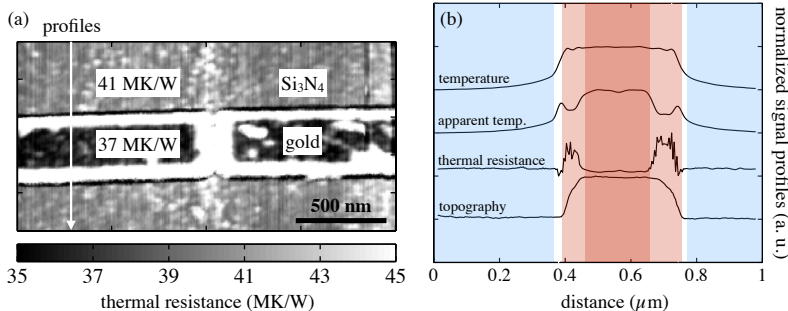


**Figure 4.11: Thermal resistance of the interconnect and cross-sectional profiles of the various measurement signals**

(a) Thermal resistance of the interconnect structure revealing the difference between gold and  $\text{SiN}_x$ .

(b) Cross-section profiles along the region depicted in (a) to visualize the interdependency between the topography, the thermal resistance, and the temperature signals acquired.

This example indicates that to quantify temperature fields, we must account not only for geometry-related-variations of the tip-sample heat flux, but also for material-related thermal resistance variations.

Finally, we aim to illustrate the interdependency of the various signals by comparison of cross-sectional profiles along the line depicted in Fig. 4.11(a). Fig. 4.11(b) shows the various normalized signals to enable a comparison between the topography, the thermal resistance, the sample temperature, and the apparent temperature. The blue-colored region corresponds to signals acquired by the tip in contact with only the  $\text{SiN}_x$  substrate, white regions corresponds to a range where the scanning probe tip is likely contacting the substrate and the interconnect simultaneously, the light-red region is the

range where the tip is in contact with the interconnect, not only with the tip apex but potentially also with the side-wall of the tip, and the red region is the range where the tip is contacting the interconnect with only the apex. If we compare, for instance, the topography signal with the thermal resistance signal, we observe that the thermal resistance is already sensitive to the interconnect in a range (white region) where the scanning probe does not yet change its vertical deflection. At the same time, we can observe significant thermal resistance variations in the range where the tip-sample contact geometry changes significantly, namely, at the edges of the interconnect structure (light-red region). On top of the interconnect, both the topographic signal and the thermal resistance signal are rather featureless. If we now compare the apparent temperature signal with the thermal resistance signal, we can directly observe that the apparent temperature is correlated to the topography-related thermal resistance variations at the interconnect edges. The temperature profile, as calculated by the new method, however, is hardly effected by the thermal resistance signal, illustrating the benefit of the proposed approach.

## 4.5 Temperature Resolution and Topography Artifacts

In the final section of this chapter, we will provide a more detailed discussion of the resolution in our measurement. Fig. 4.12 shows the interconnect constriction studied in the previous section at high spatial resolution. We can resolve the two 40-nm-wide and 100-nm-long nanobridges across the constriction in the topography image (Fig. 4.12(a)). The lateral spatial resolu-

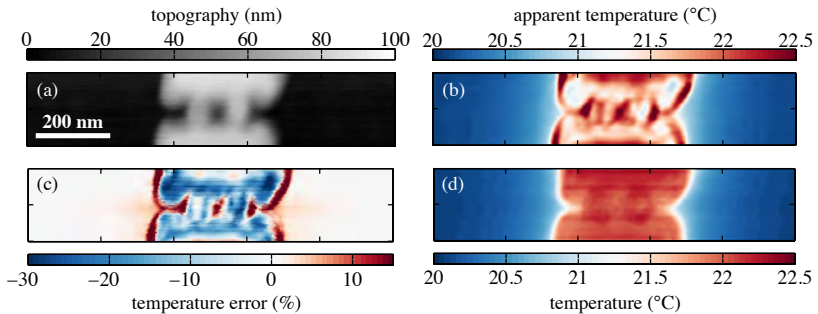


**Figure 4.12: High-resolution scans of the constriction region**

(a) Topography (b) apparent temperature, (c) temperature error map, and (d) temperature map.

tion is, however, not to be confused with the spatial temperature resolution of the experiment. Fig. 4.12(b-d) illustrate the thermal signal simultaneously acquired with the topography signal. The two constrictions cannot be identified as easily as in the topography. The apparent temperature map would even indicate three hot spots across the constriction, illustrating that topographic artifacts, as typical observed in scanning thermal microscopy experiments, can lead to a complete misinterpretation of the actual temperature field. The actual temperature map in (d) looks more homogenous, still some features indicating the position of the nanobridges are visible. The temperature error map in Fig. 4.12(c) visualizes the significant artifacts arising from the tip-sample contact-geometry-related variations in the AC heat flux signal acquired. We can actually conclude from the temperature error map that quantification of the temperature is not possible within the constriction without accounting for the topography-related signal dependence.

The temperature field calculated from simultaneous acquisition of the AC and the DC signal, however, is more homogenous. In contrast to the apparent temperature image indicating three hot spots, we observe a nearly constant temperature field along the constriction. In contrast to the two separate nanobridges visible in the topography signal, we now observe one constriction in the temperature signal. This finding is related to the shape of the tip and in particular to its opening angle. The heated tip cannot fully penetrate into the 60-nm-wide and nearly 70-nm-deep gap between the nanobridges, but always touches at least one of the bridges with the side wall. Accordingly, the tip measures a rather constant temperature as it always remains in thermal contact with the nanobridges.

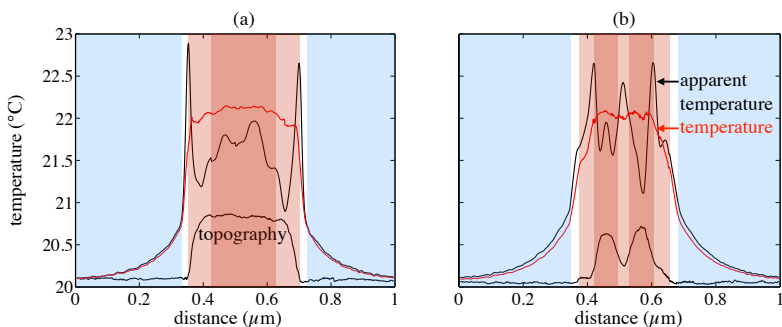


**Figure 4.13: Cross-sectional profiles along the self-heated interconnect**  
 (a) In the straight segment of the interconnect and (b) across the nanobridges within the constriction.



This interpretation is supported by the cross-sectional line scans in Fig. 4.13. Fig. 4.13(a) shows a comparison between the normalized topography signal, the apparent and the actual temperature signals across the interconnect before the constriction. We can observe that the apparent temperature signal is significantly affected by the sample topography, whereas the temperature signal is nearly constant on top of the interconnect and decaying into the substrate. In comparison, Fig. 4.13(b) shows signals acquired across the nanobridges in the constriction. From the topography line scan, we can now conclude that the tip does not touch the substrate between the two nanobridges, but remains always in contact with the interconnect.

Based on this observation, one might conclude that the spatial temperature resolution of our measurement cannot be better than 40 nm, the nominal width of the nanobridges. However, we have to acknowledge that this apparent resolution limit is only the result of the extreme topography variation in the vicinity of the constriction and not related to a variation of only the temperature field. The spatial temperature resolution in the flat part of the sample, e.g., on top of the interconnect or on the substrate, is higher. We estimate a spatial temperature resolution of  $\sim 10\text{-}20$  nm based on the smallest repetitive feature visible in the thermal signal of the scanning probe, which is likely similar to the tip-sample contact area. We have previously demonstrated a sub-10-nm spatial thermal resolution in the absence of topography variations using similar measurement conditions.

Note that a spatial temperature resolution of  $\sim 10$  nm is claimed in literature [28] from observation of topography related artifacts like those observed in the apparent temperature map in Fig. 4.13(b). Nanoscopic thermal features, like the appearance of three hot spots as visible in Fig. 4.12(b) and the cross-sectional profile in Fig. 4.13(b) can be easily misinterpreted if the topography related heat flux variations are not taken into account. A proper definition of the spatial temperature resolution would require a local variation of only the temperature field on nanoscopic length-scales in absence of topography variations.

Apart from the spatial temperature resolution, it is also interesting to examine the sample temperature resolution of our measurements. Considering the experiment on the voltage-bias-dependent self-heating of the interconnect structure we can infer a sample temperature resolution of  $\sim 30$  mK from the temperature signal acquired as a function of the AC excitation applied (see Fig. 4.7(a)), measured in a 100 Hz bandwidth. It is interesting to compare the 30 mK temperature resolution with our estimated electrical-noise-limited temperature resolution of the microscope based on the electrical noise characterization in chapter 2.5. Most easily, we can compare the predictions with our experimental results by considering the temperature resolution of the scanning probe sensor. The 30 mK sample temperature

resolution translates into a  $91 \mu\text{K}$  scanning probe sensor temperature resolution at a scanning probe temperature of  $\sim 280^\circ\text{C}$ . In chapter 2.5, we extract from the electrical noise characteristics of a different scanning probe cantilever a sensor temperature resolution of  $190 \mu\text{K}$  at a sensor temperature of  $\sim 460^\circ\text{C}$  measured at in the same bandwidth but at double the frequency. Our experimentally achieved temperature resolution is of the same order as that expected based on the electrical-noise-limited resolution. The factor of two difference is related to the use of different scanning probe cantilevers, the different temperatures of the scanning probes and the different frequency between the two measurements.

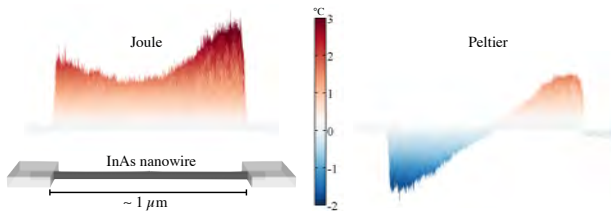
## 4.6 Conclusions

In conclusion, we presented a novel method to quantify nanoscopic temperature fields. The method provides a significant experimental improvement for the quantification of temperature fields using scanning probes. The technique is a two-path method inferring temperature by probing the total steady-state heat flux and a temporally modulated heat flux signal between the scanning probe sensor and a sample simultaneously. The novel technique minimizes contact-geometry-related artifacts so far limiting the reliability of nanoscopic temperature measurements by thermal scanning probe microscopy.

We demonstrated the new method by a study of self-heating of metal interconnects. We spatially resolved the temperature field of a 100-nm-wide gold interconnect with 30 mK sample temperature resolution, which is a three-orders-of magnitude sensitivity improvement compared with our previous attempts. Using the novel approach we could directly visualize thermal hot spots near lithographically defined defects in a 300-nm-wide interconnect. From our experimental data, we inferred a temperature resolution of the scanning probe sensor of  $91 \mu\text{K}$ , approaching the electrical-noise-limited temperature resolution of the scanning probe sensor. Our experiments indicate an outstanding performance of the novel thermal microscope that approaches the fundamental resolution limits of our scanning probe sensor.

# 5

## Imaging Local Joule and Peltier Effects in InAs Nanowires



In this chapter, we present a dual harmonic detection method for scanning probe thermometry. Advantageously, the method can be applied to experimentally separate thermophysical effects typically observed as superposition to an overall temperature field in thermal scanning probe measurements. We apply the novel technique to image the temperature increase of an InAs nanowire contacted by gold electrodes. Uniquely, we simultaneously quantify Joule heating and Peltier effects at the metal-InAs contacts with a lateral spatial resolution of  $\sim 10 \text{ nm}$  and sample temperature resolution of  $\sim 0.1 \text{ K}$ . Our work is a significant advance that enables the spatially resolved characterization of thermoelectric and electrothermal effects in operating nanoscale devices.

## 5.1 Asking Kelvin if Peltier is Cooler than Joule

In the preceding chapters of this thesis we established the instrumentation and the methodologies needed to quantify temperature fields in nanosystems. We have developed a unique instrument and method termed scanning probe thermometry. The possibility to image nanoscopic temperature fields is certainly exciting but not necessarily sufficient to understand the underlying thermophysical processes. To address this issue, we will demonstrate scanning probe thermometry beyond the quantification of overall temperature fields by extending our work to the direct experimental separation of two different thermophysical processes.

There is a whole zoo of fascinating thermophysical effects, such as Joule heating, thermoelectric effects, the pyroelectric effect, the magnetocaloric effect, the Spin-Seebeck effect and thermo-plasmonic processes to name just a few, which are largely unexplored on nanoscopic length scales. Most of these effects are known or predicted to exhibit significant structural size dependencies making it particular promising to investigate them on nanoscopic length scales. Information about these effects is typically encoded in both, the relative temperature field distributions and the absolute temperatures. However, only the latter can be quantified by the spatially averaging electrical and optical measurement methods typically applied to investigate these effects.

Therefore, we dedicate the final chapter of this thesis to an example demonstrating how scanning probe thermometry can be applied to separate different thermophysical effects. In particular, we will demonstrate how local Peltier effects at metal-semiconductor contacts can be simultaneously quantified with Joule heating. This is of direct technological relevance for the characterization of semiconductor nanoelectronics as here temperature fields are often the result of a superposition of these two effects.

Thermoelectric effects have almost exclusively been studied in the context of energy conversion for waste-heat recovery and cooling applications [113]. However, thermoelectric effects are also of tremendous importance for nanoelectronic devices. In particular nanoscale electronics directly using thermal processes, like phase-change memory cells, are strongly affected by the Peltier and the Thomson effect [114]. Considering current trends in electronics, such as the integration of novel materials and structural scaling, every serious effort to develop devices for information processing should take nanoscopic thermal processes and principles into account.

While so far mainly Joule heating has been recognized to impact device performance and reliability of integrated circuits [65, 107, 115], thermoelec-

tric effects are expected to gain further importance. CMOS technology is already thermally limited and the predicted integration of novel materials like III/V semiconductors into existing silicon technology will definitely reinforce the dependence on thermal processes and properties. Not only the low thermal conductivities of the materials themselves are problematic but also the contacts between different adjacent materials. The appearance of Peltier effects intrinsically located at metal-semiconductor and semiconductor-semiconductor interfaces are likely to further complicate the understanding and design of devices approaching their structural limits. Heat dissipation is not only going to be impeded by interfaces but heat will also be modulated very locally by thermoelectric and thermionic interface effects. These effects in combination with the increasing thermal boundary resistances due to surface-to-volume scaling and the integration of new device topologies, such as nanowire geometries, may lead to device properties that are difficult to predict. This poses serious challenges to the development of improved semiconductor electronics.

On the other hand, one may also speculate that based on a deepened understanding of thermal interface processes, thermal engineering approaches might emerge to control electrical device performances in semiconductor nanoelectronics, e.g., thermally assisted tunneling of electrons across barriers or the dissipation of heat from nanoscopic hot spots.

In order to address these urgent needs to explore electrothermal and thermoelectric processes in more detail, we describe how scanning probe thermometry can be applied to measure the related temperature fields, ultimately testing if Peltier or Joule is cooler.

## 5.2 Dual Harmonic Detection for Scanning Probe Thermometry

In this section, we will introduce a dual harmonic detection method for scanning probe thermometry. The method is an extension to the heat flux reference method presented in the preceding chapter. We will experimentally demonstrate the approach in the next section by spatially resolving Joule and Peltier effects in an InAs nanowire contacted by gold electrodes.

The method is motivated by the need to gain further information about the thermophysical processes giving rise to the overall temperature field typically observed in scanning thermal microscopy measurements [13, 25, 28, 29, 55]. In our previous experiments reporting the self-heating of silicon nanowires [27], we spatially resolved an overall temperature increase as the

result of combined Joule and Peltier effects. In those DC scanning thermal microscopy measurements, two different thermophysical processes were superimposed making it difficult to understand the underlying mechanisms giving rise to the observed temperature field.

The idea of the dual-harmonic detection method is to separate these two effects by their different scaling dependencies on an applied electrical current. By applying a sinusoidal voltage bias excitation the Peltier effect can be distinguished from Joule heating as the former has a linear dependence on the applied current ( $I$ ), whereas Joule heating has a quadratic response. As demonstrated in the experiments on self-heating of metal interconnects in chapter 4, Joule heating of a linear resistor ( $R$ ) scales as

$$\dot{Q} = R \times I^2 \quad (5.1)$$

In contrast, the Peltier effect is a function of the difference in the Peltier coefficient ( $\Delta\Pi$ ) between the two contacting materials and the applied current, scaling as

$$\dot{Q} = \Delta\Pi \times I \quad (5.2)$$

As consequence, both effects can be separated in an AC scanning probe thermometry measurement as the two effects manifest at different harmonics of the scanning probe signal if an AC current ( $I = I_0 \times \sin(\omega t)$ ) is applied. The Joule-heating-related temperature increase of the device leads to a DC response ( $V_{Lev,0}$ ) and an AC voltage response ( $V_{Lev,2}$ ) in the second harmonic of the scanning probe sensor. In chapter 4, we already derived how the DC and second harmonic AC voltage bias can be related to the temperature increase of an interconnect. In short, we first calculate the heater temperature increase of the scanning probe sensor ( $T_h$ ) and the heat flux between the scanning probe and the device ( $Q_{hs}$ ) by rescaling of the DC ( $V_{Lev,0}$ ) and AC ( $V_{Lev,2}$ ) voltage raw signals. Based on these quantities, we derive the sample temperature increase ( $T_s$ ) according to Eq. 4.4 in chapter 4.2. The sample temperature ( $T_s$ ) in response to combined Joule and Peltier effects is modulated as

$$T_s = T_{s,0} + T_{s,1} \sin(\omega t) + T_{s,2} \sin(2\omega t), \quad (5.3)$$

with  $T_{s,1}$  being proportional to the Peltier effect ( $1\omega$ ) and  $T_{s,2}$  being proportional to the Joule effect ( $2\omega$ ). The electrical voltage bias measured across the scanning probe sensor accordingly has three temporal components

$$V_{Lev} = V_{Lev,0} + V_{Lev,1} \sin(\omega t) + V_{Lev,2} \sin(2\omega t), \quad (5.4)$$

The heater temperature  $T_h(V_{Lev})$  can directly be calculated from measurement of the DC ( $V_{Lev,0}$ ) and AC voltage bias components ( $V_{Lev,1}$ ,  $V_{Lev,2}$ ) as discussed in chapter 4. The total electrical power dissipated in the scanning probe sensor needed to quantify the heat flux gets modified because of the additional linear AC component ( $V_{Lev,1}$ ) measured in the first harmonic of the lock-in amplifier. Accordingly, the electrical power ( $P_{el}$ ) dissipated in the scanning probe reads

$$\begin{aligned}
 P_{el} &= P_{el,0} + P_{el,1} \sin(\omega t) + P_{el,2} \sin(2\omega t) + P_{el,3} \sin(3\omega t) + P_{el,4} \sin(4\omega t) \\
 P_{el,0} &= \frac{1}{R_{series}} \left[ V_{Tot} V_{Lev,0} - V_{Lev,0}^2 - \frac{1}{2} V_{Lev,1}^2 - \frac{1}{2} V_{Lev,2}^2 \right] \\
 P_{el,1} &= \frac{1}{R_{series}} [V_{Tot} V_{Lev,1} - 2 \times V_{Lev,0} V_{Lev,1} - V_{Lev,1} V_{Lev,2}] \\
 P_{el,2} &= \frac{1}{R_{series}} \left[ V_{Tot} V_{Lev,2} - 2 \times V_{Lev,0} V_{Lev,2} - \frac{1}{2} V_{Lev,1}^2 \right] \\
 P_{el,3} &= \frac{1}{R_{series}} [V_{Lev,1} V_{Lev,2}] \\
 P_{el,4} &= \frac{1}{R_{series}} \left[ \frac{1}{2} V_{Lev,2}^2 \right]
 \end{aligned}$$

having two additional components ( $P_{el,1}, P_{el,3}$ ). Note, that also the even components ( $P_{el,0}, P_{el,2}$ ) related to the Joule heating of the sample are modified by the linear AC component ( $V_{Lev,1}$ ). The effect on the overall power dissipated is, however, very small as the AC voltage response of the scanning probe measured in the first harmonic ( $V_{Lev,1}$ ) is about five orders of magnitude smaller than the DC voltage ( $V_{Lev,0}$ ).

Based on measurements of the different temporal components of the electrical power dissipated in the scanning probe ( $P_{el,0}, P_{el,1}, P_{el,2}$ ), the sample temperature increase due to Joule heating ( $T_{s,2}$ ) and Peltier heating ( $T_{s,1}$ ) can be quantified by dual harmonic scanning probe thermometry.

Similar detection approaches have previously been reported to quantify Joule and Peltier effects with techniques that differ from scanning probe thermometry. In particular Vermeersch et al. reported the observation of Joule and Peltier effects in thermoelectric modules optically imaged by thermoreflectance microscopy [116]. Recently, Grosse et al. adapted a dual harmonic detection scheme to extract temperature-related signals using scanning Joule expansion microscopy [39]. They reported the observation of Joule- and Peltier-related effects in a  $\text{Ge}_2\text{Sb}_2\text{Te}_2$  thin film. Note that in studies of non-linear electrical devices, like phase-change memory cells, the simple separation of Joule and Peltier effects into a first and a second harmonic response

of a sensor element is not valid, and a more detailed analysis is required to separate Joule and Peltier effects.

### 5.3 Observation of Joule and Peltier Effects in an InAs Nanowire

To demonstrate the described approach experimentally, we studied self-heating of indium arsenide (InAs) nanowires. The nanowire investigated in the following study was grown by metal-organic vapor-phase epitaxy on a silicon(111) wafer by H. Schmid [117]. The nanowire ( $\sim 120$  nm diameter) was separated from the growth substrate and transferred to a silicon (Si) substrate covered with a  $\sim 100$ -nm-thick silicon oxide. Electrical contacts (Au/Ni) were fabricated by e-beam lithography by P. Mensch. Note that in further experiments also thinner nanowires (down to 20 nm diameter) grown by gold-catalyzed metal-organic chemical vapor deposition were studied.

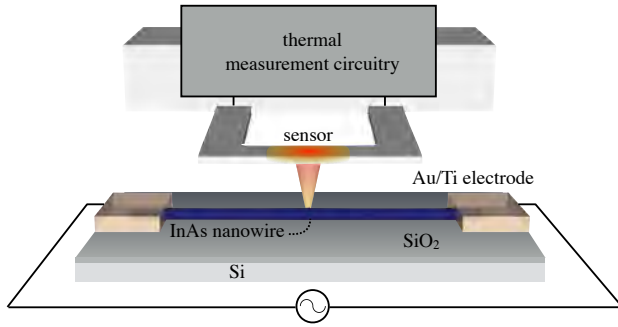
In a first experiment, a bipolar AC voltage bias (10 kHz,  $0.7 V_{pp}$ ) was applied to the nanowire as illustrated in Fig. 5.1, creating an oscillating temperature field. The scanning probe sensor was calibrated by the electrical fix-point calibration method (see chapter 2.4) and self-heated to a temperature of  $86^\circ\text{C}$  by the applied DC sensing voltage bias. The thermal scanning probe was moved into sample contact and raster-scanned at a scan speed of 3 ms per pixel. The heat-flux-related DC and AC voltage bias components of the scanning probe sensor were simultaneously recorded by the electrical measurement circuitry illustrated in chapter 2.3 as a function of the scanning probe position.

Fig. 5.2 shows the DC voltage bias in comparison to the AC raw voltage signal ( $V_{Lev,2}$ ) measured in the second harmonic ( $2\omega$ ) of the lock-in amplifier.

In the DC voltage image of Fig. 5.2(a), we can clearly identify the InAs nanowire on top of the  $\text{SiO}_2$  substrate and the two metal electrodes. The nanowire has a thermally measured width of  $\sim 200$  nm, which is larger than the nominal width of  $\sim 120$  nm because of the tip-shape convolution. Major signal variations are observed near the electrical contacts and the nanowire edges. These topography-related signals illustrate the tip-sample contact-size dependence of the heat flux between the scanning probe sensor and the sample (see discussion in chapter 4).

This dependence also manifests in the AC raw voltage signal amplitude ( $V_{Lev,2}$ ) shown in Fig. 5.2(b). In particular, we observe large voltage amplitudes at the edges of the self-heated nanowire. These edge signals are related





**Figure 5.1: Illustration of the experiment**

showing the scanning probe in thermal contact with the InAs nanowire electrically contacted by two Au/Ti electrodes. An AC voltage bias is applied to the nanowire and the temperature-dependent voltage response of the scanning probe sensor is acquired by the electrical measurement circuitry illustrated in chapter 2.3, including two lock-in amplifiers.

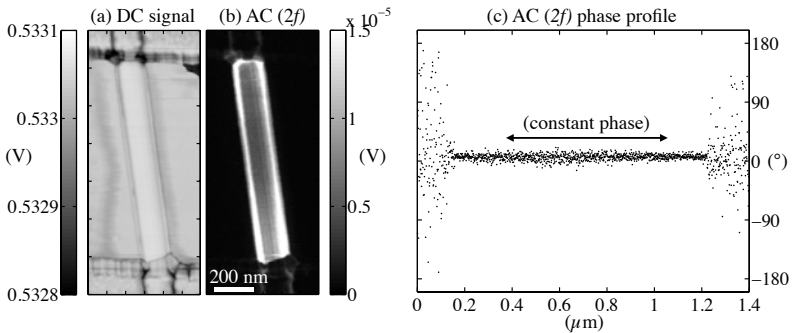


**Figure 5.2: DC and AC raw voltage ( $V_{Lev,2}$ ) signals**

(a) DC voltage bias ( $V_{Lev,0}$ ) measured across the scanning probe sensor  
 (b) AC voltage bias amplitude ( $V_{Lev,2}$ ) acquired in the second harmonic of the sensor signal  
 (c) AC ( $V_{Lev,2}$ ) phase signal line profile along the nanowire length direction

to the decrease of the thermal resistance between the scanning probe and the sample as the tip-sample contact area gets increased by the topography variation. Fig. 5.2(c) shows the related phase signal, which is constant along the length of the nanowire.

In contrast, we observe a  $180^\circ$  phase shift in the first harmonic of the scanning probe voltage ( $V_{Lev,1}$ ) simultaneously recorded (see Fig. 5.3). Fig. 5.3(a) shows the acquired AC voltage amplitude ( $V_{Lev,1}$ ) and the related phase image in (b). We observe a vanishing voltage amplitude in the center of the

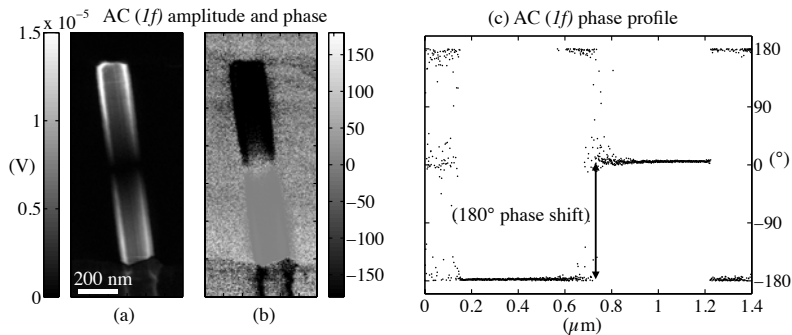


**Figure 5.3: AC raw voltage signal ( $V_{Lev,1}$ )**

(a) AC voltage amplitude ( $V_{Lev,1}$ ) acquired in the first harmonic response of the scanning probe sensor signal.

(b) corresponding phase image

(c) phase line profile along the center of nanowire illustrating a  $180^\circ$  phase shift near the center of the nanowire.

nanowire corresponding to the  $180^\circ$  phase shift between the two electrical contacts (see Fig. 5.3(c)). The observed phase shift can be related to bias-polarity-dependent Peltier effects at the opposite metal/InAs contacts, leading to a heating and a cooling, respectively, as discussed in the following.

To quantify the sample temperature field from the electrical DC and AC voltages measured across the scanning probe sensor, we apply the dual harmonic heat-flux reference method derived in the preceding section 5.2 and chapter 4.2 to the raw image signals of Fig. 5.2 and Fig. 5.3.

The overall sample temperature increase is characterized by a steady-state temperature increase ( $T_{s,0}$ ) due to the Joule heating superimposed by two transient temperature fields recorded in the first ( $T_{s,1}$ ) and second harmonic response ( $T_{s,2}$ ) of the scanning probe signal. As discussed in the chapter 4 we can approximate the device temperature field as being independent of the

voltage excitation frequency because the expected thermal time constant ( $\tau$ ) of the nanowire is less than the applied excitation frequency. Accordingly, the steady-state temperature increase ( $T_{s,0}$ ) equals the maximum amplitude of the second harmonic temperature modulation of the device ( $T_{s,1}$ ), whereas the Peltier-related temperature modulation ( $T_{s,1}$ ) equals zero in the time average.

Fig. 5.4(a) shows the steady-state temperature increase of the device ( $T_{s,0}$ ) and a temporal snapshot of the superimposed Peltier temperature field ( $T_{s,1}$ ) at maximum signal amplitude in (b).

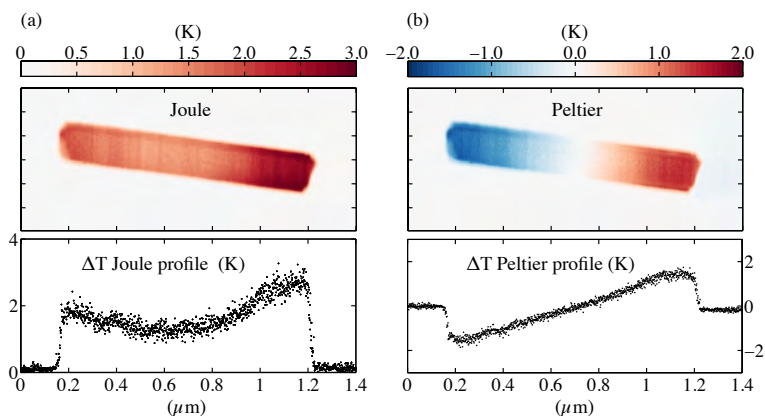


**Figure 5.4: Joule and Peltier temperature fields**

(a) Steady-state Joule temperature increase  $T_{s,0}$  and corresponding line profile along the center of the nanowire. We observe preferential Joule heating of the metal/InAs contacts.

(b) Temporal snapshot of the Peltier temperature field at maximum signal amplitude and corresponding line profile along the nanowire center.

Interestingly, the Joule-heating related steady-state temperature increase of the nanowire does not show a parabolic temperature profile as observed in chapter 4 where the self-heating of a metal interconnect was studied. Instead, we find the largest temperature increase at the metal/nanowire contacts leading to an inverse parabolic temperature field as illustrated in the line profile in Fig. 5.4(a). The asymmetry of the temperature field indicates an asymmetric heating of the contact region. Contact-dominated heating is a feature of this particular nanowire, while the significant dependence of the temperature field on the electrical contact properties is a general feature we

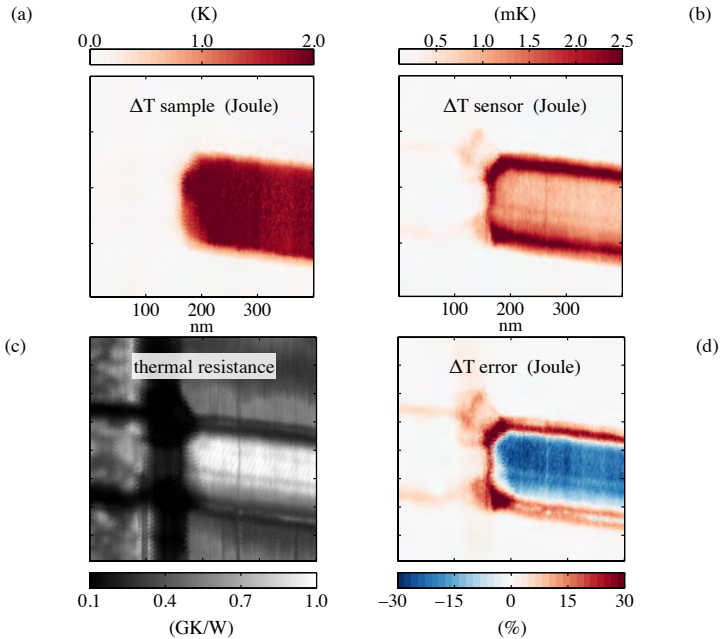
observed during investigations of different nanowires.

Fig. 5.4(b,d) illustrate the Peltier temperature modulation ( $T_{s,0}$ ) at maximum signal amplitude. Both contacts are Peltier heat sources of opposite sign as illustrated by the symmetrical temperature field along the nanowire length direction in Fig. 5.4(d), showing the temporal cooling of the left contact and the heating of the right contact. The typical exponential temperature decay from the contacts towards the nanowire center is little pronounced, and we observe only a slight nonlinearity in the temperature profile. The approximately linear appearance of the Peltier temperature profile can be explained by the interference between the two heat sources of opposite sign as two overlapping exponential temperature fields with a decay length similar to or larger than the length of the nanowire ( $\sim 1 \mu\text{m}$ ) look more linearly in the center.

Importantly, we can observe that both the Joule and the Peltier temperature field are homogenous along the length and the cross-section of the nanowire. We successfully reduced topography-related artifacts near edges and contacts, while they are clearly visible in the corresponding raw voltage signals shown in Fig. 5.2 and Fig. 5.3. Note that no post-processing of the raw data, such as filtering, was performed and the temperature fields are directly calculated from the voltage raw signals. Exclusion of topography-related artifact is very important for our measurements as we aim to quantify thermal processes in the vicinity of the metal-semiconductor contacts characterized by significant topography variations of about 150 nm. Previous studies [27–29, 57], including our own work, suffered from topography-related artifacts limiting the possibilities to quantify thermal processes at nanoscopic contacts.

Using our novel method, we overcame this limitation. To illustrate the benefit of the new approach even more clearly, we will show our ability to characterize thermal processes in the vicinity of the electrical contacts. Fig. 5.5(a) illustrates the Joule heating of the left contact in more detail.

The homogenous temperature field in Fig. 5.5(a) i.e., the absence of nanoscopic features may appear unspectacular, but is an important finding. Frequently, nanoscopic features observed in scanning thermal microscopy measurements [27–29, 57] are likely related to topography artifacts that can easily be misinterpreted. Major errors can arise if the heat-flux-dependent temperature signal of a scanning probe sensor is simply rescaled to a sample temperature. The Joule-heating-related steady-state temperature increase of the sensor element shown in Fig. 5.5(b) is not only orders of magnitudes smaller than the



**Figure 5.5: Joule heating of the left nanowire/metal contact**

(a) Sample temperature field illustrating a homogenous temperature distribution

(b) Sensor temperature field signal affected by topography artifacts at the nanowire edges and contacts

(c) Tip-sample thermal resistance image illustrating the position dependence of the signal.

(d) Temperature error map calculated as the difference between the actual sample temperature (in a) and the apparent sample temperature inferred by rescaling the sensor temperature (b) with a position-independent thermal resistance.

temperature of the sample, but also differs spatially from the sample temperature field. This is illustrated by a direct comparison of Fig. 5.5(a) and (b).

The sensor temperature increase in response to the position-dependent heat flux between the scanning probe and the sample is affected by contact-geometry-related changes in the tip-sample thermal resistance ( $R_{ts}$ ). To illustrate this dependence clearly, we show the spatial variation of the thermal resistance in Fig. 5.5(c). We observe major variations in the thermal resistance at the nanowire and metal contact edges, which, if not included into the analysis of the sample temperature field lead to a significant overestimation of the sample temperature. Fig. 5.5(d) illustrates this overestimation on the order of 30 % of the actual sample temperature field in the red colored regions.

Additionally, we observe not only topography-related artifacts disturbing the quantification of the sample temperature field, but also material-related variations of the position-dependent thermal resistance  $R_{ts}(x, y)$  that need to be included. The thermal resistance between the silicon scanning probe covered by a native oxide and the InAs nanowire is larger than the thermal resistance to the  $\text{SiO}_2$  substrate, most likely because the interface-dominated thermal resistance of a  $\text{SiO}_2/\text{SiO}_2\text{-Si}$  contact is less than that of a  $\text{InAs}/\text{SiO}_2\text{-Si}$  contact. This is apparent from the brighter appearance of the InAs nanowire in Fig. 5.5(c) and needs to be included in the analysis of the sample temperature field. Otherwise the nanowire temperature gets significantly underestimated by up to 30%, as illustrated by the blue colored region in Fig. 5.5(c).

Here we made the effort to highlight the difference between the scanning probe sensor temperature signal and the actual sample temperature in relation to material and topography-related thermal resistance variations because measurements ignoring this aspects are frequently reported in literature [15, 18, 28, 29], making the technique apparently unreliable.

Next we report an observation closely related to our ability to quantify temperature fields in the vicinity of the electrical contacts. Investigation of the metal-semiconductor contact region is of particular interest as here a very localized Peltier heat source is located. A close look on the Peltier line-profile in Fig. 5.4(b) reveals in interesting observation. We can observe plateau-like temperature regions in the nanowire segments closest to the metal contact. To highlight these observation we reproduce the Peltier temperature profile of 5.4(b) in comparison to the thermal resistance profile along the nanowire length in Fig. 5.6(a).

The thermal resistance profile is an average across the 90-nm-wide flat top-region of the nanowire. In comparison, the red curve in Fig. 5.6(b) is an average of the Peltier temperature profile of the same width, while the

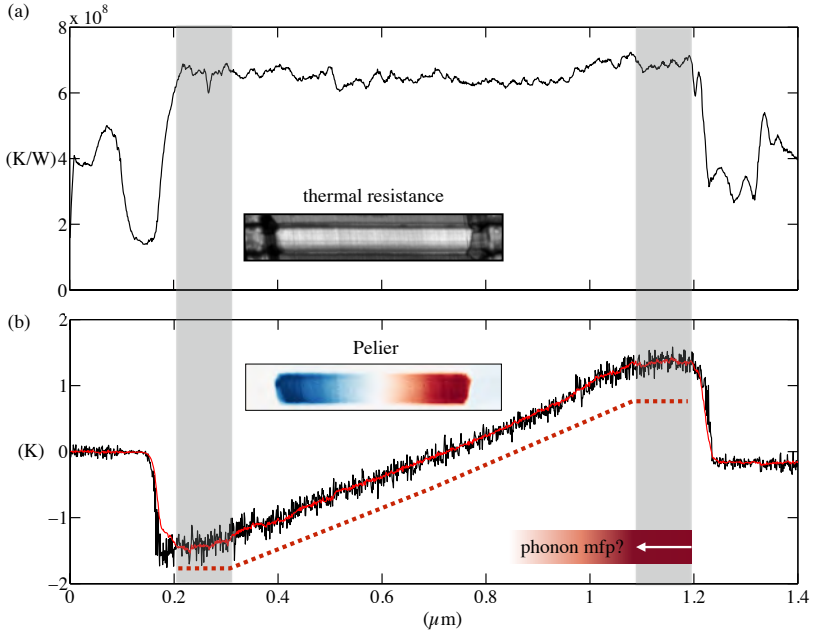


**Figure 5.6: Thermal Resistance and Peltier temperature profiles**

(a) Thermal resistance profile along the nanowire length direction calculated as an average over the 90 nm wide top region of the nanowire.

(b) Corresponding Peltier temperature profile (red line) and a single line profile (black line) corresponding to a width of 1 nm. Interestingly, we observe plateau-like temperature regions (gray shaded regions) in the nanowire segments closest to the contact, potentially related to the mean-free path of phonons emitted from the Peltier sources located at the interfaces.

black line is a single line profile of 1 nm width. Interestingly, we observe plateau-like regions in the Peltier temperature signal as indicated by the gray shaded regions in segments of the nanowire, which are not affected by potential topography related artifacts. By comparison to the thermal resistance profile in (a) we can exclude the regions which are potentially affected by signal variations due to changes of the tip-sample contact area. These regions have a width of about 30 nm while the gray shaded regions of the plateaus extend over about 100 nm.

A plateau-like region as observed in our measurements is an interesting finding. It might be related to the average mean free path (mfp) of phonons emitted from the Peltier heat source located at the interface. Based on the nanowire diameter of  $\sim 120$  nm a surface-scattering-limited mfp (Casimir limit) in that range could be expected. If this interpretation of the plateau-like temperature region is true it would be the first time the mfp of a nanoscopic heat source has been imaged in real-space. Our interpretation is certainly speculative and further experimental data needs to be evaluated in order to confirm this observation.

In the final paragraph of this section we aim to illustrate the temporal evolution of the sample temperature field. The Peltier temperature image shown in the previous figures is only a temporal snapshot of an oscillating temperature field, and the time-averaged thermoelectric response of the nanowire to a bipolar AC voltage bias is zero. Fig. 5.7 illustrates the evolution of the nanowire temperature as a function of time as extracted from the phase dependence of the sample experimental measurement.

The steady-state temperature increase ( $T_{s,0}$ ) relative to ambient temperature is shown in the first row and is independent of the excitation frequency. In contrast, the Peltier component of the temperature field ( $T_{s,1}$ ) is switching once in polarity within one period of the applied frequency corresponding to 0.1 ms. Each of the two nanowire contacts is once heated and cooled. The Joule-related temperature modulation ( $T_{s,2}$ ), illustrated in the third row of Fig. 5.7, oscillates at twice the frequency around the steady-state temperature increase. The overall time-dependent temperature field of the nanowire ( $T_s$ ), including the steady-state temperature increase and the two modulating temperature fields, is shown in the bottom row. Note that the total temperature ( $T_s$ ) is represented relative to ambient temperature, while the Joule and Peltier temperature modulations are illustrated relative to the steady-state temperature increase ( $T_{s,0}$ ) of the nanowire. By the representation relative to ambient temperature we can recognize that the sample temperature ( $T_s$ ) of the nanowire remains above ambient temperature at any time and no cooling of the nanowire due to the Peltier effect is achieved.



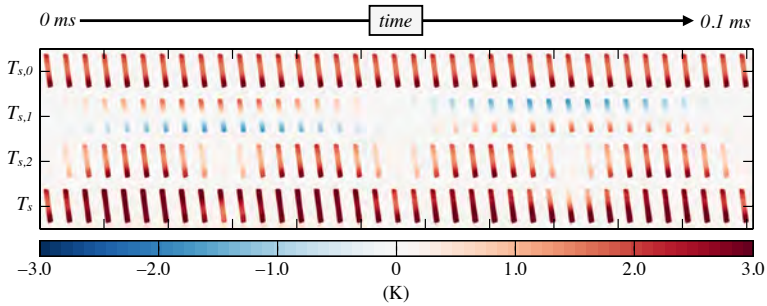


**Figure 5.7: Temporal evolution of the sample temperature field** showing the steady-state DC temperature increase ( $T_{s,0}$ ) in comparison to the Peltier ( $T_{s,1}$ ) and Joule ( $T_{s,2}$ ) temperature modulations relative to ( $T_{s,0}$ ). The Peltier temperature amplitude flips ones in polarity while the Joule heating modulates at twice the frequency. The combined sum ( $T_s$  in the bottom row) shows that the overall sample temperature remains above ambient temperature at any location and time within one excitation period.

In contrast, we will illustrate that a local temporal cooling of the nanowire can be achieved at lower voltage bias excitation due to the different scaling of the Peltier and Joule effects as investigated in the following section.

## 5.4 Bias-Dependent Investigation of Joule and Peltier Effects

In this section we investigate the voltage bias dependence of the nanowire temperature field components. Four different AC voltage excitation frequencies were applied to the nanowire and the temperature field components were characterized as discussed in the previous section. Fig. 5.8(a) shows the DC steady-state temperature increase ( $T_{s,0}$ ) due to Joule heating in comparison to the simultaneously recorded Peltier temperature amplitude ( $T_{s,1}$ ) in Fig. 5.8(b).

Note that the Peltier temperature field ( $T_{s,1}$ ) is now plotted as amplitude signal because the phase information is not needed to illustrate the bias dependent evolution of the Peltier temperature in comparison with the steady-state temperature increase ( $T_{s,0}$ ). For the low excitation bias of 0.2 V we observe a vanishing Joule heating, while the Peltier heating/cooling is significantly larger. With increasing voltage bias the trend is reversed and

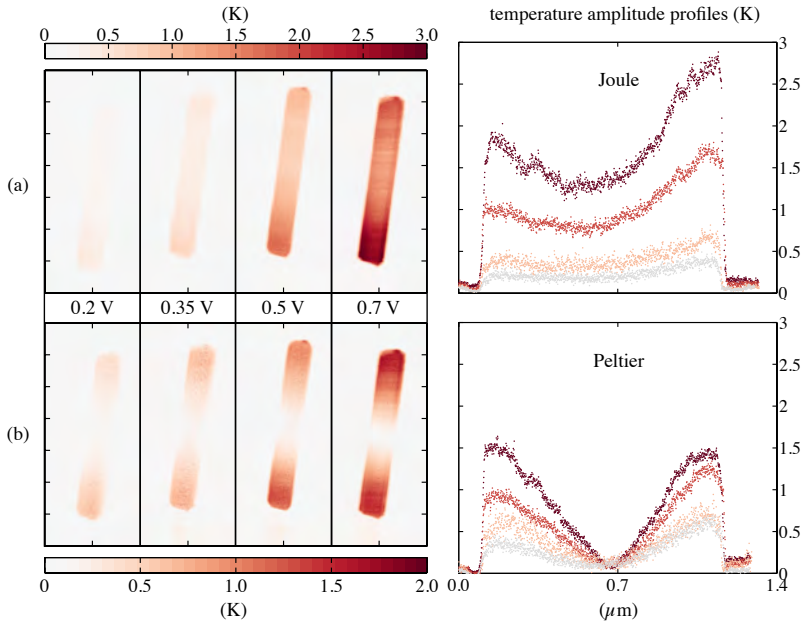


**Figure 5.8: Joule and Peltier temperature amplitude as function of the applied voltage bias**

- (a) Steady-state ( $T_{s,0}$ ) temperature increase at different voltage bias excitation and corresponding profiles along the nanowire length direction.  
 (b) Peltier temperature amplitude ( $T_{s,1}$ ) at different voltage bias excitation and corresponding profiles along the nanowire length direction.

the Joule heating exceeds the Peltier cooling/heating at the contacts. This can easily be visualized from the thermal images and the temperature profiles extracted along the nanowire-length, with each data point being a cross-sectional average of a 20-nm-wide section on the flat top of the nanowire. The maximum Joule temperature on the right contact increases from about 0.4 K to 2.8 K while the Peltier temperature amplitude simultaneously increases from 0.6 K to 1.4 K. The Peltier temperature amplitude exceeds the steady-state temperature increase ( $T_{s,0}$ ) at low voltage bias. Accordingly, parts of the nanowire are temporally cooled below ambient temperature within one excitation period as the Joule temperature modulation around the steady-state temperature gets zero at maximum amplitude of the Peltier temperature modulation. The appearance of temporal cooling effects at the nanowire contacts in a voltage bias regime between about  $\sim 0-0.6 V_{pp}$  is an interesting finding, as this is the supply voltage bias range projected for future nanowire electronic devices [118]. It illustrates that Peltier effects are likely to dominate over Joule heating in low-power nanoelectronics highlighting the importance to investigate thermal interface effects experimentally.

The voltage bias dependent study of the nanowire temperature field components is an important aspect of this work as it illustrates the different scaling of the temperature signals acquired in the two different harmonics, assigned to the Joule heating and the Peltier effect. The Peltier effect scales faster in the low voltage bias regime, whereas the Joule temperature exceeds the Peltier temperature amplitude at larger voltage bias. To illustrate this clearly we plotted the average Joule temperature increase along the nanowire and the average Peltier temperature amplitude as a function of the applied voltage bias in Fig. 5.9.

Each experimental data point corresponds to an average temperature amplitude calculated as the mean of the temperature amplitude profiles along the nanowire segment in Fig. 5.8. The fit to the experimental data points in Fig. 5.9(a) shows a quadratic dependence of the second harmonic temperature increase while the fit in Fig. 5.9(b) illustrates a linear dependency of the measured first harmonic temperature signal as function of the applied voltage bias. Observation of these two scaling dependencies is an important finding of this study as it supports our conclusion that pure Joule heating is observed in the second harmonic and Peltier heating/cooling in the first harmonic response of the scanning probe sensor.

The spatially resolved separation of these two effects on nanoscopic length scales may potentially be used to characterize both the thermal conductivity of the nanowire as well as the Peltier coefficient by fitting the measured

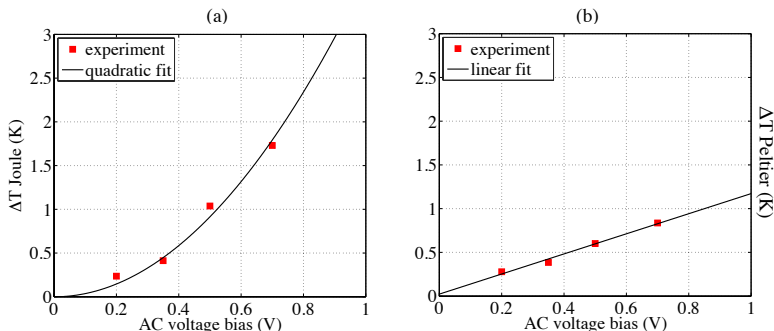


**Figure 5.9: Mean temperatures as function of the voltage bias**

(a) Average steady-state temperature ( $T_{s,0}$ ) increase of the nanowire as function of the voltage bias. The fit illustrates a quadratic scaling as typical for Joule heating.

(b) Average Peltier temperature amplitude ( $T_{s,1}$ ) of the nanowire as function of the voltage bias. The fit illustrates a linear scaling as typical for Peltier heating/cooling.

temperature fields to an appropriate heat-transfer model. Most interestingly, the new approach to image nanoscopic Joule and Peltier temperature fields in real space could enable a full thermoelectric characterization of nanoscale electronic and thermoelectric devices. This is an unsolved experimental challenge as already the characterization of simple structures like nanowires typically requires the lithographic fabrication of sophisticated measurement structures, e.g., based on suspended heat bridges and micro-heater thermometers to characterize these properties simultaneously [113, 119].

Even beyond the direct characterization of thermal material properties one could envision that scanning probe thermometry as function of additional parameters such as a gate voltage bias applied to the nanowire may be used to extract further material properties like the charge-carrier mobility via its relation to the Seebeck coefficient [120]. Overall, new exciting opportunities for the experimental characterization of nanoelectronic devices and material properties are expected to evolve based on our work.

## 5.5 Bipolar versus Unipolar Detection

In addition to the bipolar excitation of the nanowire, we validated our temperature measurement by studying the self-heating of the nanowire under unipolar AC excitation with two different polarities of the DC voltage offset.

It is interesting to study the local temperature fields also in presence of an applied DC voltage bias offset as the operation of many nanoelectronic device requires the supply of a DC voltage bias. Accordingly, the nanowire is now self-heated by a superposition of a continuous DC voltage bias and an AC voltage bias modulation of twice the DC offset amplitude as illustrated in Fig. 5.10.

While the Joule heating response is always positive leading to a heating

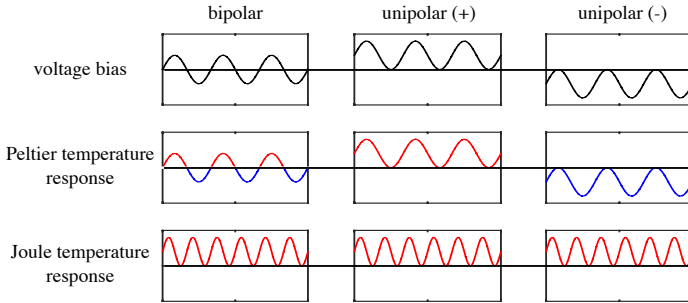


**Figure 5.10: Bipolar versus unipolar excitation**

illustrating the different voltage bias excitation scheme applied in relation to the corresponding Joule and Peltier temperature response of the nanowire.

of the nanowire, the Peltier response can either be positive or negative depending on the polarity of the DC offset voltage bias.

Fig. 5.11 shows the temperature fields measured in the first harmonic of the scanning probe sensor response as a function of the DC offset polarity. In contrast to the rather symmetric heating observed in experiments using a bipolar voltage excitation of the nanowire, we now observe a significant asymmetry in the temperature response as a function of the DC offset polarity (see Fig. 5.11). The polarity-dependent heating towards a contact is expected as the Peltier effects at the metal-semiconductor contacts in response to the DC offset voltage no longer cancel out in the time average but lead to an overall heating/cooling (see Fig. 5.10). As the Peltier effect is a function of the current direction, each contact is once cooled and heated depending on the polarity of the DC voltage bias offset.

Accordingly, the first harmonic signal in response to an unipolar AC excitation of the nanowire is no longer specific to only the Peltier effect of the nanowire, but is a superposition of the Joule heating and the Peltier

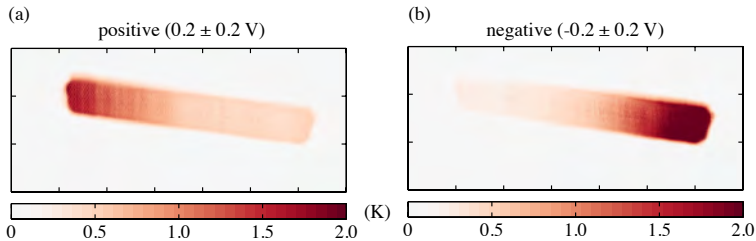


**Figure 5.11: Temperature field under unipolar heating**

- (a) positive bias offset  
(b) negative bias offset

effect. Interestingly, this superposition is linear for a linear electrical device [116] and the two measurements at different DC polarity can be applied to reconstruct the Peltier and Joule signal components. While we can no longer quantify the Peltier and Joule related temperature field simultaneously, we can still calculate the Joule temperature field component ( $T_{s,2}$ ) and the Peltier temperature amplitude ( $T_{s,1}$ ) based on the two distinct measurement scans as [116]

$$\text{Peltier : } T_{s,1} = \frac{T_{\text{pos}} - T_{\text{neg}}}{2} \quad (5.5)$$

$$\text{Joule : } T_{s,2} = \frac{T_{\text{pos}} + T_{\text{neg}}}{2} \quad (5.6)$$

Note that Eq. 5.5 and Eq. 5.6 only hold for a linear device and do not account for the potentially different phase dependence of the two effects. If we apply Eq. 5.5 and Eq. 5.6 to the temperature images shown in Fig. 5.11 we can reconstruct the Joule and Peltier temperature fields as shown in Fig. 5.12.

Fig. 5.12 illustrates the Joule and Peltier temperature fields reconstructed from the unipolar excitation measurement in comparison to a bipolar excitation measurement at slightly lower amplitude (0.5 V). We can observe a substantial similarity between the Peltier and Joule temperature fields measured in response to a bipolar excitation and the temperature fields reconstructed from two unipolar AC excitation measurements. In both cases, we observe a rather symmetric temperature profile, with preferential Joule heating of the contacts and Peltier effects.

The substantial agreement between the unipolar and the bipolar characterization of the temperature fields measured in the first and second harmonics of the scanning probe sensor supports our conclusion that we observe Joule

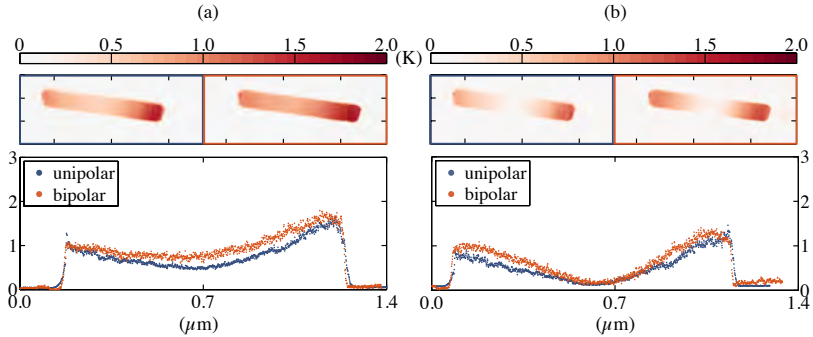


**Figure 5.12: Reconstructed Joule and Peltier temperature amplitudes**

(a) Reconstructed Joule temperature amplitude (blue box and line) in comparison to the Joule temperature amplitude measured during bipolar excitation of the nanowire (red box and line) at slightly lower voltage bias amplitude (0.5 V). (b) Reconstructed Peltier temperature amplitude (blue box and line) in comparison to the Peltier temperature amplitude measured during bipolar excitation of the nanowire (red box and line) at slightly lower voltage bias amplitude (0.5 V).

and Peltier effects in the two different harmonics. The reconstruction of the Peltier effect from the two unipolar measurements is solely based on the sign change of the Peltier effect upon polarity reversal. Any asymmetry between the two unipolar measurements, e.g., related to polarity-dependent nonlinear electrical effects of the nanowire or the metal/semiconductor contacts in response to the continuous DC offset bias is expected to lead to a deviation between the reconstructed Peltier and Joule temperature fields from those quantified by the bipolar excitation schema. During characterization of self-heating effects of different nanowires we observed nonlinear effect at the metal-semiconductor contacts leading to temperature field signals that cannot immediately be separated into Joule and Peltier effects as illustrated in this chapter. These experimental data sets are currently under evaluation. The comparison of the bipolar and the unipolar detection approach as demonstrated in this section is an interesting cross-check of our measurement and verification that Joule and Peltier effects can be locally separated by the introduced method. While an unipolar voltage excitation is likely required for characterization of more complex nanoelectronic devices, the bipolar excitation is advantageous as it enables the simultaneous characterization of both effects in a single measurement scan.

## 5.6 Conclusions

In the final experimental chapter of this thesis work we demonstrated the local separation of Joule and Peltier effects by scanning probe thermometry. The adaption of a dual harmonic detection scheme to scanning probe thermometry provides a powerful new approach to understand the physical effects behind nanoscopic temperature fields typically observed only as superposition in scanning thermal microscopy measurements.

In particular, we presented the first spatially resolved quantification of Joule and Peltier effects in a nanowire, which is a significant advance as information about the temperature field distribution is typically lost in conventional averaging methods used for the thermoelectric characterization of nanowires [113, 119]. Based on our novel approach, diminishing the topography-related artifacts frequently observed in thermal scanning probe measurements, we studied contact-dominated Joule heating and Peltier effects with a spatial resolution of  $\sim 10$  nm and a sample temperature resolution of  $\sim 0.1$  K.

We expect that the techniques developed in this chapters will significantly enrich the understanding of non-equilibrium electrothermal and thermoelectric processes as they become of increasing relevance for the development of semiconductor nanoelectronics. Our observation of dominating Peltier effects in a voltage bias regime matching the predicted supply voltage range of future low-power electronics [118] highlights the importance to quantify thermal interface effects experimentally. Our studies indicate that the precise understanding of local thermal effects is essential for development of semiconductor nanoelectronics. The experimental investigation of these interface effects might not only address challenges already encountered in CMOS technology but potentially enables new approaches to nanoscale thermal device engineering, e.g., to manipulate the injection or tunneling of charge carriers by thermal interface effects.

Having established the fundamental methodologies of scanning probe thermometry future studies will focus on the characterization of more complex nanoelectronic devices and the possibilities to derive important device and material properties based on the spatially resolved temperature field components. Here, it will become of tremendous importance to combine the measurement of local thermal effects with a spatially resolved characterization of electrical device properties in order to understand the underlying physical mechanisms.



# 6

## Final Remarks

### 6.1 Conclusion

This thesis work reports the development of a pico-Watt-per-Kelvin thermal scanning probe microscope and novel methods for nanoscale thermometry. The performance of the microscope was demonstrated by the investigation of thermal transport across individual graphene layers with sub-10 nm spatial resolution and the quantification of temperature fields with  $\sim 10$  nm spatial and 30 mK temperature resolution.

Apart from the instrumentation, novel methods for nanoscale thermometry were developed. First, a technique termed scanning probe thermometry was introduced, which enables the quantification of nanoscopic temperature fields. Scanning probe thermometry is a two-path method inferring the local temperature of a sample by probing the total steady-state heat flux and a temporally modulated heat flux signal between the scanning probe sensor and a sample simultaneously. Based on this approach, contact geometry-related artifacts, previously limiting the reliability of nanoscopic temperature measurements by scanning thermal microscopy could be minimized. The technique developed is expected to find a wide range of applications for the characterization of temperature fields in various kind of nanosystems. In a second approach, the scanning probe thermometry technique was extended by a dual harmonic detection scheme. This approach enabled the

spatially resolved separation of Joule and Peltier effects on nanoscopic length scales. Previously, only overall temperature fields, potentially the result of various thermal effects, could be studied by scanning thermal microscopy. The approach reported for direct experimental separation of two different thermophysical effects facilitates a deeper understanding of electrothermal and thermoelectric effects in nanoscale devices.

Subsequently, this thesis reported the application of the instrument and methods for characterization of thermal transport and temperature fields in nanosystems.

Thermal transport across graphene layers of different thickness was studied down to 6 nm spatial thermal resolution. The experiments revealed an interface-dominated heat transfer across single-layer graphene (SLG) on both low- and high-conductive substrates. It was demonstrated that a SLG in contact with the hot tip apex impedes heat dissipation despite its potentially high inplane thermal conductivity. With increasing number of graphene layers, a decrease of the thermal resistance was observed and attributed to thickness-dependent spreading of heat. It was concluded that the large thermal anisotropy of graphene sheets relates to an effective thermal thickness much larger than the actual physical thickness, facilitating the potential application of few-layer graphene as atomically thin heat spreader.

The techniques developed were further applied to characterize the self-heating of metal interconnect test structures. The self-heating of nanoscale interconnects is a serious issue in operating integrated circuits. The observation of local hot spots near lithographically defined 40 nm-wide defects demonstrated the capability to investigate the formation of hot spots and related electromigration processes on a length scale that is not accessible by other techniques, such as infrared microscopy.

Another contribution of this thesis is the study of electrothermal and thermoelectric effects in indium arsenide nanowires. Peltier effects and Joule effects at metal semiconductor contacts were directly visualized. These two effects are important for the operation of nanoelectronic devices, such as phase-change memory cells, and can typically only be characterized by spatially averaging methods where the relative temperature field information is lost. The local study of these processes, resolved down to  $\sim 10$  nm opens new opportunities for the characterization of nanoelectronic and energy-conversion devices. The local temperature field information could be used to quantify relevant material and device properties, such as the thermal conductivities, the Seebeck coefficients, and potentially non-thermal properties, like the electrical mobility of charge carriers.

## 6.2 Outlook

In this final section, we aim to provide a vision and an outlook on the numerous possibilities and opportunities that may arise based on the experimental platform and results developed in this thesis.

Most obvious, it is of interest to apply the instrumentation and methods developed to investigate the observed localized Joule and Peltier effects in more detail. In particular, the plateau-like Peltier temperature fields in the vicinity of the contacts appear interesting for further investigations. Also the challenge to separate Joule and Peltier effects in nonlinear electrical devices should be addressed. The investigation of other localized thermal processes, like thermionic effects, and the study of semiconductor junctions are possible based on the instrumentation and methods developed. Because of the direct technological relevance, further studies should preferentially investigate state-of-the-art transistors and memory cells.

The resolution and sensitivity reported in this thesis encourage the investigation of nonequilibrium thermal processes in nanosystems beyond nanoelectronic devices. In particular, the investigation of thermo-optical effects in plasmonic structures, which give rise to very localized temperature fields and gradients, is of interest. Local thermoplasmonic effects are of high relevance for biomedical applications and optoelectronics [121]. In this context it might be of interest or even necessary to extend the measurement platform described by capabilities for non-contact scanning probe operation to explore the thermal near-field radiation in addition to the direct phonon heat conduction dominating in contact mode.

In a broader view, one might envision to extend the thermal scanning probe microscope and thermometry methods to a more general platform for thermal scanning probe metrology for investigation of thermal nonequilibrium processes and properties on nanoscopic length scales. In particular one might further emphasize the possibilities to investigate nanoscopic systems out of equilibrium by exploring the active character of the probe next to its sensing capabilities. In this thesis, the hot tip itself was already applied as variable, movable heat source to investigate thermal transport across graphenes. In contrast to the idea of thermometry measurements, one might apply the probe as local thermal gate to intentionally perturb the temperature field of a device, while measuring its global response, e.g. the electrical conductance as function of the hot tip position.

Furthermore, one might use the unique capability of the probe to simultaneously control not only the temperature but also the pressure locally. In thermodynamics, pressure and temperature are directly related, and both

affect the local equilibrium of a system. During this thesis, we observed the pressure dependence of the tip-sample heat flux only qualitatively during tip-sample approach curves. The effect is rather small, however, might become of more interest if local phase transitions can be either mechanically or thermally initiated by the tip. Here, we are not referring to the local deformation or melting of a polymer, but to the study of solid-state phase transitions in semiconductor and oxide thin films. In particular, one might envision a thermal scanning mode with similarities to piezo-response force microscopy to investigate the nanoscopic properties of pyroelectric/electrocaloric and certain multiferroic systems on nanoscopic length scales.

Another interesting direction could be to explore the capability of scanning probes to pick up nanoscopic or even molecular-sized objects from the surface of a sample. During this thesis, this was not explored intentionally, however, we unintentionally observed significant changes in heat flux if some particle became attached to the tip. If one could combine this with the force sensitivity of the scanning probe cantilever to infer the mass of the particle, one might perform interesting thermogravimetric and calorimetric studies as function of the tip location and temperature.

Finally, one might address the fairly low temporal resolution of the thermal scanning probe microscope as presented in this thesis. This temporal resolution ( $\sim 10 \mu\text{s}$  at best) is sufficient for the characterization of steady-state temperature processes, but too slow for studies of dynamic effects out of equilibrium, as can currently be studied on microscopic length scales by pump-probe thermoreflectance measurements. However, so far no experimental tool exists to study thermal nonequilibrium processes in combination with nanoscopic spatial and high temporal resolution. Accordingly, one might apply heterodyne measurement techniques, as they are known from various scanning probe techniques, to thermal scanning probe systems. The experimental capabilities to study thermal dynamics on nanoscopic length scales might be eye-opening for the understanding of numerous energy transfer and conversion processes in nanosystems. In particular, one might expect to gain new insights into the kinetics of processes on nanoscopic length scales, something that might even be important to understand the most intriguing state of thermodynamic nonequilibrium, living matter.

Within the scope of this thesis outlook, we cannot go into further details in order to illustrate the fascinating opportunities related to progress in thermal scanning probe metrology. What we envision here is, however, as simple as applying thermal scanning probe systems and measurement principles to the study of nonequilibrium processes on nanoscopic length scales in order to understand the conversion of energy at the interaction between heat, light and electricity.

## Bibliography

- [1] J Christofferson, K Maize, Y Ezzahri, J Shabani, X Wang, and A Shakouri. Microscale and nanoscale thermal characterization techniques. *Journal of Electronic Packaging*, 130:041101, 2008.
- [2] DG Cahill, K Goodson, and A Majumdar. Thermometry and thermal transport in micro/nanoscale solid-state devices and structures. *Journal of Heat Transfer*, 124:223, 2002.
- [3] C C Williams and H K Wickramasinghe. Scanning thermal profiler. *Applied Physics Letters*, 49(23):1587–1589, 1986.
- [4] M Nonnenmacher and H K Wickramasinghe. Scanning probe microscopy of thermal conductivity and subsurface properties. *Applied Physics Letters*, 61(2):168–170, 1992.
- [5] A Majumdar, J P Carrejo, and J Lai. Thermal imaging using the atomic force microscope. *Applied Physics Letters*, 62(20):2501–2503, 1993.
- [6] B Cretin, S Gomès, N Trannoy, and P Vairac. Scanning thermal microscopy. *Microscale and Nanoscale Heat Transfer*, pages 181–238, 2007.
- [7] A Majumdar, J Lai, M Chandrachood, O Nakabeppu, Y Wu, and Z Shi. Thermal imaging by atomic force microscopy using thermocouple cantilever probes. *Review of Scientific Instruments*, 66(6):3584–3592, 1995.
- [8] A Hammiche, HM Pollock, M Song, and DJ Hourston. Sub-surface imaging by scanning thermal microscopy. *Measurement Science and Technology*, 7:142, 1996.
- [9] G Mills, H Zhou, A Midha, L Donaldson, and JMR Weaver. Scanning thermal microscopy using batch fabricated thermocouple probes. *Applied Physics Letters*, 72:2900, 1998.

- [10] S Gomès, N Trannoy, and P Gossel. DC thermal microscopy: study of the thermal exchange between a probe and a sample. *Measurement Science and Technology*, 10:805, 1999.
- [11] A Majumdar. Scanning thermal microscopy. *Annual Review of Materials Science*, 1999.
- [12] S Lefevre, S Volz, JB Saulnier, C Fuentes, and N Trannoy. Thermal conductivity calibration for hot wire based dc scanning thermal microscopy. *Review of Scientific Instruments*, 74(4):2418–2423, 2003.
- [13] L Shi. Scanning Thermal and Thermoelectric Microscopy. *Handbook of Microscopy for Nanotechnology*, 2005.
- [14] M Hinz, O Marti, B Gotsmann, M A Lantz, and U Dürig. High resolution vacuum scanning thermal microscopy of HfO<sub>2</sub> and SiO<sub>2</sub>. *Applied Physics Letters*, 92(4):043122, 2008.
- [15] L Shi, J Zhou, P Kim, A Bachtold, A Majumdar, and P L McEuen. Thermal probing of energy dissipation in current-carrying carbon nanotubes. *Journal of Applied Physics*, 105(10):104306, 2009.
- [16] I Jo, I-K Hsu, Y J Lee, M M Sadeghi, S Kim, S Cronin, E Tutuc, S K Banerjee, Z Yao, and L Shi. Low-frequency acoustic phonon temperature distribution in electrically biased graphene. *Nano Letters*, 11(1):85–90, 2010.
- [17] Y Zhang, C L Hapenciuc, E E Castillo, T Borca-Tasciuc, R J Mehta, C Karthik, and G Ramanath. A microprobe technique for simultaneously measuring thermal conductivity and Seebeck coefficient of thin films. *Applied Physics Letters*, 96(6):062107–062107–3, 2010.
- [18] Y-J Yu, M Y Han, S Berciaud, A B Georgescu, T F Heinz, L E Brus, K S Kim, and P Kim. High-resolution spatial mapping of the temperature distribution of a Joule self-heated graphene nanoribbon. *Applied Physics Letters*, 99(18):183105–183105–3, 2011.
- [19] M E Pumarol, M C Rosamond, P Tovee, M C Petty, D A Zeze, V Falko, and O V Kolosov. Direct Nanoscale Imaging of Ballistic and Diffusive Thermal Transport in Graphene Nanostructures. *Nano Letters*, 12(6):2906–2911, 2012.
- [20] T Borca-Tasciuc. Scanning Probe Methods for thermal and thermoelectric property measurements. *Annual Review of Heat Transfer*, 16:211–258, 2013.

- [21] F Ruiz, W D Sun, F H Pollak, and C Venkatraman. Determination of the thermal conductivity of diamond-like nanocomposite films using a scanning thermal microscope. *Applied Physics Letters*, 73(13):1802–1804, 1998.
- [22] D Sarid, B McCarthy, and R Grover. Scanning thermal-conductivity microscope. *Review of Scientific Instruments*, 77(2):023703, 2006.
- [23] E Puyoo, S Grauby, J-M Rampnoux, E Rouvière, and S Dilhaire. Scanning thermal microscopy of individual silicon nanowires. *Journal of Applied Physics*, 109(2):024302, 2011.
- [24] M Reading, DM Price, DB Grandy, RM Smith, L Bozec, M Conroy, A Hammiche, and HM Pollock. Micro-thermal analysis of polymers: current capabilities and future prospects. *Macromolecular Symposia*, 167(1):45–62, 2001.
- [25] A Soudi, R Dawson, and Y Gu. Quantitative heat dissipation characteristics in current-carrying GaN nanowires probed by combining scanning thermal microscopy and spatially resolved Raman spectroscopy. *ACS Nano*, 5(1):255–62, 2010.
- [26] J Chung, K Kim, G Hwang, O Kwon, S Jung, J Lee, J W Lee, and G T Kim. Quantitative temperature measurement of an electrically heated carbon nanotube using the null-point method. *Review of Scientific Instruments*, 81(11):114901, 2010.
- [27] F Menges, H Riel, A Stemmer, and B Gotsmann. Quantitative Thermometry of Nanoscale Hot Spots. *Nano Letters*, 12(2):596–601, 2012.
- [28] K Kim, W Jeong, W Lee, and P Reddy. Ultra-High Vacuum Scanning Thermal Microscopy for Nanometer Resolution Quantitative Thermometry. *ACS Nano*, 81(11):114901, 2012.
- [29] W Jeong, K Kim, K Youngsang, L Woochul, and R Pramond. Characterization of nanoscale temperature fields during electromigration of nanowires. *Scientific Reports*, 4:4975, 2014.
- [30] L Aigouy, G Tessier, M Mortier, and B Charlot. Scanning thermal imaging of microelectronic circuits with a fluorescent nanoprobe. *Applied Physics Letters*, 87(18):184105, 2005.
- [31] W P King, T W Kenny, K E Goodson, G Cross, M Despont, U Dürig, H Rothuizen, G K Binnig, and P Vettiger. Atomic force microscope cantilevers for combined thermomechanical data writing and reading. *Applied Physics Letters*, 78(9):1300–1302, 2001.

- [32] K Edinger, T Gotszalk, and I W Rangelow. Novel high resolution scanning thermal probe. *Journal of Vacuum Science & Technology B*, 19(6):2856–2860, 2001.
- [33] U Drechsler, N Bürer, M Despont, U Dürig, B Gotsmann, F Robin, and P Vettiger. Cantilevers with nano-heaters for thermomechanical storage application. *Microelectronic Engineering*, 67:397–404, 2003.
- [34] Y Zhang, P S Dobson, and J M R Weaver. Batch fabricated dual cantilever resistive probe for scanning thermal microscopy. *Microelectronic Engineering*, 88(8):2435–2438, 2011.
- [35] J Varesi and A Majumdar. Scanning Joule expansion microscopy at nanometer scales. *Applied Physics Letters*, 72(1):37–39, 1998.
- [36] M Igeta, K Banerjee, G Wu, C Hu, and A Majumdar. Thermal characteristics of submicron vias studied by scanning Joule expansion microscopy. *Electron Device Letters, IEEE*, 21(5):224–226, 2000.
- [37] S P Gurrum, W P King, Y K Joshi, and K Ramakrishna. Size Effect on the Thermal Conductivity of Thin Metallic Films Investigated by Scanning Joule Expansion Microscopy. *Journal of Heat Transfer*, 130(8):082403, 2008.
- [38] K L Grosse, M-H Bae, F Lian, E Pop, and W P King. Nanoscale Joule heating, Peltier cooling and current crowding at graphene-metal contacts. *Nature Nanotechnology*, 6(5):287–290, 2011.
- [39] K L Grosse, E Pop, and W P King. Heterogeneous nanometer-scale Joule and Peltier effects in sub-25nm thin phase change memory devices. *Journal of Applied Physics*, 116(12):124508, 2014.
- [40] Y De Wilde, F Formanek, B Carminati, Rand Gralak, P-A Lemoine, K Joulain, J-P Mulet, Y Chen, and J-J Greffet. Thermal radiation scanning tunnelling microscopy. *Nature*, 444(7120):740–743, 2006.
- [41] R Grover, B Mccarthy, D Sarid, and I Guven. Mapping thermal conductivity using bimetallic atomic force microscopy probes. *Applied Physics Letters*, 88(23):233501, 2006.
- [42] S-Jin Kim, T Ono, and M Esashi. Thermal imaging with tapping mode using a bimetal oscillator formed at the end of a cantilever. *Review of Scientific Instruments*, 80(3):033703, 2009.



- [43] B Nelson. Temperature calibration of heated silicon atomic force microscope cantilevers. *Sensors and Actuators A: Physical*, 2007.
- [44] L Shi and A Majumdar. Thermal Transport Mechanisms at Nanoscale Point Contacts. *Journal of Heat Transfer*, 124(2):329–337, 2002.
- [45] B Gotsmann, M A Lantz, A Knoll, and U Dürig. Nanoscale thermal and mechanical interactions studies using heatable probes. *Nanotechnology, Band 6*, Wiley, 2010.
- [46] D G Cahill, W K Ford, K E Goodson, G D Mahan, A Majumdar, H J Maris, R Merlin, and S R Phillpot. Nanoscale thermal transport. *Journal of Applied Physics*, 93(2):793–818, 2003.
- [47] G Chen, D Borca-Tasciuc, and R G Yang. *Nanoscale heat transfer of Nanoscience and Nanotechnology*, volume 7. H.S. Nalwa, Ed., American Scientific Publishers, 2004. 429-459 pp.
- [48] H Böttner, G Chen, and R Venkatasubramanian. Aspects of Thin-Film Superlattice Thermoelectric Materials, Devices, and Applications. *MRS bulletin*, 31(03):211–217, 2006.
- [49] A Minnich and G Chen. Modified effective medium formulation for the thermal conductivity of nanocomposites. *Applied Physics Letters*, 91(7):073105, 2007.
- [50] A J Minnich, J A Johnson, A J Schmidt, K Esfarjani, M S Dresselhaus, K A Nelson, and G Chen. Thermal Conductivity Spectroscopy Technique to Measure Phonon Mean Free Paths. *Physical Review Letters*, 107(9):095901, 2011.
- [51] E Swartz and R Pohl. Thermal boundary resistance. *Reviews of Modern Physics*, 61(3):605–668, 1989.
- [52] R Prasher. Thermal Interface Materials: Historical Perspective, Status, and Future Directions. *Proceedings of the IEEE*, 94(8):1571–1586, 2006.
- [53] B Gotsmann and M A Lantz. Quantized thermal transport across contacts of rough surfaces. *Nature Materials*, 12(1):59–65, 2013.
- [54] G Chen. Particularities of Heat Conduction in Nanostructures. *Journal of Nanoparticle Research*, 2(2):199–204, 2000.

- [55] F Menges, H Riel, A Stemmer, and C Dimitrakopoulos. Thermal Transport into Graphene through Nanoscopic Contacts. *Physical Review Letters*, 111:205901, 2013.
- [56] S Sadat, A Tan, Y J Chua, and P Reddy. Nanoscale Thermometry Using Point Contact Thermocouples. *Nano Letters*, 10(7):2613–2617, 2010.
- [57] D Sarid, P Khulbe, and R Grover. Effects of sample topography and thermal features in scanning thermal conductivity microscopy. *Solid State Communications*, 145(7-8):389–391, 2008.
- [58] J Chung, G Hwang, H Kim, W Yang, Y Ki Choi, and O Kwon. Measurement of thermal contact resistance between CVD-grown graphene and SiO<sub>2</sub> by null point scanning thermal microscopy. *Proceeding of the IEEE International Conference on Nanotechnology (IEEE-NANO)*, pages 1–4, 2012.
- [59] J Chung, K Kim, G Hwang, O Kwon, Y K Choi, and J S Lee. Quantitative temperature profiling through null-point scanning thermal microscopy. *International Journal of Thermal Sciences*, 62:109–113, 2012.
- [60] S M Sze. *Physics of semiconductor devices*, 1981.
- [61] M Yovanovich. *Thermal Spreading and Contact Resistances. Heat Transfer Handbook*, 2003.
- [62] M Hartmann, Günter Mahler, and O Hess. Existence of Temperature on the Nanoscale. *Physical Review Letters*, 93(8):080402, 2004.
- [63] Tamás Sándor Biró. *Is There a Temperature? Conceptual Challenges at High Energy, Acceleration and Complexity*. Springer, 2011.
- [64] H Y Zhang, J Gu, W Barber, and Emerson D R. Modeling thermal flow in the transient regime using a lattice Boltzmann approach. *Europhysics Letters*, 77:300003, 2007.
- [65] E Pop. Energy dissipation and transport in nanoscale devices. *Nano Research*, 3(3):147–169, 2010.
- [66] R C Merkle. *Energy limits to the computational power of the human brain. Foresight Update*, 1989.

- [67] R Landauer. Irreversibility and Heat Generation in the Computing Process. *IBM Journal of Research and Development*, 5(3):183–191, 1961.
- [68] C H Bennett. The thermodynamics of computation—a review. *International Journal of Theoretical Physics*, 21(12):905–940, 1982.
- [69] Carlos D S Brites, P P Lima, N J O Silva, A Millán, V S Amaral, F Palacio, and Luís D Carlos. Thermometry at the nanoscale. *Nanoscale*, 4(16):4799–4829, 2012.
- [70] Jaebeom Lee and Nicholas A Kotov. Thermometer design at the nanoscale. *Scientific Reports*, 2(1):48–51, 2007.
- [71] G Kucsko, P C Maurer, N Y Yao, M Kubo, H J Noh, P K Lo, H Park, and M D Lukin. Nanometre-scale thermometry in a living cell. *Nature*, 500(7460):54–58, 2013.
- [72] E Lörtscher, D Widmer, and B Gotsmann. Next-generation nanotechnology laboratories with simultaneous reduction of all relevant disturbances. *Nanoscale*, 5(21):10542–10549, 2013.
- [73] R Enning, D Ziegler, A Nievergelt, R Friedlos, K Venkataramani, and A Stemmer. A high frequency sensor for optical beam deflection atomic force microscopy. *Review of Scientific Instruments*, 82(4), 2011.
- [74] P Vettiger, M Despont, U Drechsler, U Dürig, W Haberle, M I Lutwyche, H E Rothuizen, R Stutz, R Widmer, and G K Binnig. The Millipede Project: More than thousand tips for future AFM storage. *IBM Journal of Research and Development*, 44(3):323–340, 2000.
- [75] G S Doerk, C Carraro, and R Maboudian. Temperature dependence of Raman spectra for individual silicon nanowires. *Physical Review B*, 80(7), 2009.
- [76] A Sebastian and D Wiesmann. Modeling and experimental identification of silicon microheater dynamics: A systems approach. *Journal of Microelectromechanical Systems*, 17(4):911–920, 2008.
- [77] T Meier, F Menges, P Nirmalraj, H Hölscher, H Riel, and B Gotsmann. Length-Dependent Thermal Transport along Molecular Chains. *Physical Review Letters*, 113(6):060801, 2014.
- [78] S Sadat, E Meyhofer, and P Reddy. Resistance thermometry-based picowatt-resolution heat-flow calorimeter. *Applied Physics Letters*, 102(16):163110, 2013.

- [79] S Ghosh, I Calizo, D Teweldebrhan, E P Pokatilov, D L Nika, A A Balandin, W Bao, F Miao, and C Ning Lau. Extremely high thermal conductivity of graphene: Prospects for thermal management applications in nanoelectronic circuits. *Applied Physics Letters*, 92:151911, 2008.
- [80] Z Gao, Y Zhang, Y Fu, and M Yuen. Graphene heat spreader for thermal management of hot spots. . . . *Conference (ECTC)*, 2013.
- [81] S Subrina, D Kotchetkov, and A A Balandin. Thermal management with graphene lateral heat spreaders: A feasibility study. *Proceedings ITherm, The IEEE Intersociety Conference on Thermal and Thermo-mechanical Phenomena in Electronic Systems*, pages 1–5, 2010.
- [82] Z Yan, G Liu, J M Khan, and A A Balandin. Graphene quilts for thermal management of high-power GaN transistors. *Nature Communications*, 3:827, 2012.
- [83] A A Balandin, S Ghosh, W Bao, I Calizo, D Teweldebrhan, F Miao, and C N Lau. Superior thermal conductivity of single-layer graphene. *Nano Letters*, 8(3):902–907, 2008.
- [84] A Balandin. Thermal properties of graphene and nanostructured carbon materials. *Nature Materials*, 10:569, 2011.
- [85] H-Y Cao, Z-X Guo, H Xiang, and X-G Gong. Layer and size dependence of thermal conductivity in multilayer graphene nanoribbons. *Physics Letters A*, 376(4):525–528, 2012.
- [86] J Chen, G Zhang, and B Li. Substrate coupling suppresses size dependence of thermal conductivity in supported graphene. *Nanoscale*, 5(2):532–536, 2012.
- [87] W Jang, Z Chen, W Bao, C N Lau, and C Dames. Thickness-dependent thermal conductivity of encased graphene and ultrathin graphite. *Nano Letters*, 10(10):3909–3913, 2010.
- [88] M-H Bae, Z Li, Z Aksamija, P N Martin, F Xiong, Z-Y Ong, I Knezevic, and E Pop. Ballistic to diffusive crossover of heat flow in graphene ribbons. *Nature Communications*, 4:1734, 2013.
- [89] A A Balandin. In-plane and cross-plane thermal conductivity of graphene: applications in thermal interface materials. *Proc. of SPIE Vol.*, 8101:07–8, 2011.

- [90] Z Chen, W Jang, W Bao, C N Lau, and C Dames. Thermal contact resistance between graphene and silicon dioxide. *Applied Physics Letters*, 95(16):161910, 2009.
- [91] E Pop, V Varshney, and A K Roy. Thermal properties of graphene: Fundamentals and applications. *MRS bulletin*, 37(12):1273–1281, 2012.
- [92] Y Ni, Y Chalopin, and S Volz. Calculation of inter-plane thermal resistance of few-layer graphene from equilibrium molecular dynamics simulations. *J. Phys. Conf. Ser.*, 395(1):012106, 2012.
- [93] K Sun, M A Stroschio, and M Dutta. Graphite C-axis thermal conductivity. *Superlattices and Microstructures*, 2009.
- [94] M M Sadeghi, M T Pettes, and L Shi. Thermal transport in graphene. *Solid State Communications*, 152(15):1321–1330, 2012.
- [95] S Ghosh, W Bao, D L Nika, S Subrina, E P Pokatilov, C N Lau, and A A Balandin. Dimensional crossover of thermal transport in few-layer graphene. *Nature Materials*, 9(7):555–558, 2010.
- [96] Y K Koh, M-H Bae, D G Cahill, and E Pop. Heat conduction across monolayer and few-layer graphenes. *Nano Letters*, 10(11):4363–4368, 2010.
- [97] J H Seol, I Jo, A L Moore, L Lindsay, Z H Aitken, M T Pettes, X Li, Z Yao, R Huang, and D Broido. Two-dimensional phonon transport in supported graphene. *Science*, 328(5975):213–216, 2010.
- [98] Z Ni, Y Wang, T Yu, and Z Shen. Raman spectroscopy and imaging of graphene. *Nano Research*, 1(4):273–291, 2010.
- [99] O Kazakova, V Panchal, and T Burnett. Epitaxial Graphene and Graphene-Based Devices Studied by Electrical Scanning Probe Microscopy. *Crystals*, 3(1):191–233, 2013.
- [100] Kin Fai Mak, Chun Hung Lui, and Tony F Heinz. Measurement of the thermal conductance of the graphene/ SiO<sub>2</sub> interface. *Applied Physics Letters*, 97(22):221904–221904–3, 2010.
- [101] J R Dryden. The effect of a surface coating on the constriction resistance of a spot on an infinite half-plane. *Journal of Heat Transfer*, 105:408, 1983.

- [102] Y Muzychka and M Yovanovich. Thermal spreading resistance in compound and orthotropic systems. *Journal of thermophysics and heat transfer*, 18(1):45–51, 2004.
- [103] C Dimitrakopoulos, Y-M Lin, A Grill, D B Farmer, M Freitag, Y Sun, S-J Han, Z Chen, K A Jenkins, Y Zhu, Z Liu, T J McArdle, J A Ott, R Wisnieff, and P Avouris. Wafer-scale epitaxial graphene growth on the Si-face of hexagonal SiC (0001) for high frequency transistors. *Journal of Vacuum Science & Technology B: Microelectronics and Nanometer Structures*, 28(5):985–992, 2010.
- [104] S Lloyd. Ultimate physical limits to computation. *Nature*, 406:1047–1054, 2000.
- [105] G I Meijer. Cooling Energy-Hungry Data Centers. *Science*, 328(5976):318–319, 2010.
- [106] G E Moore. Cramming more components onto integrated circuits. *Proceedings of the IEEE*, 1965.
- [107] D Vasilevska, K Raleva, and S M Goodnick. Modeling heating effects in nanoscale devices: the present and the future. *Journal of Computational Electronics*, 7:66–93, 2008.
- [108] S Krishnan, S V Garimella, G M Chrysler, and R V Mahajan. Towards a Thermal Moore’s Law. *Advanced Packaging, IEEE Transactions on*, 30(3):462–474, 2007.
- [109] E Pop, K Banerjee, P Sverdrup, R Dutton, and K Goodson. Localized heating effects and scaling of sub-0.18 micron CMOS devices. *International Electron Devices Meeting*, pages 677–680, 2001.
- [110] A Shakouri, K Maize, P Jackson, X Wang, B Vermeersch, and K Yazawa. Ultrafast submicron thermal characterization of integrated circuits. *IPFA, th IEEE International Symposium on the Physical and Failure Analysis of Integrated Circuits*, pages 1–2, 2011.
- [111] K Banerjee, G Wu, M Igeta, A Amerasekera, A Majumdar, and C Hu. Investigation of self-heating phenomenon in small geometry vias using scanning joule expansion microscopy. *Reliability Physics Symposium Proceedings*, 37:297–302, 1999.
- [112] J P Bourgoin, G G Allogho, and A Haché. Thermal conduction in thin films measured by optical surface thermal lensing. *Journal of Applied Physics*, 108(7):073520, 2010.

- [113] D M Rowe. *Thermoelectrics Handbook: Macro to Nano*. CRC Press/Taylor Francis Group, 2006.
- [114] J Lee, M Asheghi, and K E Goodson. Impact of thermoelectric phenomena on phase-change memory performance metrics and scaling. *Nanotechnology*, 23(20):205201, 2012.
- [115] E Pop, S Sinha, and KE Goodson. Heat generation and transport in nanometer-scale transistors. *Proceedings of the IEEE*, 94(8):1587–1601, 2006.
- [116] B Vermeersch and A Shakouri. Simultaneous thermal imaging of Peltier and Joule effects. *IMAPS Thermal ATW, Palo Alto, CA*, 2010.
- [117] H Ghoneim, P Mensch, H Schmid, C D Bessire, R Rhyner, A Schenk, C Rettner, S Karg, K E Moselund, H Riel, and M T Björk. In situ doping of catalyst-free InAs nanowires. *Nanotechnology*, 23(50):505708, 2012.
- [118] A M Ionescu and H Riel. Tunnel field-effect transistors as energy-efficient electronic switches. *Nature*, 479(7373):329–337, 2011.
- [119] S F Karg, V Troncale, U Drechsler, P Mensch, P Das Kanungo, H Schmid, V Schmidt, L Gignac, H Riel, and B Gotsmann. Full thermoelectric characterization of InAs nanowires using MEMS heater/sensors. *Nanotechnology*, 25(30):305702, 2014.
- [120] V Schmidt, P F J Mensch, S F Karg, B Gotsmann, P Das Kanungo, H Schmid, and H Riel. Using the Seebeck coefficient to determine charge carrier concentration, mobility, and relaxation time in InAs nanowires. *Applied Physics Letters*, 104(1):012113, 2014.
- [121] J B Herzog, M W Knight, and D Natelson. Thermoplasmonics: Quantifying Plasmonic Heating in Single Nanowires. *Nano Letters*, 14(2):499–503, 2014.





## Acknowledgments

At the end of this thesis, I want to thank many friends and colleagues who supported this work and continuously encouraged me throughout this thesis. Without these many people I would not have been able to complete my thesis, and Iâd like to gratefully acknowledge their help and contributions.

I thank Dr. Bernd Gotsmann, my academic mentor. Every thesis is imbedded into an overall research project, and it is due to Bernd's talent, creativity, dedication, and outstanding scientific competence that this project is so successful. I had the privilege and the fortune to work with him for more than four years and he has been guiding me through my studies and research all that time. His ability to recognize my strengths and weaknesses enabled me to develop as scientist and person. I have been impressed again and again by his sharp insights into almost everything I ask him, his patience when explaining and his inspirational comments whenever we were discussing. His way of thinking has significantly influenced me, and I hope we will explore science together for many more years.

I thank Prof. Andreas Stemmer, head of the Nanotechnology group and supervisor of this thesis. Without him, the Nanosystems lecture, and his faith in my abilities, this project would not have been possible. I am grateful for his contributions, his advice on building the microscope, and his continuous support, in particular in the initial phase of this project. He made new experiences possible for me, such as my first lectures at a university class, but he also gave me the freedom to explore new directions on my own. I am deeply grateful to him for all his support. I am looking forward to continue our joint project beyond this PhD thesis.

A special thank goes to Dr. Heike Riel, head of the MIND group at the IBM Research-Zurich laboratory in Ruschlikon. She has supported not only my project, but also my personal development as a scientist. The structures she created were an ideal working environment, and I am thankful for experiencing her continuous support.

I would like to thank Philipp Mensch for fabricating of nanowire devices and

Meinrad Tschudy for his experimental support during the building of the microscope. I also thank Ute Drechsler for fabrication of the scanning probe cantilevers and Blerim Veselaj for building the electrical read-out board of the optical beam deflection detection system. Furthermore, I am grateful to Heinz Schmid and Pratysh Das Kanugo for the growth of nanowires and Christos Dimitrakopolous for providing the graphitized silicon carbide samples. I thank Kevin Lister for the fabrication of the metal interconnect test-structures and Armin Knoll for his advice and the scanning probe holder. I am thankful to Siegfried Karg and Emmanuel Lörtscher for supporting the Raman measurements. I am grateful to Walter Häberle for his advice during building of the microscope and to Marcel Bürge and Urs Egger from the IBM model shop for the fabrication of parts of the microscope. My thanks also go to Martin Witzig, Ralph Heller and Hansruedi Steinauer for support with the measurement electronics, to Lijian Mai and Gabriele Raino for their advice on getting a nice optical image from the cantilever, and to Martin Brunner for taking photographs of the microscope. I also like to thank Tobias Meier for the time we had doing experiments together and the interesting discussions.

I am particularly grateful to Charlotte Bolliger and Peter Nirmalraj for proof-reading my thesis whenever I had some pages complete. This was an outstanding support during the two most intense months of this project.

I am thankful to all members of the MIND group and the IBM Research lab and the Nanotechnology Group at the ETH Zurich for their support and the great time we had also next to the scientific work.

Many more great people, in particular in the Science and Technology department of the IBM Research laboratory, have inspired my work and thinking. I feel lucky that I had the chance to conduct my PhD thesis in such a stimulating environment. It is this mix of people, from many different fields of expertise, which makes it really special to work here, truly creating a melting pot for inventions and ideas. It is in particular due to Dr. Walter Riess, head of the Science and Technology department, that this unique environment can exist in its current form and I like to thank him for his continuous support and the great lab space I could use during my PhD thesis project.

Last but not least, I want to thank Sarah and my family for their love and always being there for me.

## Appendix: Calibration Assumptions and Uncertainty Estimations

In this appendix, we estimate some uncertainties of assumptions used during the electrical fix-point calibration of the cantilever, as reported by Menges et al. [27].

### Assumption of constant thermal resistance of the probe

If we know the electrical power  $P(530\text{ K})$  needed to reach  $T_{heater} = T_{int} = T_{ambient} + 530\text{ K} = 550\text{ }^\circ\text{C}$ , then according to our assumption, we determine the electrical power to reach our operating point of for example  $600\text{ }^\circ\text{C}$  (or  $\Delta T = 580\text{ K}$ ) as

$$P(580\text{ K})/P(530\text{ K}) = 580/530 = 1.09 \quad (.1)$$

To estimate the maximum systematic error of this assumption, we consider a situation depicted in .1. The heater is at a temperature  $T_{ambient} + \Delta T$ .

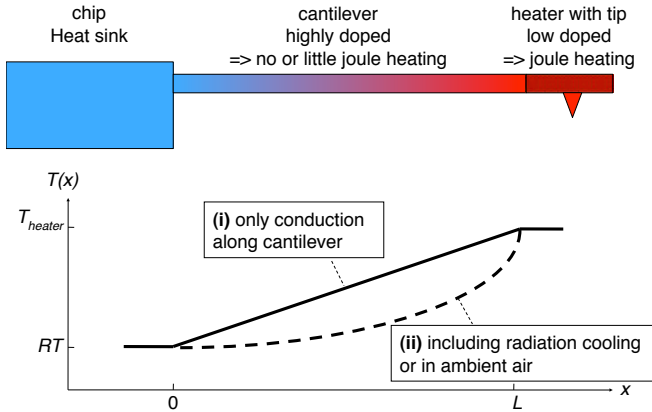


**Figure .1: Schematic of the temperature profile along the cantilever**

Then the temperature profile along the cantilever linking the heater to a

heat sink (the silicon chip) can be expressed as  $T(x) = T_{ambient} + \Delta T x/L$ , where  $x$  is the coordinate along the cantilever and  $L$  is its length (see .1). We consider a temperature-dependent thermal conductivity  $\kappa$  defined as

$$\kappa = c/T, \quad (.2)$$

with  $c$  being a constant accounting for the typical temperature dependence of  $\kappa$  for silicon. The thermal resistance of the cantilever can be defined as:

$$R_{th} = \int_0^L \frac{T(x)}{cWH} dx \quad . \quad (.3)$$

Here,  $W$  and  $H$  denote the height and width of the cantilever, respectively. After integration we find for a cantilever heated up to  $\Delta T$ :

$$R_{th}(\Delta T) = \frac{L}{cWH} \left( T_{RT} + \frac{\Delta T}{2} \right) \quad . \quad (.4)$$

With  $R_{th} = \dot{Q}/\Delta T$  and the assumption  $\dot{Q} = P$  (discussed separately) we have

$$P(\Delta T) = \frac{L}{cWH} \left( T_{RT} + \frac{\Delta T}{2} \right) \Delta T \quad (.5)$$

We therefore can write:

$$P(580\text{ K})/P(530\text{ K}) = \frac{(T_{RT} + 290\text{ K})580}{(T_{RT} + 265\text{ K})530} = 1.14 \quad (.6)$$

The difference to the value calculated with our assumption (see Eq. (.1)) is only 5%.

The same argumentation holds for the assumption concerning the temperature independent thermal resistance of the tip-surface contact. However, there the variation of  $\Delta T$  is larger (e.g. 100°C) and therefore an average of ~15% is plausible. We note, that the argument is independent on the exact geometry of the thermal resistor.

We do not use the seemingly more accurate expression Eq. (.5) because the underlying assumption of a thermal conductivity of the form Eq. (.2) is not accurate for sub-micron thin silicon films (as our cantilevers). Considering a steeper temperature profile along the cantilever due to radiation cooling and the geometric constrains, the expected deviation from our linear assumption is even weaker than in Eq. (.5). This applies even more to the tip-surface contact, which has more constraints in 2D or even 3D. We therefore expect the given uncertainties as conservative.

### Assumption of scaling electrical power to heat flux

We treat the calculation as if all of the electrical power delivered to the heated cantilever is exclusively dissipated into the heater region and none is dissipated in the cantilever beams, so that we can write  $\dot{Q} = P$ . The fraction of the dissipated power in the cantilever beams scales with the fraction of the electrical resistance in the beams divided by the total electrical resistance of the cantilever. The beams are highly doped while the heater region has a low doping level so we expect this fraction to be small. To quantify this small fraction, we use the fact that the cantilevers we use have three electrical contacts (three cantilever beams) attached to two independent heater regions. Through comparing the different electrical resistances between the three contacts we can quantify the electrical resistance of the beams. From this we estimate a fraction of power dissipation of  $\sim 10\%$  only. The systematic error occurring neglecting this contribution is much less, because we use a heated cantilever/heater for the calibration point already.

### Assumption concerning the known temperature at maximum electrical resistance

The temperature-dependent electrical resistivity of doped silicon exhibits a maximum at a temperature  $T_{int}$  determined by the doping level (see .1). At lower temperatures the positive temperature coefficient indicates increased scattering with temperature, while at larger temperatures the increase of charge carriers through thermal activation dominates the temperature dependence. In our case (doping= $5 \times 10^{17}$  at/cm<sup>3</sup>) we calculate a maximum resistance at 550 °C[60]. The limiting factors in this calculation stem from uncertainties in the actual doping levels. Dopants can be trapped, and heat treatments can induce dopant diffusion from the highly-doped cantilever beams into the heater region. The overall uncertainty of dopant concentration is closely correlated to the control in the microfabrication process. For our process we estimate at most 10 % uncertainty in determining  $T_{max}$ .

Combining the different contributions we arrive at a combined uncertainty of determining the thermal resistance of the cantilever of  $<20\%$ , and  $<30\%$  for the determination of the sample temperature.



## Publication List

- **Local imaging of Joule and Peltier Effects in InAs nanowires**  
**F. Menges**, P. Mensch, Schmid, H. Riel, H., A. Stemmer, and B. Gotsmann, in preparation.
  - **A high vacuum scanning thermal microscope for nanoscale thermometry**  
**F. Menges**, H. Riel, A. Stemmer, and B. Gotsmann, in preparation.
  - **Temperature mapping of operating nanoscale devices by scanning probe thermometry**  
**F. Menges**, P. Mensch, H. Schmid, H. Riel, A. Stemmer, and B. Gotsmann, submitted.
6. **Nanoscale thermometry using scanning thermal microscopy**  
**Fabian Menges**, Philipp Mensch, Siegfried Karg, Andreas Stemmer, Heike Riel, and Bernd Gotsmann, Proc. Eurotherm 103: Nanoscale and Microscale Heat transfer IV, 2014.
  5. **Length-dependent thermal transport along Molecular Chains**  
Tobias Meier, **Fabian Menges**, Peter Nirmalraj, Hendrik Hoelscher, Heike Riel, and Bernd Gotsmann, Physical Review Letters 2014 113, 060801.
  4. **Thermal transport into graphene through nanoscopic contacts**  
**Fabian Menges**, Heike Riel, Andreas Stemmer, Christos Dimitrakopoulos, and Bernd Gotsmann, as 'Editor Suggestion' in Physical Review Letters 2013 111, 205901.
  3. **Heat dissipation and thermometry in nanosystems: when interfaces dominate**  
Bernd Gotsmann, **Fabian Menges**, Siegfried Karg, Valentina Troncale, Mark Lantz, Philipp Mensch, Heinz Schmid, Pratyush Das Kanungo, Ute Drechsler, Volker Schmidt, Meinrad Tschudy, Andreas Stemmer, and Heike Riel, Proc. IEEE Device Research Conference, 2013.

2. **Quantitative thermometry of nanoscale hot spots**  
F. Menges, H. Riel, A. Stemmer, and B. Gotsmann, Nano Letters 2012 12 (2), 596-601.
1. **Cellular responses to novel, micropatterned biomaterials**  
M. C. Lensen, V. A. Schulte, J. Salber, M. Diez, F. Menges, and M. Möller, Pure Appl. Chem. 2008 80 (11), 2479-2487

Selected Talks and Presentations:

9. 11/2013 Physics Colloquium University of Konstanz, Germany (invited talk)  
**Probing Thermal Transport and Conversion in Nanosystems**
8. 08/2013 CECAM Workshop-Nanophonics, Bremen (poster)  
**Nanoscale Thermal Imaging by Scanning Probe Microscopy**
7. 06/2013 QMNTIA 2013 - Quantitative Micro and Nano Thermal Imaging and Analysis, Reims (talk)  
**Imaging Thermal Transport and Conversion in Nanosystems**
6. 05/2013 529<sup>th</sup> Wilhelm and Else Heraeus Seminar - Thermal Transport at the Nanoscale, Bonn (talk)  
**Local Probing of Heat Transport and Conversion in Nanosystems**
5. 03/2013 AAFM 2013 - Advanced Atomic Force Microscopy Conference, Karlsruhe (contributed talk),  
**Scanning Probe Thermometry in Nanosystems**
4. 08/2012 ICPS, Zürich (talk),  
**Thermal Hot Spots and Self-Heating of Nanowire Devices**
3. 05/2012 Phonons and Fluctuations Workshop 3, Girona (poster)  
**Quantifying Nanoscale Hot Spots by Scanning Thermal Microscopy**
2. 03/2011 DPG-Frühjahrestagung, Dresden (talk)  
**Thermal Probing of Heat Generation in Biased Silicon Nanowires**
1. 09/2010 Seeing at the Nanoscale VIII, Basel (poster)  
**Scanning Thermal Microscopy of Silicon Nanostructures**